CORROSION BEHAVIOR ON MILD CARBON STEEL C1018 IN CO_2-SATURATED SUPERCRITICAL ENVIRONMENT WITH ADDITION OF H_2S

A Dissertation

by

CHIN-HUA CHENG

Submitted to the Office of Graduate and Professional Studies of
Texas A&M University
in partial fulfillment of the requirements for the degree of

DOCTOR OF ENGINEERING

Chair of Committee,	Raymundo Case
Committee Members,	Homero Castaneda
	Michael J Demkowicz
	Sheng-Jen "Tony" Hsieh
Head of Department,	Ibrahim Karaman

May 2021

Major Subject: Materials Science and Engineering

ABSTRACT

The first part of this dissertation was designed to evaluate three different types of tungsten-based electrodes, which were made in house, and find out the best electrode to measure stable signals in a severe environment (high temperature and high pressure). Electrochemical performance and crystal microstructures of three different types of tungsten-based electrodes were evaluated in pH range of 3 to 10 at room temperature and elevated temperatures. Tungsten/tungsten oxide electrodes were prepared by thermal-oxidized and electrochemical-polarized methods and compared with pure metallic tungsten electrode. The electrochemical properties of the electrochemical-polarized tungsten/tungsten oxide electrode were examined by Cyclic Voltammetry and Mott Schottky testing. Crystal microstructures of the thermal-oxidized and electrochemical-polarized tungsten/tungsten oxide electrodes were confirmed as $W/WO_3/WO_2$ and W/H_2WO_4. The pH measurements of all the prepared tungsten-based electrodes responding to temperature over a wide range of pH values were examined by Open Circuit Potential at room temperature and elevated temperatures.

The second part of this study was aimed to compare the corrosion rate predictions obtained from a state-of-the-art CO_2 corrosion modeling with experimental results on mild carbon steel (C1018) exposed in brine solutions in both sub-critical CO_2 and supercritical CO_2 (SC-CO_2) environments. Corrosion behavior of mild carbon steel were investigated by immersing in a still 1 wt.% NaCl solution at temperatures from 60 – 120^{o}C under both 400 psi (sub-critical CO_2) and under 1600 psi (supercritical CO_2), respectively. The

kinetics of the corrosion process on C1018 were studied by Linear Polarization Resistance (LPR) and Electrochemical Impendence Spectrum (EIS). Surface morphology, element distributions on the surface, and crystal structures of C1018 were evaluated by Scanning Electron Microscopy (SEM), X-ray Diffraction (XRD), and X-ray Photoelectron Microscopy (XPS). The LPR results indicated that the corrosion rates of C1018 in the sub-critical CO_2 environment at steady state were higher than the predicted theoretical values at high temperature, whereas the corrosion rates of C1018 in the supercritical environment at steady state decreased with the increase of temperature and were found consistently lower than its predicted values.

The last part of this study focused mainly on the kinetics and corrosion behavior of C1018 in supercritical CO_2 environment with the presence of H_2S gas. Considering the solubility limit of H_2S gas in water, low concentrations of H_2S gas (5 ppm, 50 ppm, 100 ppm, and 200 ppm) were created via a wet chemical method before temperature and pressure were increased to the same level of our previous research interests (same as in the second part of this study). The kinetics and corrosion behavior were studied by using Weight Loss method (WL), LPR, and EIS technologies. A corrosion mechanism was tentatively proposed to explain the complicated corrosion phenomenon caused by CO_2 corrosion with H_2S corrosion in the supercritical CO_2 environment. Several crucial factors that could largely influence the corrosion rate in the supercritical environment such as temperature, pressure, H_2S concentration, and exposure time, were interpreted and ranked.

DEDICATION

I would like to thank my friends, Weijin, who spent time on listening to me and easing my pressure from the schoolwork and research. I also want to thank my friends, Guoxiu, Rich, Hailin, Tony, and Paul, who brought a lot of joy to me when it was needed. I also would like to thank my previous roommates, Yi-wen, Jui-Hung, and Chia-Pang, who experienced the most difficult period when we just started this “unknown” and “adventurous” journey.

ACKNOWLEDGEMENTS

I would like to thank my committee chair, Dr. Case, and my committee members, Dr. Demkowicz, Dr. Castaneda, and Dr. Hsieh, for their guidance and support throughout the course of this research.

Thanks also go to my colleagues, Lin, Lianlian, and Yuan, and friends, Yenny, Hanna, Minho, Seongkoo, Chungkyu, Brenda, and Reece, and the department faculty and staff, Murat Kaynak, Erin Bandza, and Jules Henry, for making my time at Texas A&M University a great experience.

Finally, thanks to my mother and father for their encouragement and to my husband, Gary, for his patience and love.

CONTRIBUTORS AND FUNDING SOURCES

Contributors

This work was supervised by a dissertation committee consisting of Professor Raymundo Case [advisor], Michael J Demkowicz, and Homero Castaneda, of the Department of Materials Science and Engineering and Professor Sheng-Jen "Tony" Hsieh of the Department of Engineering Technology & Industrial Distribution.

All other work conducted for the thesis (or) dissertation was completed by the student independently.

Funding Sources

Graduate study was supported by a fellowship from Texas A&M University.

This work was also made possible in part by ExxonMobil, Shell, and ConocoPhillips. Its contents are solely the responsibility of the authors.

NOMENCLATURE

AISI	American Iron and Steel Institute
Al	Aluminum
API	American Petroleum Institute
BCC	Body-centered Cubic
CCS	Carbon Dioxide Capture and Storage
CE	Counter Electrode
CPE	Constant Phase Element
CRA	Corrosion-resistive Alloy
CV	Cyclic Voltammetry
CVD	Chemical Vapor Deposition
DI	De-ionized
EDS	Energy Dispersive Spectroscopy
EMF	Electromotive Force
EIS	Electrochemical Impendence Spectrum
EOR	Enhanced-oil Recovery
$FeCO_3$	Iron Carbonate
FeS	Iron Sulfide
H_2CO_3	Carbonic Acid
H_2SO_4	Sulfuric Acid
HB	Hydrogen Blistering

HCl	Hydrogen Chloride
HIC	Hydrogen-induced Cracking
HNO_3	Nitric Acid
HTHP	High Temperature and High Pressure
IP-GID	In-plane Grazing Incidence Diffraction
ISE	Ion-selective Electrode
KOH	Potassium Hydroxide
LPR	Linear Polarization Resistance
MEG	Ethylene Glycol
MS	Mott Schottky
NaCl	Sodium Chloride
NaOH	Sodium Hydroxide
$NaNO_2$	Sodium Nitrite
Ni	Nickel
OCP	Open Circuit Potential
PVC	Poly-vinyl Chloride
RE	Reference Electrode
S	Sulfur
SC	Simple Cubic
SC-CO_2	Supercritical Carbon Dioxide
SCE	Saturated Calomel Electrode
SCL	Space Charge Layer

SEI	Secondary Electron Image
SEM	Scanning Electron Microscopy
SiC	Silicon Carbide
SOHIC	Stress-oriented Hydrogen Induced Cracking
SSC	Sulfide Stress Cracking
XPS	X-ray Photoelectron Microscopy
XRD	X-ray Diffraction
W	Tungsten
WE	Working Electrode
WL	Weight Loss
WO_3	Tungsten Trioxide
YSZ	Yttria-stabilized Zirconia

TABLE OF CONTENTS

Page

LIST OF FIGURES

Page

LIST OF TABLES

Page

1. INTRODUCTION

1.1. Motivations

It is not a secret that demand for energy has increased every year in the world due to economic growth. Traditional energy sources are diminishing, and in the case of the conventional fossil fuel it takes thousands of years to slowly recover after the decomposition of biological species. While research interests are dedicated to exploring and exploiting new energy resources, novel and advanced technologies to improve the production from the original sources are continuously evolving. Development of the alternative techniques has been focused on minimizing environmental damage and impact as global warming and the green-house effect have become more severe over the years. Potential environmental issues, such as reduction of energy consumption, decrease in toxic residues, and better utility of byproducts, are of great concern along with developing new technologies, and most importantly attention is being paid to safer and better quality of the final products. High pressure technology is one of the technologies being developed with growing interest as it can achieve most of the advantages mentioned above through creating a supercritical fluid of interest.

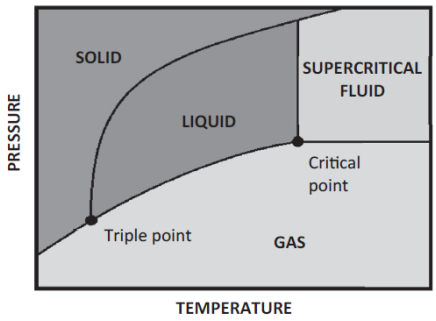

Figure 1: Pressure-temperature phase diagram with existence of solid, liquid, gas, and supercritical fluid. Reprinted from [1].

Supercritical fluid (SCF) is a fluid of a medium (any substance) at a temperature and pressure at or above its critical point [1], shown in Figure 1. When the medium reaches its own supercritical state, no conspicuous boundary can be observed between the gas and liquid phases. Hence, a homogenous phase mixture of gas and liquid phases is created. In the supercritical state, many thermophysical properties such as volumetric properties (P, V, T – behavior), caloric properties (heat capacity, enthalpy, and entropy), and transportation properties (viscosity, thermal conductivity, and diffusivity) [2], are susceptible to small changes in the vicinity of its critical temperature and critical pressure points. It can effuse through porous solids like a gas, overcoming the mass transfer limitations that slow liquid transport through such materials. SCFs are much superior to gases in their ability to dissolve materials like liquids or solids. Table 1 lists the typical values of selected physical properties about gas, liquid, and supercritical fluid, showing the physical properties of a supercritical fluid usually vary between gas and liquid. In other words, supercritical fluid equips with gas-like viscosity and diffusivity as well as liquid-like dissolubility and density. Such dual physicochemical features make it an excellent solvent or being involved in spontaneous chemical reactions in various industrial applications [3]. Moreover, the application of supercritical fluid is developing toward a high pressure technology that provides chances to access the potential possibility of obtaining new products with novel and special features or is used as a key step to design new processes owing to its environmental-friendly, cost-efficient and sustainable advantages [3]. The separation and drying products in the high-pressure technology can be achieved simply by cooling and depressurizing the environment where the gas can be

recycled and reused without further purifying steps. Therefore, supercritical fluid becomes a popular topic that has attracted extensive attention and research interests from scientists and researchers during the past three decades.

Supercritical Carbon Dioxide is used to enhance oil recovery in mature oil fields. At the same time, it is also used as a "clean coal technology" to combine enhanced recovery methods with carbon sequestration. The CO_2 is separated from other flue gases, compressed to the supercritical state, and injected into geological storage, possibly into existing oil fields to improve yields. At present, only schemes isolating fossil CO_2 from natural gas use carbon storage, but there are many plans for future CCS schemes involving pre- or -post-combustion CO_2. Chances to reduce the amount of CO_2 in the atmosphere by using biomass to generate power and sequestering the CO_2 produced is ongoing.

Table 1: Comparison of density, viscosity, and diffusivity between gas, supercritical fluid, and liquid. Reprinted from [4].

Property	Gas	Supercritical Fluid	Liquid
Density (g/cm^3)	10^{-3}	0.3	1
Viscosity (Pa/s)	10^{-5}	10^{-4}	10^{-3}
Diffusivity (cm^2/s)	0.1	10^{-3}	5×10^{-6}

When a medium reaches its own critical point or is in the vicinity of the critical point, many of its properties will change or deviate from its normal behavior [5]. As volumetric, caloric, transportation properties change, it is necessary to understand the thermodynamics of supercritical fluid. Because our research interest focuses on the corrosion behavior in supercritical CO_2 condition, fundamental parts about the thermodynamics are skipped and directly starts with a generalized reduced pressure (P_r) - reduce volume (V_r) diagram as the reduced variables are commonly used to interpret the

correlation between pressure V, volume (or density which equals the reciprocal of volume, $\rho = 1/V$), and absolute temperature T in sub-critical state and supercritical state. Shown in Figure 2, as the pressure increases in the sub-critical region ($T < T_c$), the volume of a gas decreases rapidly with a small change in pressure until it reaches the phase boundary line at Point a_2. As the volume of the gas continues to decrease, formation of liquid drops happens. As long as the total volume of mixed vapor-liquid phases sits in the parabola (two-phase mixture region), gaseous phase and liquid phase co-exist at constant pressure. In other words, points anywhere within the two-phase region depict coexistence of gas and liquid at constant pressure and constant temperature. If all the gas is condensed to Point a_3 on the bubble point line, a further reduction of the total volume will result in a huge increase in pressure since the compressibility of a liquid is low, consequently making it more incompressible compared to that of a gas.

When the temperature increases to the critical point ($T = T_c$, isotherm b), the gas and liquid meet at the climax of the phase boundary line, where an inflection point is observed, so as a horizonal tangent. It indicates the first and second derivatives of pressure with respect to volume at constant temperature are equivalent to zero ($\left(\frac{\partial p}{\partial V}\right)_T = 0$ and $\left(\frac{\partial^2 p}{\partial V^2}\right)_T = 0$). Critical point is considered as the initial region of a supercritical regime. As the temperatures go beyond but are still near the critical points, flat isotherms are gained around reduced volume equaling 1 in the vicinity of the critical point. Consequently, the density is smaller than that of the liquid phase and becomes compressible.

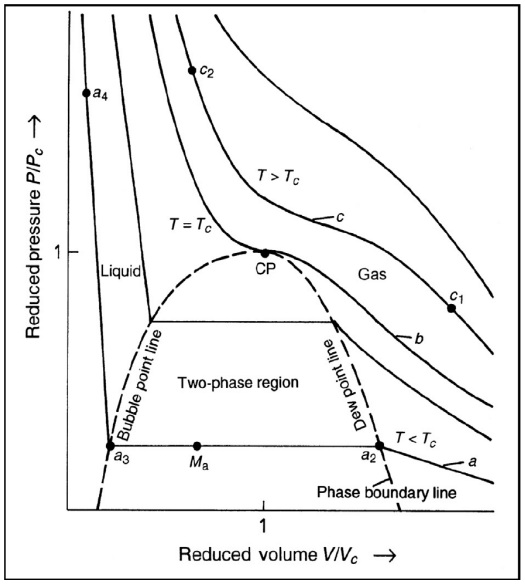

Figure 2: A generalized reduced pressure – reduced volume diagram for P, V, T-behavior in sub-critical and supercritical regions. Reprinted from [6].

Beyond the critical point, the volume of a gas at Point c_3 is decreased to a liquid-like volume at Point c_2 where the compressibility in this region is low, leading the density to increase tremendously. Hence, it is understood that the transition in volume and density varies with the variation of pressure without a certain value for a supercritical fluid, depending on pressure and temperature.

The quantitative interpretation of the P, V, T-behavior for supercritical CO_2 fluid has been developing and becoming more mature and accurate over the years but it is not perfect yet [5, 7, 8]. It can be achieved by using equation of state (EOS) that derives from statistical thermodynamics and accounts for properties of individual substance. Take CO_2 gas for example which is our research interest. The best method to interpret the thermodynamics of supercritical CO_2 fluid is to use cubic EOS with polynomial terms as CO_2 gas is considered as a molecular gas, which saves energies in translational,

vibrational, and rotational forms. Cubic EOS is well-known to explain gas-phase data well when the gas is nonpolar or moderate polar like CO_2, but deviation can be substantial for the density of liquid phase.

Many substances in gaseous state behave like ideal gas at low densities or high pressure. The ideal gas behavior can be explained as a behavior of monoatomic spherical molecules with zero forces also known as "relaxed", and the only interaction taking into account is elastic collision. This model is solid to evaluate the behavior of gas phase at low densities and can be reflected as a reference point to examine the behavior of real gas, which many gases are. Van der Waals [9] in 1873 proposed his famous EOS to describe the ideal-gas behavior based on the assumption of spherical molecules with interactions of repulsive and attractive forces in relative distance between molecules.

$$\boldsymbol{P = \frac{RT}{V-b} - \frac{a}{V^2}} \qquad \textit{(1)}$$

Where P is pressure, T is absolute temperature (K), R is universal gas constant ($J \cdot mol^{-1} \cdot K^{-1}$), a is a constant that represents attractive force, and b is a constant representing repulsive force.

Due to the isotherm at critical point,

$$\boldsymbol{\left(\frac{\partial p}{\partial V}\right)_T = 0} \qquad \textit{(2)}$$

$$\boldsymbol{\left(\frac{\partial^2 p}{\partial V^2}\right)_T = 0} \qquad \textit{(3)}$$

Embedded in Equation (1), then the obtained critical volume (V_c), critical pressure (P_c), and critical temperature (T_c) are showing below:

$$\boldsymbol{V_c = 3b;\ P_c = \frac{a}{27b^2};\ T_c = \frac{8a}{27Rb}} \qquad \textit{(4)}$$

Yet this only explains well for the ideal-gas behavior while supercritical CO_2 fluid should be treated as real gas behavior, which is more complicated. Yokozeki [8] proposed an analytical EOS in terms of reduced parameters, expressed below:

$$\boldsymbol{P_r = \frac{T_r}{V_R - b_R}\left(\frac{V_R - d_R}{V_R - c_R}\right) - \frac{a_R}{V_R^2}} \qquad \textit{(5)}$$

Where $a_R = a_r$, $\mathrm{b_R} = \frac{P_c b}{RT_c}$, $\mathrm{c_R} = \frac{P_c c}{RT_c}$, and $\mathrm{d_R} = \frac{\mathrm{P_c d}}{\mathrm{RT_c}}$, and the four constants vary with temperature. The critical point conditions – Equation (2) and (3), are used to determine the four constants (a, b, c, and d). This simple analytical EOS is proposed based on fundamental thermodynamics and analytical geometry and considered as an extension of the Van der Waals EOS. It can be used to demonstrate thermodynamic properties of pure substance as well as mixtures in soild/liquid/gas regions. In 1994, Span and Wagner [7] published a new EOS with emphasis on Helmholtz free energy correlated with an empirical term to account for the residual part of Helmholtz free energy (see Equation 2.5 in [7]). It was fit with selected data including the volumetric properties (ρ, P, T) and the energy properties (specific isobaric heat capacity C_p) of CO_2 in single phase region and liquid-vapor saturation region. The function holds accurate with uncertainty of $\pm 0.03\%$ to $\pm 0.05\%$ in the density and $\pm 0.15\%$ to $\pm 1.5\%$ in the specific isobaric heat capacity in the region up to pressures of 30 MPa and to temperatures of 523K. The whole series of the EOS development to explain the thermodynamics of supercritical CO_2 fluid is beyond what has been mentioned here. Nonetheless, it is not our research of interest. The reason to introduce these relevant EOS models is to provide some ideas about what would

potentially happen regarding the thermodynamics in a system containing supercritical CO_2 fluid.

Common media used to create supercritical fluid are supercritical carbon dioxide (SC-CO_2) and supercritical water (SC-H_2O), and the former is a better candidate to be used for enhanced-oil recovery (EOR) and carbon dioxide capture and storage (CCS) applications to reduce CO_2 emission in reservoirs, deep water oil, and gas production applications where temperature and pressure are enormously high and play essential roles affecting the production. Supercritical CO_2 possesses lower temperature and pressure critical points (31.1^oC and 7.38 MPa) compared to supercritical water, earning a more suitable position of studying its heat transfer and pressure drop capabilities for heating and cooling processes. Furthermore, with its several advantages like thermal stableness, zero flammability, low toxicity, and abundant existence in nature, SC-CO_2 is broadly used in the oil & gas industry.

1.2. Problem Statement & Objectives

The potential problems of supercritical CO_2 used in CCS are in the pipelines or equipment that are used to transport crude oil and store CO_2 gas in storage sites. It is well-acknowledged that CO_2 gas itself is not corrosive unless a certain amount of water (10 wt.% of H_2O) is involved (> 6.5 wt.% in industrial report). When CO_2 gas contains that amount of water and reaches a supercritical state, the supercritical CO_2 fluid becomes acidic and creates a serious impact on the materials related to the corrosion process. A few

research interests have paid attention to how much damage the corrosion can cause in that severe environment as well as understanding the resulting corrosion mechanism proceeded behind. How to monitor the corrosion behavior effectively and accurately is the key step before accessing the data. This brings up the topic of a suitable reference electrode that can perform well in the supercritical CO_2 environment. Unfortunately, the traditional pH glass electrode is hard to be used in this environment as it is difficult to shape, has a natural fragile feature and long stabilized time, all of which are difficult challenges to apply in the field. Hence, the first part of this study was aimed at developing a reliable tungsten/tungsten oxide reference electrode by using metallic tungsten as the base material. Secondly, with the reference electrode created in house, stable corrosion-related signals of the CO_2 corrosion process in supercritical CO_2 environment (sweet environment) were able to be measured using Electrochemical Impendence Spectroscopy (EIS) in different temperature and pressure ranges and be evaluated with a state-of-the-art corrosion prediction model (by OLI system). The final part of this dissertation focused on studying the corrosion behavior of the supercritical CO_2 containing H_2S gas (sour environment) via Electrochemical Impendence Spectroscopy, Linear Polarization Resistance, and Weight Loss method.

1.3. Reference

1. Cabeza, L.F., et al., *Supercritical CO2 as heat transfer fluid: A review.* Applied Thermal Engineering, 2017. **125**: p. 799-810.
2. Rao, N.T., A.N. Oumer, and U.K. Jamaludin, *State-of-the-art on flow and heat transfer characteristics of supercritical CO2 in various channels.* The Journal of Supercritical Fluids, 2016. **116**: p. 132-147.
3. Knez, Ž., et al., *Industrial applications of supercritical fluids: A review.* Energy, 2014. **77**: p. 235-243.
4. Leitner, W., *Handbook of green chemistry Vol. 4 : Green solvents. Vol. 4 : Green solvents*. 2010.
5. Brunner, G., *Hydrothermal and Supercritical Water Processes*. 2014, Oxford, NETHERLANDS, THE: Elsevier.
6. Brunner, G., *Gas extraction : an introduction to fundamentals of supercritical fluids and the application to separation processes*. 1994, Darmstadt; New York: Steinkopff ; Springer.
7. Span, R. and W. Wagner, *A New Equation of State for Carbon Dioxide Covering the Fluid Region from the Triple-Point Temperature to 1100 K at Pressures up to 800 MPa.* Journal of Physical and Chemical Reference Data, 1996. **25**(6): p. 1509-1596.
8. Yokozeki, A., *Analytical Equation of State for Solid-Liquid-Vapor Phases.* International Journal of Thermophysics, 2003. **24**(3): p. 589-620.
9. Van der Waals, J.D., *Over de Continuiteit van den Gas-en Vloeistoftoestand*. Vol. 1. 1873: Sijthoff.

2. DEVELOPMENT OF TUNGSTEN/TUNGSTEN OXIDE REFERENCE ELECTRODES FOR SUPERCRITICAL ENVIRONMENT

2.1. Research Background of Metal/Metal Oxide Electrode

2.1.1. pH Sensitive Electrodes

Definition

The measurement of pH value plays an essential role in our daily life regarding scientific, biomedical, industrial, environmental purposes, and so on. Before the successful invention of the first pH glass electrode, it was customary to believe that pH value was determined by visualizing the color change of indicators. Although it is the first generation of pH measurement, it still has been continuously used in various industries due to its easiness, convenience, and straightforward use. On the other hand, devices used to measure pH value are called pH sensor or pH sensitive electrode, which is a type of chemical sensors, revealing pH values based on the activity of hydrogen ions (H^+) in a solution [1]. It monitors the mobility of hydrogen ions to interact, but not react, at the interface of two phases. A reliable pH sensor is required to possess features such as high stability, ideal Nernstian linear relationship over a wide range of pH value, and high selectivity [2]. Such advantages are well-proven in a traditional-developed glass electrode, which, even though old, is still the best electrode in a laboratory environment for multiple purposes. Common and commercial pH electrodes used in laboratory environments and fields are:

1. Calomel Reference Electrode
2. Silver-Silver Chloride Reference Electrode

3. Saturated Copper-Copper Sulfate Reference Electrode
4. Traditional glass Reference Electrode

With the same theory applied, a pH sensor used in an electrochemical measurement system is called a reference electrode, which is used to measure potentials of an electrochemical system to determine how reactive the material of interest will be to respond to the system. It can measure the potential of interest and further monitor the thermodynamics and kinetics of the entire system.

A good reference electrode should be the same as a pH sensor, which means it has to have a fast-balancing time, be unreactive or inert to most chemicals, and has harsh-environmental reliance. As a family member in the category of ion-selective electrode (ISE), it is considered as a potentiometric measurement which reflects pH value by detecting the change in potential at the interface of two different materials. Over 50 years of development, it became the standard and major laboratory electrode that measured pH value by sensing the proton concentrations.

History

The development of ion-selective electrodes (ISEs) has a long history [3], which can be traced back to the beginning of the 20th century and divided into three stages. The first stage focused on the gradual development of the traditional pH glass electrode for almost 50 years, starting with the first pH glass electrode invented by Cremer in 1906 and Haber and Klemensiewicz in 1909. The pH glass electrode later became the oldest electroanalytical sensor and is still the best standard tool widely used in laboratory

environments since the 1930s. The theory that was linked with the pH electrode was slowly developed by accumulating high-dispersed data and information based on experience and efforts that dedicated on routinely analytical testing in laboratories. The glass electrodes sensitive to ions were successfully built than the attempts that paid to design sensitive electrodes for hydroxonium ions and electrodes with membranes of materials.

Until the late 1950s, rapid development of various types of electrodes started growing and soon branching toward the directions involved single, double, and even multiple membranes for miscellaneous systems like semiconductor and biochemical sensors in the second stage. Several successful examples were proved by the fabrications of the glass electrodes that were sensitive to alkali metal, silver ions, and ammonium, but unfortunately, they were no longer served. Pungor and his colleagues, around 1960, developed electrodes using silver halide as membranes spreading out on a matrix of silicone rubber, demonstrating that it was sensitive to halide products. In 1966, another successful example was provided that Frant and Ross fabricated an accurate fluoride ion-selective electrode by introducing a lanthanum fluoride single crystal material as a membrane. With multiple successes in the short period of time in 1960s, the first ISE was successfully invented with a liquid membrane.

In the third stage, ionophores, also known as neutral ion carriers, became the key element to help produce diverse ISEs with various membranes. In 1966, Štefanac and Simon produced the first ion-selective electrode of this type selective to potassium ions by coating valinomycin on a membrane. Many other liquid chemical types of electrodes

that were highly selective to ions, such as ion association, ion exchange, and solvent extraction, were also under research investigations. Dedicated in these tremendous efforts, the development of ISEs on neutral ionophores and in these applications were gradually perfected by the technology of plasticized poly-vinyl chloride (PVC) matrix membranes. Finally, with the help of Nikolskii and Eisenman, the theory of ISE was soundly established by standardizing and unifying the experimental procedure and repeated systematical analysis in 1970s.

Principle & Theory

The theory applied on pH sensors and reference electrodes to reflect the activity of hydrogen ions or proton concentration were based on Nernst Equation in Thermodynamics, which was derived from Gibbs free energy of chemical reaction in an electrolytic cell at a given system [3, 4]. When two phases or materials, be them solid or liquid, are in contact with each other, a potential difference will be spontaneously formed and cause a potential flow from high potential to low potential. Such phenomenon can be explained by Thermodynamics to decide the reaction of the entire system.

$$\Delta G^o = -RTlnK \qquad (6)$$

Where K is the equilibrium constant for the reaction of the half-cell, R is the gas constant (8.314J/deg-mole), T is the absolute temperature (degree in Celsius + 273.16), and ΔG^o represents the change of Gibbs free energy between products and reactants at equilibrium.

Nernst Equation derived from Gibbs free energy for a half cell of an electrochemical system at equilibrium is shown below:

$$E = E^o - \frac{RT}{nF} ln \frac{a_Q^q \cdot a_R^r \cdots}{a_L^l \cdot a_M^m \cdots} \quad (7)$$

Where E^o represents the electromotive force (emf) when products and reactants are in standard states, n is the number of the electrons that transfers in the reaction, F is the Faraday constant (96500 C/eq), and a depicts the activity of a given substance that can be obtained by molarity multiple by activity coefficient.

In 2008, Fenster et. al [5] manufactured single tungsten nanowires covered with their own oxides as reliable pH electrodes by selective-etching a directionally solidified eutectic NiAl-W alloy. The pH electrodes were dimensioned with 100-200 nm in diameter, presenting an almost perfect linear relationship along with the increase in pH value from 3.0 to 6.0.

Instead, the properties of the whole system will become uniform than the previous state. However, in order to study the corrosion mechanism in the supercritical environment, an adequate reference electrode is required, so studies of the corrosion mechanism in different metals can be accomplished.

2.1.2. Tungsten Material

Tungsten (W) was officially identified as a new element in 1781 and has attracted extensive research interests due to its exclusive ability of combining with other elements spontaneously [6]. Tungsten can exist alone by itself as a pure and stable chemical structure naturally and is arranged as one of the transition metals in the third series of Periodic Table. As a matter of fact, it owns multiple features of robustness, including the highest melting point – 3422°C (6192°F) and the highest boiling point – 5930°C (10706°F) of all

the elements which have been discovered. In addition, it also possesses high density, the highest tensile strength, the lowest coefficient of thermal expansion compared to other pure metals. While tungsten is intrinsically brittle in polycrystalline state, its pure single-crystalline state possesses more ductility. With the numerous merits about tungsten material mentioned above, researches [7, 8] have been reported with tungsten-related products in the application of gas sensors, electrochromic devices, photolysis, solar cells, and photocatalysis due to its unique electrochemical and photoelectric properties and broad fermi bandgap (2.6 - 3.4 eV) in polycrystalline and amorphous forms of tungsten oxides [9, 10]. In addition, tungsten material also displays complex surface chemistry along with co-existence of W-O system at different temperatures [1].

$$W(gray) \rightarrow W_3O \rightarrow WO_2(brown) \rightarrow WO_x(violet, x = 2.72; blue, x = 2.9) \rightarrow WO_3(yellow)$$

Where x = 2.65-2.75, x=2.88-2.92

Tungsten oxides basically can be classified as three phases: $\alpha-$, $\beta-$, and $\gamma-$ crystalline phases respectively while amorphous phase tungsten also exists naturally [11]. The $\alpha-$ phase is the most stable form among the three phases and has a body-centered cubic (BCC) structure. By comparison, the $\beta-$ phase is a metastable form and has a simple cubic (SC) structure. It can be transformed to $\alpha-$ phase as heated above 600°C. Originally, it was characterized as a suboxide – W_3O, but later it was found out that it could be created as a full oxidized compound – WO_3 using sputtering, thermal evaporation, and chemical vapor deposition (CVD). Lastly, $\gamma-$ phase would exist as an amorphous form at the initial process of sputtering, but it also can be transformed to $\alpha-$ phase when heated no higher

than 700ºC. In electronic states, tungsten oxide forms range from -2 to +6, and the most common oxidation state is +6, which means the correspondent compound is WO_3. WO_3 can dissolve in aqueous alkaline solutions to form tungstate ions - WO_4^{-2}.

2.1.3. Tungsten/Tungsten Oxide Electrodes

The development of tungsten electrodes started in early 1920s with a report where the tungsten wire provided consistent results over pH from 6.5 to 8.6 by reflecting potential difference of approximately 0.09 V per pH [12]. Such primary results for serving as a reliable reference electrode were considerably promising among many other materials compared to the hydrogen-ion determination by using hydrogen electrode. Meanwhile, it was understandable that the sensitivity of measuring pH value was not as fast as expected in the early attempts; reliable reading for pH determination was not stable until a week of measurement processed due to the complexity of the surface chemistry of tungsten material. Nonetheless, the tungsten wire still showed near linear relationship with pH for the pH determination.

In 1971, Levick used a glass micropipette to protect the body of tungsten and created a sharpen tungsten wire tip as a reliable electrode in an electrolytic etching technique [13]. The sharpened tungsten wire tip was prepared by protruding the tip through a borosilicate-glass micropipette in a mixed chemical bath of saturated sodium nitrite ($NaNO_2$), potassium hydroxide (KOH), and DI-water and applying a protected current that would vary no more than 1A. By this method, the extent of the tungsten wire tip was able to be controlled precisely into the micro-level, with 420 μm for the outside stem diameter

of the glass pipette. Although a sharpened tungsten wire could be produced using this method, the demanding and complex multiple steps of such a method would not be able to be an advantage of this technique.

In 1990 [14]and 2003 [15], Przybyt and Sugier found that the best electrode for detecting urea with a reliable responding result (near linear Nernstian slope) is tungsten/tungsten oxide enzyme electrode among other metal/metal oxide enzyme electrodes. The conclusion was rationally reasoned based on the tungsten/tungsten electrode that was produced by oxidizing it in a gas frame and then immersed in deionized water for a day before use, compared to (1) titanium electrodes covered with RuO_2 and tungsten, and (2) titanium-RuO_2 electrode.

In 2003, Yamamoto et. al [2] developed a novel tungsten/tungsten oxide nanoelectrode with a tiny sharp tip as an ultramicrosensor for pH determination by electrochemical etching and oxidation. The tip of the nano tungsten electrode was shaped to 500-800 nm by electrochemical etching in a 0.1 M of sodium hydroxide (NaOH) solution with an applied potential of 0.4 V for approximately 100 seconds. Secondly, a tungsten oxide layer was created by electrooxidation in 2 M of sulfuric acid (H_2SO_4) solution to protect the tip of the produced nano tungsten electrode. The tungsten/tungsten oxide (W/WO_3) ultramicrosensor exhibited an ideal linear Nernstian slope of -53.5 ± 0.5 mV/pH over pH range from 2 to 12. The highly-sensitive tip shortened the response time to 3 seconds at pH of 6 – 7 and up to 15 seconds at high pH. Their experimental results also showed the developed W/WO_3 ultramicrosensor equipped with stability, reproducibility, and longevity with a small change (10%) in EMF after one month of

testing in a 2 M of H_2SO_4 solution. The novel W/WO_3 ultramicrosensor demonstrated better mechanical strength and highly sensitive tip over a wide range of pH compared to the traditional glass electrode.

In 2008, Fenster et. al [5] fabricated single tungsten nanowires as pH sensitive electrodes by selectively etching nickel (Ni) and aluminum (Al) on solidified eutectic NiAl-W alloy. The tiny tip of the tungsten (100-200 nm) was easily exposed and precisely remained on the alloy. This electrochemical etching method was able to control the wire diameter and the spacing between tungsten wires simply by varying the immersing time to produce the miniaturing tungsten nanowires in nano scale with faster balance time and higher sensitivity.

Table 2: Literature Review of Tungsten-based Electrode and its Application

Literatures of Tungsten Material used as in the Application of Reference Electrodes

Forms of Tungsten	Methodology	Electrode type	Field	Ref
Metallic Tungsten wire in a borosilicate-glass micropipette	Electrolytic etching	microelectrodes	Extracellular nerve cells	[13]
Tungsten wire	Electrolytic etching (-61 mV/pH)	Solid-state	intercellular	[13]
Tungsten nanowire	Selective electrochemical etching on directionally solidified eutectic NiAl-W alloy (200 um)	pH-sensitive	Biological cells	[5]
Nano Tungsten/tungsten oxide	Electrochemical oxidation (~ several μm) -53.5 ± 0.5 mV/pH	Solid-state pH ultramicrosensor	Endothelial cells	[2]

2.2. Experimental Approach

In this chapter, two fabrication methods for preparing tungsten/tungsten oxide reference electrodes were served to compare with a pure form of metallic tungsten electrode where no experimental treatments were supplied but only cleaning pretreatment for the specimen surface. In the two fabrication methods, tungsten/tungsten oxide reference electrodes were prepared by thermal oxidation on one side while the other method was electrochemical polarization where cylindrical tungsten coupon was immersed in two different acidic solutions (H_2SO_4 and HNO_3) with various concentrations.

All the metallic tungsten coupons were purchased in a cylindrical shape with a high purity of 99.999% and centerless finished from Metal Samples (Alabama, USA). Before starting with any fabrication methods, all of them were mechanically polished with #800 and #1000 grit of silicon carbide (SiC) sandpapers individually as pretreatment. Acetone and ethanol (99.5% in purity) were served to degrease and clean the surface of the tungsten coupons.

2.2.1. Methodologies of Tungsten/Tungsten Oxide Electrode Preparations

2.2.1.1. Thermal-oxidation Method

In the thermal-oxidized method, a metallic tungsten coupon was burned manually by a torch for 15 ~ 20 minutes in an air condition until a yellowish color of oxidized thin film was created on the surface of the tungsten coupon. It was, later, placed in the same ambient air condition for at least 24 hours to cool down before further treatment took place

in an autoclave vessel at high temperature and high pressure (HTHP) environment. The condition of high temperature and high pressure was served to stabilize the structure of the oxidized tungsten thin film, creating stronger bonding adhering densely with the metallic tungsten surface. Before the high temperature and pressure simulated condition was created, the thermal-oxidized tungsten coupon was immersed in one molar concentration (1M) of sodium chloride (NaCl) solution with sodium acetate as the buffered solution. Hydrogen chloride (HCl) was used to adjust pH value to approximately 4 before the temperature and pressure were increased to our parameters of interest (2.75 MPa and 120^{o}C). The entire process was maintained in that experimental condition for 3 days before use.

2.2.1.2. Electrochemical-polarization Method

The electrochemical-polarization method was processed by cathodically sweeping in acidic solutions in Cyclic Voltammetry (CV) at room temperature. A three-electrode experimental configuration was applied to evaluate the produced tungsten/tungsten oxide reference electrodes. In the electrochemical-polarization method, sulfuric acid (H_2SO_4) and nitric acid (HNO_3) were selected as the electrolyte solutions for electrochemical-synthesizing a thin layer of tungsten oxide covering the surface of the tungsten coupon. Both the acid solutions were maintained on constant concentration during the whole electrochemical oxidization process; one molar (1M) concentration for the sulfur acid concentration, and 1 weight percent concentration (1 wt.%.) for the nitric acid. Both solutions were tested separately. After immersing the metallic tungsten coupons in both acid solutions, a Cyclic Voltammetry (CV) test was cathodically swept from -0.6 V to 1.5

V at a scan rate of 1 mV/s and swept back to the original potential point for 5 cycles in order to adequately create a thin layer of tungsten oxide in a certain level of thickness covering the surface of the metallic tungsten coupons. After the cathodic sweeping was finished, the tungsten/tungsten oxide coupons remained in the same acid solutions for about one day to stabilize the created tungsten oxide structure. During the electrochemical polarization method, a typical standard electrode commonly used in laboratory environments: saturated calomel electrode (SCE) was used as the reference electrode, and graphite was used as the counter electrode in the three-electrode system. Similar preparation was reported elsewhere [16].

The Cyclic Voltammetry (CV) testing result was obtained directly through the electrochemical polarization process in the 1M H_2SO_4 and 1 wt.% HNO_3 solutions. The result demonstrated phase transformation happened on the metallic tungsten surface. The result of the (CV) testing performed on the metallic tungsten coupons showed an oxide layer created on the surface of the metallic tungsten coupons, which proved the thermodynamic calculation of OLI software predicting types of the tungsten oxide formation was correct.

2.2.2. Electrochemical Analyses and Materials Characterizations

In electrochemical tests, Electrochemical Impedance Spectroscopy (EIS), and Mott Schottky (MS) tests were used to study electrochemical properties of the prepared tungsten-based electrodes to evaluate the suitability of using it as a reference electrode for severe environments containing CO_2 gas. Later, Open Circuit Potential (OCP) testing was performed by long-period immersion of the prepared tungsten-based electrodes in the two

acidic solutions over a wide range of pH 3 – 10 with interval of half pH unit as a measurement point at room temperature, and at elevated temperatures (20ºC – 100ºC) with intervals every 10ºC.

Electrochemical Impedance Spectroscopy (EIS) was designed to monitor the in-situ (real time) electrochemical behavior or corrosion monitoring on materials in an electrolyte solution by applying a given potential and observing the frequency feedback output from such materials. Before the EIS testing, one day immersion in the same electrolyte solutions was beneficial to stabilize the structure of the created tungsten oxide layer on the surface. The EIS testing was preceded in the same solutions at an applied DC potential of 0.9V vs. reference potential (E_{ref}) from 10 kHz to 0.001 Hz after one-day immersion in 1M H_2SO_4 and 1 wt.% HNO_3 solutions. The scan rate was set to scan at 0.1 mV/s, and the AC voltage was kept at 10 mV rms.

The invention of Mott Schottky technology was aimed to measure the conductive thickness of a formed phase on top of the original material. Although the relationship between the thickness of the conductive film and of the physical phase could not be verified as a linear slope or an exponential growth, it still could be referred as a certain level or correlation between them. For the Mott Schottky testing, the potential range was selected accordingly based on the result of the CV testing, which meant a broader range of potential had to be chosen for scanning. The chosen range had to go beyond the starting and ending point where the tungsten oxide layer was formed and dissolved. Covering the starting and ending points of the formed oxide layer would be referred as a tool to understand how and when the tungsten oxide structure collapsed.

As for materials characterization analyses, X-ray diffraction (XRD) analysis was undertaken to identify the tungsten oxides formed on the tungsten surface. The analysis was processed with a conventional Cu Kα ($\lambda = 1.542$ Å) target at a scan rate of 1 degree per minute from 10 to 90 degrees. X-ray Photoelectron Spectroscopy (XPS) was employed to observe the change in the valence electron and electronic structures on the oxidized tungsten surface with an Argus detector in the XPS/UPS system.

2.2.3. Configuration, Simulation, and Operation of the Supercritical CO_2 System

2.2.3.1. System Configuration of the Supercritical CO_2 System

The experimental configuration to simulate the supercritical CO_2 environment was composed of an autoclave vessel body and lid, booster pump, temperature control, heating pad, dual thermal and pressure digital monitoring panel, visual standard pressure gauge, venting valves, cooling circulating system, gas-in and gas-out pipelines, and a research grade of carbon dioxide cylinders. The essential pipes and equipment such as the vessel body, lid, gas-in, gas-out, venting valves was made of 316L stainless steel, which is an excellent corrosion-resistant material used widely in Oil & Gas industry to prevent corrosion damage, so the system was sustainable to perform corrosive experiments over a broad range of environmental conditions including various temperatures, high pressure, corrosive liquids, toxic gas, and additives. The whole system was capable of simulating miscellaneous harsh environments at elevated temperatures and pressures. The corrosion-resistive autoclave vessel can contain liquid up to 4 liters, resist working temperature up to 300^{o}C, hold pressure up to 35 MPa as maximum, and function well without fracture.

The booster pump was used as auxiliary equipment to create an ultra-high-pressure environment in the autoclave vessel body by increasing the pressure beyond the limit of a CO_2 gas cylinder. It can deliver a high pressure of 68.95 MPa via extracting liquid CO_2 gas from a CO_2 gas cylinder and pumping it into the vessel body.

The electrochemical testing was conducted by connecting a Gamry potentiostat modelled 600+ with a three-electrode system that was manufactured on a conductive pole with three evenly distributed threads on the tip and was sealed through the autoclave lid, so the solution, electrodes, and cables were able to form a connection with the potentiostat. The 600+ Gamry potentiostat was used to perform Linear Polarization Resistance (LPR) testing and monitor the variation of corrosion potential and polarization resistance in a supercritical CO_2 environment. For the three-electrode system, the prepared W/W_{oxide} specimen was used as the reference electrode, and nickel alloy 725 (UNS N07725) was used as the counter electrode. High-strength carbon steel alloy (API Q125) was chosen to be the working electrode to test and validate the new-installed supercritical system. Later in Section 3.2, the working electrode was switched to the AISI C1018, a family member of mild carbon steel, which is also very commonly used in the Oil & Gas industry for pipelines. It is worth noting that all three electrodes were connected to each other through the supercritical phase of CO_2 in the autoclave vessel without directly contacting the solution to conduct electrochemical testing.

2.2.3.2. Operation of the Supercritical CO_2 System

To start with, 2.5 liters of 1 wt. % sodium chloride solution was added into the autoclave vessel before the autoclave lid was tightened to the autoclave vessel by screwing 12 bolts in diagonally and evenly. Torque sequence was organized as 30, 60, and 120 ft. lbs. step by step. After that, the three-electrode pole was sealed with the autoclave lid of the supercritical system, then followed with the tightening of gas-in and gas-out pipelines. Tested the pressure compactness with N_2 gas for a day and released, the autoclave system was injected with CO_2 from a CO_2 cylinder, and the pressure was brought to 2.758 MPa (400 psi). The next step was to increase the temperature to 65°C and wait until the environment became stable. The booster pump was started to pump in more CO_2 gas and increase the CO_2 partial pressure to 8.27 MPa. When the temperature (65°C) and CO_2 partial pressure (8.27 MPa) were applied in the sealed space, such space became a supercritical CO_2 condition because the critical point of CO_2 gas is at 31.0°C (87.8°F) and 7.3773 MPa (1070 psi). After stabilization, the entire system became more acidic as more CO_2 gas were dissolved into the solution in the confined space. Temperature, pressure, and volume of the solution played important roles concerning the dissolubility of CO_2 gas in the supercritical environment. As more CO_2 gas dissolved into the sodium chloride solution, the pH value of the system decreased to 3.9 as calculated by OLI simulation software.

Linear polarization resistance testing was utilized to measure the corrosion potential, E_{corr} and polarization resistance, R_p of Q125 carbon steel in the supercritical CO_2 environment and validate the installation and set-up of the simulated system. The

LPR testing performed at 8.27 MPa and 65°C lasted for 2.33 hours before the connection between the electrodes collapsed.

2.3. Experimental Results and Discussions

2.3.1. Electrochemical Behavior of the W/Woxide Reference Electrode

Cyclic Voltammetry (CV) Result

Figure 3 shows the Cyclic Voltammetry (CV) result of the W/W_{oxide} reference electrode prepared by the electrochemical polarization method in 0.1 M H_2SO_4 solution for 5 cycles at room temperature. The CV testing was aimed to create an oxidized layer on top of the metallic tungsten surface by sweeping from positive potential to low potential at a scan rate of 1 mV/s and backward. In Figure 3(a), the CV result showed that the current started increasing gradually when the potential swept from -0.25 V to 0.75 V, indicating an anodic reaction occurred on the surface of the metallic tungsten coupon. This scan rate was appropriate for hydroxide ion to migrate onto the metallic tungsten surface and combine to form hydrous tungsten oxide ($WO_3 \cdot H_2O$) or tungstite (H_2WO_4).

Note that a tentative trial to create a W/W_{oxide} reference electrode by using a HNO_3 solution as electrolyte in the electrochemical polarization method was also tested. Its CV result was remarkably similar to the one prepared in the H_2SO_4 solution. Thus, in this study, we only focused on discussing the W/WO_3 reference electrode prepared in the H_2SO_4 solution.

To analyze the CV result more precisely, a logarithm function was reasonably applied on current as plotted in Figure 3(b). It is clearly observed in the logarithm form that the current was decreased gradually (from -0.6 V to 0 V) and had a stiff drop (from 0

V to 0.105 V), addressing that the tungsten surface was activated, and an oxidation layer was formed during the sweeping. The tungsten ion was oxidized and combined with hydroxide ion, which migrated from the H_2SO_4 solution. As the potential passed around 0.105 V, the fluctuation of the current slowed down and became stable. At that stage, a passivation layer was formed and covered the metallic tungsten surface, which, later at around 0.3V to 0.75V, seemed to decompose because the current increased tremendously by 2 orders in the logarithm form. It is wort noting that the current didn't act the same as the potential scanned from negative potential to positive potential (-0.6 V to 1.5 V). As the potential scanned back to negative, the current was still stable. It could be explained since the passivation layer didn't decompose completely in that range.

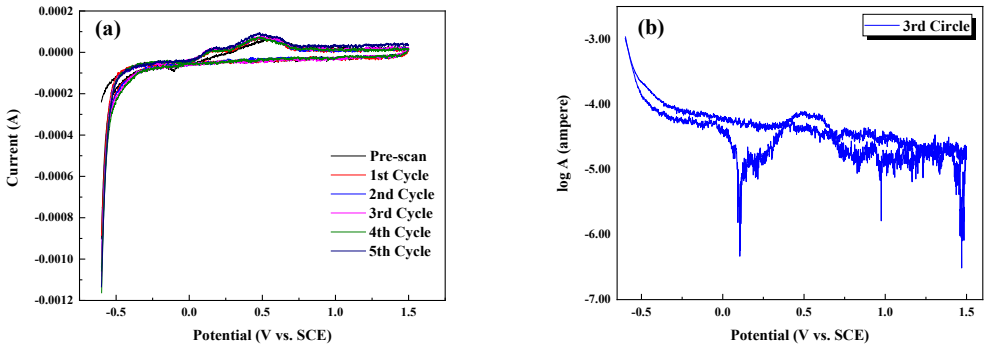

Figure 3: (a) CV result of the tungsten/tungsten oxide reference electrode proceeded in 0.1M H_2SO_4 electrolyte for 5 cycles from -0.6V to 1.5V at room temperature; (b) the fourth circle of CV result plotted with potential vs. logarithm current.

Mott Schottky Testing (MS)-Electrochemical Polarization method

Figure 4 shows the thickness of the space charge layer (SCL) in the formed oxide layer on the surface was tested using the Mott Schottky (MS) measurement. Experimental parameters such as potential and frequency used in the MS testing were selected

accordingly based on other electrochemical testing results. The potential scanning range (-0.3 V to 1.1 V vs. $E_{reference}$) chosen for the MS testing was based on the CV result of the W/W_{oxide} reference electrode, and 1000 Hz was selected to perform the MS testing together. Regardless of the EIS result, choosing such a high frequency would be beneficial to maximize the capacitive response of the tungsten oxidized layer as an optimum value in the MS testing.

As shown in Figure 4, the capacitance of the oxidized layer was increased as the potential decreased from 1.1 V to 0 V gradually. When the potential reached 0 V, the thickness of the SCL in the passive layer became zero, and the capacitance was equivalent to infinite, demonstrating that the $W/WO_3{\cdot}H_2O$ reference electrode acted as a n-type semiconductor behavior in a p-n junction material. In this case we would further calculate the charge carrier density by using Equation (11) and Equation (12).

$$\boldsymbol{C = \varepsilon \frac{A}{L}} \tag{8}$$

$$\boldsymbol{C_{SCL}^{-2} = \frac{2}{e{\cdot}\varepsilon{\cdot}N_D}\left(E - E_{FB} - \frac{kT}{e}\right)} \tag{9}$$

Where ε was dielectric constant, A was the contact area, L symbolized the thickness of the space charge layer (SCL), C_{SCL}^{-2} represented the capacitance of the SCL, N_D was the charge carrier density, and E_{FB} was the flat band potential.

$N_D = -4.7264 \times 10^{19} \cdots\cdots\cdots\cdots\cdots\cdots$ the charge carrier density of the 1st MS testing

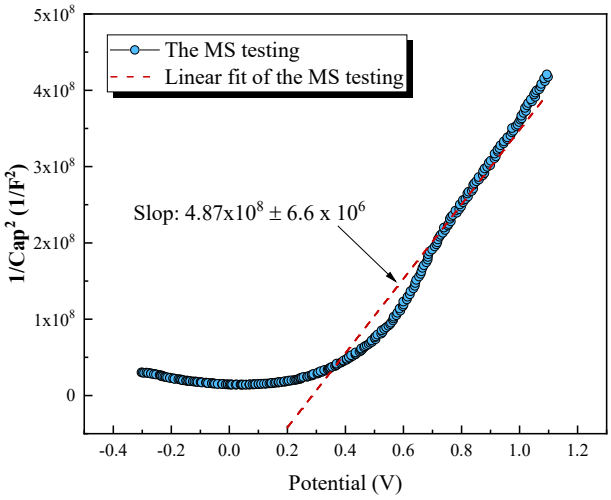

Figure 4: Mott Schottky plot of the W/$WO_3 \cdot H_2O$ reference electrodes prepared by the electrochemical polarization method.

2.3.2. Materials Characterizations of the W/Woxide Reference Electrodes

X-ray Diffraction Analysis (XRD)-Thermal Oxidation Method

As thermally oxidized, the tungsten surface was covered by a thick oxidized layer, which was composed of two or possibly more oxidized products, depending on temperature, oxidation time, the degree of oxidation, and the gas atmosphere used for oxidizing. The determination of the whole oxidized tungsten products could be deceptive by observing the light yellowish color on the top of the surface merely, which was not the only phase created by this method. Part of the superficial yellowish oxidized layer was fluffy and easily removed simply by touching, shaking, or tapping, whereas the inner part is bonded a little more tightly with the surface, but still in yellowish color. What was hidden beneath the yellowish layer was another oxidized product in navy or dark blue color, which was considered as an incomplete oxidized product. The incomplete oxidized product resulted from the influence of accessibility to react with limited oxygen and from

the nature of the complex surface chemistry of the tungsten material itself. In this way, the tungsten oxide products were twofold: one was completely oxidized product in the most stable form of tungsten oxide, and the other one was inclined to form as a non-stoichiometric product: WO_2 [17].

Figure 5 shows the X-ray diffraction spectrum of the tungsten/tungsten (W/W_{oxide}) reference electrode produced by the thermal oxidation method. In the XRD spectrum, the dark grey line represented the result of the W/W_{oxide} reference electrode created by the thermal oxidation method while the red line stands for the pure metallic tungsten coupon after cleaning as pre-treatment to remove any potential grease, dirt, and pollution.

The peaks populated at 40.22°, 58.25°, 73.1°, and 86.99° (JCPDS Card 01-089-2767) on the red line belonged to the original metallic tungsten coupon, showing the crystal plane of (110), (200), (211), and (220) of the natural pure form of W, which later completely disappeared as it was thermally oxidized and observed on the grey dark line. It clearly showed that an oxidized tungsten layer was created and thick enough to cover the entire surface of the metallic tungsten coupon, preventing the electron beam from penetrating through the surface layer of the tungsten oxide, so no peaks belonging to the pure metallic tungsten coupon were detected. After confirmation with JCPDS card 43-1035 and 05-1431, the whole oxidized tungsten products were composed of two forms of tungsten oxides, in the crystal form of WO_3 and WO_2, demonstrated by the peaks shown at 23.08°, 23.56°, 24.31° on the dark grey line.

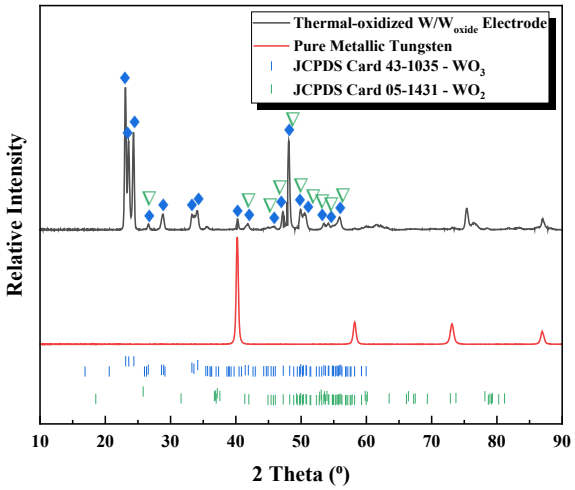

Figure 5: X-ray diffraction spectrums of the W/W$_{oxide}$ reference electrode prepared by the thermal oxidation method.

X-ray Diffraction Analysis (XRD)-Electrochemical Polarization Method

Figure 6 shows that the crystal structure of the tungsten/tungsten oxide reference electrode was examined by X-ray Diffraction Analysis (XRD) before and after performing the MS testing, where the blue line directly depicted the as-prepared tungsten/tungsten oxide reference electrode by the electrochemical polarized method while the red line represented the tungsten/tungsten oxide reference electrode already evaluated by the MS testing.

On the blue line, the existence of the peaks located at 21.49°, 30,61°, and 40.00° was examined with JCPDS card 43-0679, confirming that the oxidized layer on top of the metallic tungsten surface was tungstite in a hydration form of $WO_3 \cdot H_2O$ (also known as H_2WO_4), whereas the peaks at higher angles such as 45.28°, 63.25°, and 78.19° belonged to the original metallic tungsten itself. Although both the lines showed similar results in terms of existence of the hydrous tungsten oxide ($WO_3 \cdot H_2O$) or tungstite (H_2WO_4), the

peak intensity of the hydrous tungsten oxide was reduced, explained by the effect that the cathodic sweep nature of the MS testing dissociated the dense tungsten oxide structure. Meanwhile, an unexpected effect from the MS testing was also observed by a relatively flat but broad bulging peak from 20° to 30°. This could be explained by an increased hydration effect that was intensified by the MS testing, which was beneficial to the formation of amorphous sate or the hydrated state of tungsten oxide. Note that the potential sweeping range was within the potential boundary used in the Cyclic Voltammetry (CV) testing.

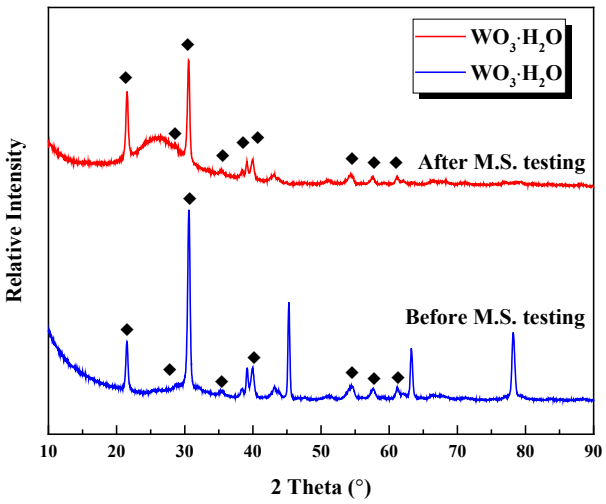

Figure 6: X-ray diffraction spectrums of the electrochemical-prepared tungsten/tungsten oxide reference electrode before and after Mott Schottky test.

X-ray Photoelectron Spectroscopy (XPS)-Electrochemical Polarization Method

Figure 7 shows the chemical surface composition of the electrochemical-polarized $W/WO_3 \cdot H_2O$ reference electrode investigated by X-ray Photoelectron Spectroscopy (XPS). The XPS technology was processed before and after the Mott Schottky testing in

1M H_2SO_4 solution at room temperature. Initially, the survey result of the brief whole XPS spectrum, shown in Figure 7 (a), depicted that the electronic orbital of $W_{4p1/2}$, W_{4d}, and W_{4f} was evidenced by the peak locations at 427 eV, 247 eV, and 35 eV while the evidence of O 1s was shown at the peak location of 530 eV [18]. The strong peak of O_{1s} on the surface of the $W/WO_3 \cdot H_2O$ reference electrode was explained as associations related to metal oxide and hydroxide species of tungsten after the electrochemical polarized method swept from -0.6 V to 1.5 V at room temperatures for 5 times.

In Figure 7 (b), before and After the Mott Schottky testing, the crystal structure of the tungsten oxide reference electrode retained the same chemical compositions on the surface, demonstrated by the presence of the electronic orbitals of W 4f. To be exact, it is proved by the peaks populated at 35.55 eV and 37.75 eV corresponding to $W_{4f7/2}$ and $W_{4f5/2}$, respectively. It is worth noting that the peak intensity of the W 4f electronic orbital decreased after the MS testing was performed. Reasonable explanation was delivered with the deprivation or degradation of the structure caused by the main function of the MS testing - the cathodic sweep from positive potential to negative potential, which could be considered as destructive testing. It also indirectly resulted in thinning the thickness of the tungsten oxide layer on the surface. In the aspect of change in peak location, the $W_{4f7/2}$ electronic orbital of the $W/WO_3 \cdot H_2O$ reference electrode at 35.55 eV only shifted toward higher binding energy by 0.25 eV after the Mott Schottky testing.

The results in Figure 7 (b) proves that tungsten oxide crystal structure in an hydration state was successfully created by the electrochemical polarization method and still adequately maintained after the MS testing. Furthermore, the explanation of the $W_{4f7/2}$

peak was correlated to the tungsten oxidation form of WO_3, which was in agreement with the XRD result (shown in Figure 6).

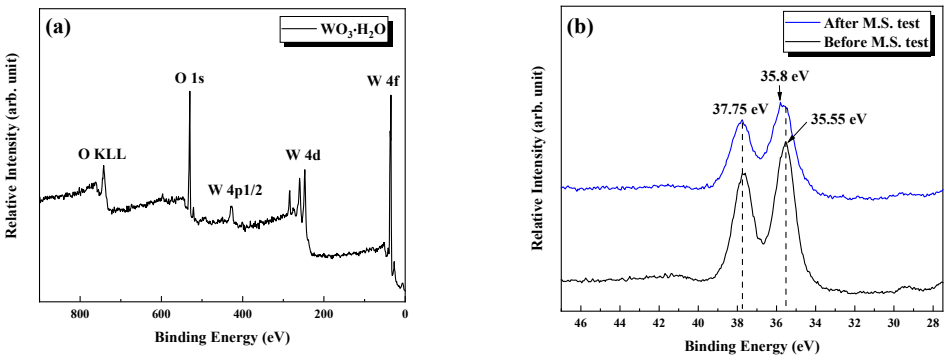

Figure 7: (a) XPS survey spectrum of the W/WO_3·H_2O reference electrode (b) XPS spectrum of the W/WO_3·H_2O reference electrode at low binding energy range.

2.3.3. Discussion of W/Woxide Reference Electrode

Kriksunov *et al* [19] reported that the tungsten/tungsten oxide reference electrode prepared by the thermal oxidization method had a reliable pH response from pH 2 to pH 11 at high temperature, compared with the yttria-stabilized zirconia (YSZ) membrane electrode. In their study, the tungsten/tungsten oxide reference electrode still showed excellent pH responding behavior in different concentrations and various electrolytes including 0.01M to 10M NaOH, 0.005M to 0.25M H_2SO_4, and 0.01M to 0.1M $NiSO_4$ and a buffer solution of 0.1M H_3BO_3 mixed with 0.01M NaOH at high temperatures such as 250°C and 300°C. The experimental result was consistent with the calculation result from the modified Nernst Equation, shown as Equation (13). However, it remained unclear and unexplained which electrochemical reaction was responsible for the W/W_{oxide} reference electrode since two of the electrochemical reactions presented similar electrochemical

potentials, only by 200 mV difference. No evidence was shown to prove the prepared W/W_{oxide} reference electrode was in favor of the electrochemical potential range in the thermodynamic system of tungsten.

$$\boldsymbol{E = E^{o}_{W/W_4O_{12}} - \frac{2.303RT}{F} pH - \frac{2.303RT}{2F} log(a_{H_2O})} \quad \textbf{(10)}$$

Where $E^{o}_{W/W_4O_{12}}$ is the standard potential of W/W_4O_{12}, and a_{H_2O} is the activity of water.

The testing solution used in the experiments - 1M NaCl electrolyte solution contains 10 wt. % ethylene glycol (MEG), showing that it would start to boil at 130°C, so the temperatures chosen to simulate high temperature environment were 50°C, 60°C, 70°C, 80°C, 90°C and ended at 100°C. This result was obtained using OLI simulation software and used as a key factor since temperature plays an important role in thermodynamics. Temperature, pressure, pH values, activity coefficients of H_2O, and molarities of H_2O were input as experimental parameters in a thermodynamic equilibrium speciation program of the OLI software and used to compute the theoretical potential values at different temperatures. From the calculation, the output theoretical potential was -261.47 V, -283.69 V, -306.23 V, -329.07 V, -352.18 V, -375.55 V, -399.17 V, -423.03 V, -446.12 V, and -454.34 V, versus SCE from 20 - 110°C, shown in Table 3.

Table 3: pH of the aqueous solution containing with 10 wt. % of MEG, molarity of water, and activity coefficient of water were computed in the OLI simulation software.

Temperature (°C)	The pH of the Aqueous Solution containing MEG	The Molarity of Water (mole)	The Activity Coefficient of Water	Electrochemical Potential (V vs. SCE)
20	7.08	52.61	0.983	-261.47
30	6.92	52.45	0.982	-283.69
40	6.77	52.24	0.982	-306.23
50	6.63	52.00	0.982	-329.07
60	6.51	51.72	0.982	-352.18
70	6.40	51.42	0.982	-375.55
80	6.30	51.07	0.982	-399.17
90	6.21	50.66	0.982	-423.03
100	6.13	47.90	0.965	-446.12
110	6.07	23.55	0.691	-454.34

2.3.4. Comparison and Evaluation of the Tungsten/Tungsten Oxide Reference Electrodes

Figure 8 shows the pH response of the tungsten-based electrodes prepared by the thermal-oxidized (dark grey), electrochemical polarization (red), and pure metallic tungsten (blue) electrode from 3 – 10 at room temperature in Open Circuit Potential (OCP) measurement. In the OCP measurement, all the tungsten-based electrodes presented decrease in the open circuit potential as the measured solution became more alkaline (high pH) from acidic solution (low pH). Among all of them, the pH response of the electrochemical-polarized tungstite electrode was detected with 45.0 ± 4.1 mV per pH, showing the closest pH response to the theoretical values (55 mV per pH) in the comparison of the thermal-oxidized tungsten oxide electrode (38.8 ± 2.9 mV per pH) and the metallic tungsten electrode (27.1 ± 2.8 mV per pH). Nonetheless, the thermal-oxidized tungsten oxide electrode was still considered as the most satisfactory one in all of them

due to its most linear Nernstian relationship (0.93) relating to pH at room temperature. The relative narrative potential response over a broad pH range resulted from the solid thermal-oxidized tungsten oxide structure adhering tightly to the tungsten surface; that was difficult for chemical dissolution to take place in the acidic solution.

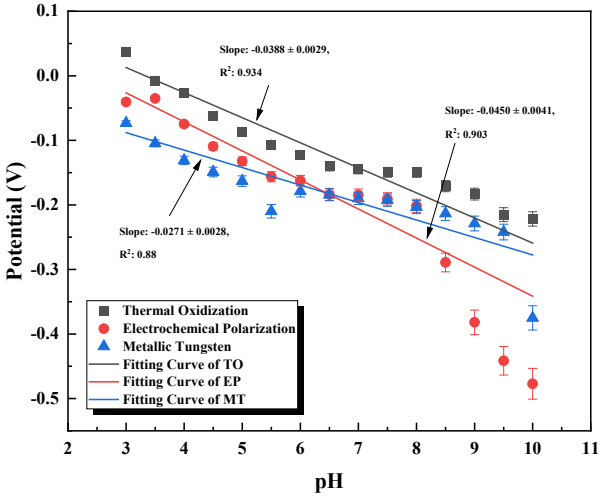

Figure 8: pH response measured by the thermal-oxidized (dark grey), electrochemical-prepared tungsten-based (red), and pure metallic tungsten (blue) electrode from pH 3 – 10 at room temperature.

Figure 9 shows the potential comparison of the theoretical values with the real potential values measured by the W/W_{oxide} reference electrodes prepared by the thermal oxidation and electrochemical polarization methods. The potential was plotted as Y axis versus temperature, depicting that the theoretical potential values increased linearly as the temperature rose from room temperature to 100°C. As the temperature went beyond 100°C, the electrochemical potential decreased slower than it did at lower temperatures because it was influenced by the boiling of water which influenced the concentration of the ethylene glycol in the aqueous solution.

In the aspect of potential measurement, the W/W_{oxide} electrode prepared by the thermal oxidation method was more reliable from 50ºC to 100ºC, whereas the reference electrode fabricated by the electrochemical polarization method seemed to deviate more as the temperature increased. Initially, the measured potential of the electrochemical-polarized tungsten oxide reference electrode decreased from -216.4 V to -297.6 V as the temperature rose from 20°C to 30°C. However, its potential response acted randomly after 30°C, meaning that no clear correlation with elevated temperature was observed. From the material analysis results above, a more plausible reason that could explain this phenomenon was that the hydrous tungsten oxide ($W/WO_3 \cdot H_2O$) or the loosened tungstite structure (H_2WO_4) oxide layer was easier to be dissolved to the solution from the surface as the temperature went up.

On the other hand, the thermal-oxidized tungsten oxide reference electrode presented a better and more linear response to the temperature in the comparison of the electrochemical-polarized one. The measured potential dropped from -187.2 V to -282.6 V as the temperature decreased from 50°C to 100°C. The potential deviation responding with the pH range seemed much smaller, which is consistent with the theory. Note that the standard electrochemical potentials of the W/W_4O_{12} at 1 bar was gathered from the NIST Standard Reference Database 103a.

$$\boldsymbol{4W + 12H_2O \leftrightarrow W_4O_{12} + 24H^+ + 24e^-} \qquad \textbf{(11)}$$

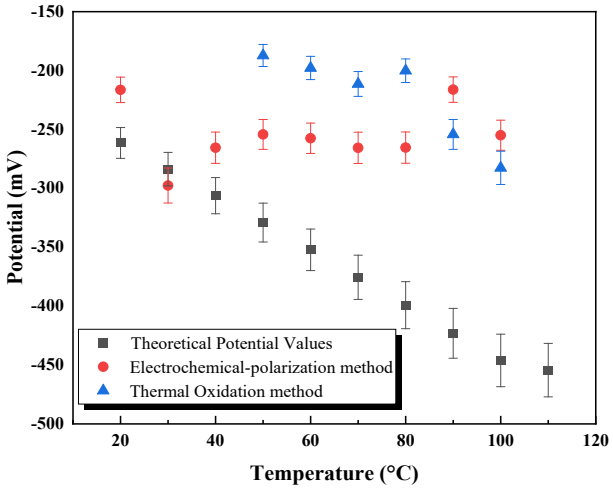

Figure 9: Comparison of the temperature response of the theoretical values with real potentials measured by the thermal-oxidized and electrochemical-polarized W/Woxide reference electrodes from room temperature to 110°C in an aqueous solution with 10 wt. % of MEG.

Based on the results in Figure 8 and Figure 9, the thermal oxidized W/WO_3 reference electrode was chosen as the reference electrode for the following supercritical testing at 65°C in 8.27 MPa. Although the electrochemical-polarized W/W_{oxide} reference electrode demonstrated sub-Nernst relationship in response of pH at room temperature, the created hydrous tungsten oxide layer was not stable as temperature started to rise. In other words, as temperature increased, the hydrous tungsten oxide structure decomposed and lost its capacitance ability, which made it less suitable to perform and monitor corrosion testing in supercritical environment.

2.3.5. Corrosion Testing in Supercritical CO_2 Conditions

Figure 10 shows the variation of polarization resistance (R_p) and corrosion potential (E_c) in response to time on Q125 carbon steel monitored by the LPR testing at

65ºC in 8.27 MPa. Carbon dioxide became a supercritical state when part of the CO_2 gas condensed in liquid form, and part of the aqueous solution evaporated and mixed with the CO_2 gas. Theoretically, no clear boundary can be observed between the gas and liquid phases. The supercritical CO_2 environment is non-corrosive itself until an adequate amount of water (>10 wt. %) is introduced in such an environment. Some literature reported that the supercritical CO_2 environment would become corrosive even only if 6.5 wt. % of water were present in that environment. Hence, to be clear, a water-saturated supercritical CO_2 environment at 65ºC in 8.27 MPa was used to simulate the supercritical environment as an initial trial.

What was worth noting was that the W/WO_3 electrode was circulated by a mixed phase of gas and liquid CO_2. Since the autoclave vessel achieved a supercritical condition, part but not all the aqueous solution evaporated and mixed with the gas phase in the autoclave. Hence, it was assumed that the three electrodes were connected to each other by the continuity of the mixed phase of gas and liquid CO_2.

The LPR testing was performed under the supercritical condition simulated at 65°C in 8.27 MPa in an autoclave vessel for about 2.3 hours. As observed in Figure 10, the result showed that the polarization resistance,R_p, remained high around 90 – 100 k ohm during the entire testing time. Initially, the fluctuation of the polarization resistance was tremendous during the first 2000 seconds, and then it became mild when the time passed 8000 seconds in comparison with the initial values, indicating that the corrosion reaction became more active.

The corrosion potential of the thermal-oxidized W/WO_3 electrode, E_{corr}, in the supercritical condition was obtained with the help of Equation (13), where the pH 3.9 was computed by inputting the amount of CO_2 gas in the supercritical phase at equilibrium with water. Also, the fugacity of water was considered to calculate the reference potential of the W/WO_3 electrode for the water-saturated supercritical CO_2 environment (8.27 MPa). Therefore, through calculation, the open circuit potential of the Q-125 carbon steel decreased to -0.702 V from -0.52 V. The E_{corr} values shown in Figure 10 are converted to the Ag/AgCl reference electrode scale in order to compare them with other supercritical CO_2 studies on X65 carbon steel [20].

Tang [20] reported that the measured open circuit potential on X65 carbon steel in water-saturated supercritical CO_2 environment (8 MPa and 50°C) without O_2 was not available until the continuous water film was formed after 10-hour testing processed and obtained -0.68 V (vs saturated Ag/AgCl). Their result compared favorably with the OCP obtained in our supercritical CO_2 testing, where at steady state an OCP of -0.710 V was observed when the W/WO_3 reference electrode was brought to the same standard scale as the Ag/AgCl reference electrode. Furthermore, the comparison of the polarization resistance (R_p) values with their experimental results were also found to be consistent, indicating that both experiments showed a similar corrosion rate. Therefore, it was concluded that among the three reference electrodes, the thermal oxidation method was a better technique and reinforced a decision to fabricate tungsten oxide reference electrode for the corrosion measurement in a supercritical environment. The thermal-oxidized W/WO_3 reference electrode was a viable alternative to other reference electrodes in the

water-saturated supercritical CO_2 environment for corrosion testing. It provided reliable potential reading upon pH from 50°C to 100°C and was suitable for corrosion study electrochemical in supercritical CO_2 environments.

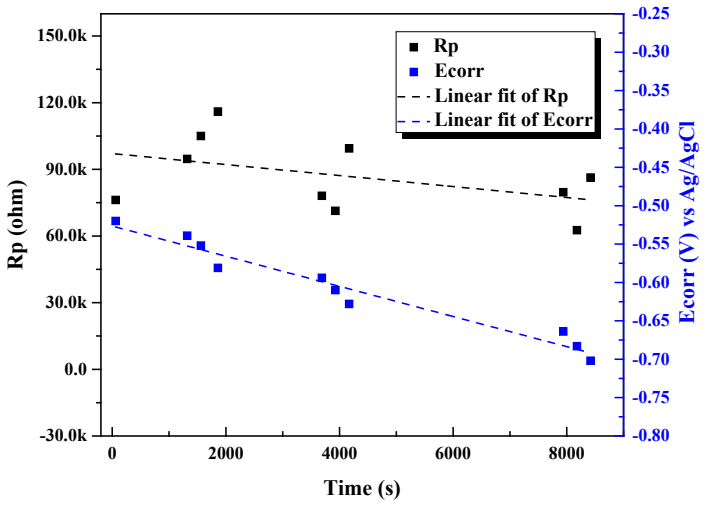

Figure 10: LPR testing of Q125 carbon steel in response of time in supercritical environment.

2.4. Conclusions

- The tungsten/tungsten oxide reference electrodes were successfully prepared by the thermal oxidation and electrochemical-polarization methods and tested at room temperature over pH 3 – 10 and at elevated temperatures from 20°C to 100°C.

- The metallic tungsten and thermal-oxidized W/W_{oxide} reference electrodes present better Nernst relationship in response to pH than the electrochemical-polarized one at room temperature. Furthermore, the thermal-oxidized W/W_{oxide} reference electrode demonstrated the best sensing performance compared to all the prepared tungsten electrodes.

- The linear polarization resistance measurement and the open circuit potential testing demonstrated that the thermal-oxidized W/WO_3 electrode can be used as a reference electrode to study the supercritical environment containing CO_2 phase.

2.5. References

1. Wen, Y. and X. Wang, *Characterization and application of a metallic tungsten electrode for potentiometric pH measurements.* Journal of Electroanalytical Chemistry, 2014. **714**(Supplement C): p. 45-50.
2. Yamamoto, K., et al., *Solid-state pH ultramicrosensor based on a tungstic oxide film fabricated on a tungsten nanoelectrode and its application to the study of endothelial cells.* Analytica Chimica Acta, 2003. **480**(1): p. 109-117.
3. Štulík, K., *ION-SELECTIVE ELECTRODES | Overview*, in *Encyclopedia of Analytical Science (Second Edition)*, P. Worsfold, A. Townshend, and C. Poole, Editors. 2005, Elsevier: Oxford. p. 493-498.
4. Revie, R.W., *Corrosion and Corrosion Control : An Introduction to Corrosion Science and Engineering*. Vol. 4th ed. 2008, Hoboken, N.J.: Wiley-Interscience.
5. Fenster, C., et al., *Single tungsten nanowires as pH sensitive electrodes.* Electrochemistry Communications, 2008. **10**(8): p. 1125-1128.
6. Lassner, E. and W.-D. Schubert. *Tungsten: Properties, Chemistry, Technology of the Element, Alloys, and Chemical Compounds*. 1999.
7. Tsuchiya, H., et al., *Self-organized porous WO3 formed in NaF electrolytes.* Electrochemistry Communications, 2005. **7**(3): p. 295-298.
8. Hahn, R., J.M. Macak, and P. Schmuki, *Rapid anodic growth of TiO2 and WO3 nanotubes in fluoride free electrolytes.* Electrochemistry Communications, 2007. **9**(5): p. 947-952.
9. Chawla, A.K., et al., *Influence of nitrogen doping on the sputter-deposited WO3 films.* Thin Solid Films, 2009. **518**(5): p. 1430-1433.
10. Hendi, A.H.Y., et al., *Modulation of the band gap of tungsten oxide thin films through mixing with cadmium telluride towards photovoltaic applications.* Materials Research Bulletin, 2017. **87**: p. 148-154.
11. Schubert, E.L.a.W.-D., *Tungsten Properties, Chemistry, Technology of the Element.* Alloys, 1999.
12. Baylis, J.R., *Tungsten Wire for Hydrogen-Ion Determinations.* Industrial & Engineering Chemistry, 1923. **15**(8): p. 852-853.
13. Levick, W.R., *Another tungsten microelectrode.* Medical and biological engineering, 1972. **10**(4): p. 510-515.
14. Przybyt, M. and H. Sugier, *Metal-metal oxide enzyme electrodes for the determination of urea.* Analytica Chimica Acta, 1990. **237**: p. 399-404.
15. Przybyt, M. *Potentiometric tungsten electrodes with enzymes immobilised by the sol-gel technique*. 2003.
16. Wen, Y., et al., *Tungsten oxide electrode for measurement of ultralow liquid flow velocity.* Sensors and Actuators B: Chemical, 2015. **215**: p. 459-463.
17. Pašti, I.A., T. Lazarević-Pašti, and S.V. Mentus, *Switching between voltammetry and potentiometry in order to determine H+ or OH− ion concentration over the entire pH scale by means of tungsten disk electrode.* Journal of Electroanalytical Chemistry, 2012. **665**: p. 83-89.

18. Casella, I.G. and M. Contursi, *Electrochemical and spectroscopic characterization of a tungsten electrode as a sensitive amperometric sensor of small inorganic ions.* Electrochimica Acta, 2005. **50**(20): p. 4146-4154.
19. Kriksunov, L.B., D.D. Macdonald, and P.J. Millett, *Tungsten/Tungsten Oxide pH Sensing Electrode for High Temperature Aqueous Environments.* Journal of The Electrochemical Society, 2019. **141**(11): p. 3002-3005.
20. Tang, Y., X.P. Guo, and G.A. Zhang, *Corrosion behaviour of X65 carbon steel in supercritical-CO2 containing H2O and O2 in carbon capture and storage (CCS) technology.* Corrosion Science, 2017. **118**(Supplement C): p. 118-128.

3. EXPERIMENTAL EVALUATION OF CORROSION MODELING ON CARBON STEEL IN SUB-CRITICAL AND SUPERCRITICAL CO_2 ENVIRONMENTS

3.1. Research Background of CO_2 Corrosion

3.1.1. CO_2 Corrosion

CO_2 corrosion is one of the major corrosion mechanisms requiring tremendous attention in the Oil and Gas industry [1]. It is important to clarify that CO_2 gas itself is not corrosive until water is involved with the existence of CO_2 gas. The water molecule combined with CO_2 gas leads to the formation of carbonic acid (H_2CO_3), which lowers the pH of a solution and makes the material of interest susceptible to corrosion. Such corrosion happens equally often and maybe more compared to other corrosion mechanisms happening to pipelines, equipment, and facilities.

$$\boldsymbol{CO_2 + H_2O \rightleftarrows H_2CO_3} \tag{12}$$

The formation of carbonic acid from carbon dioxide reacting with water can always easily be written as shown above, but actually it is not that simple; the whole chemical reaction of the corrosion process is controlled by three cathodic reactions and one anodic reaction. The cathodic reactions include bicarbonate ions and hydrogen produced by the reduction of carbonic acid as the first step (Equation (4)), continuous reduction from bicarbonate ions into carbonate ions (the second step shown as Equation 5), and the final step: the reduction of hydrogen ions.

$$\boldsymbol{2H_2CO_3 + 2e^- \rightarrow H_2 + 2HCO_3^-} \tag{13}$$

$$\boldsymbol{2HCO_3^- + 2e^- \rightarrow H_2 + 2CO_3^{2-}} \tag{14}$$

$$2H^+ + 2e^- \rightarrow H_2 \quad (15)$$

The anodic reaction significantly involved with iron materials in CO_2 corrosion is the oxidation of iron into the ferrous (Fe^{2+}) ion shown in Equation 7.

$$Fe \rightarrow Fe^{2+} + 2e^- \quad (16)$$

These corrosion reactions are fundamentally important to understand the basics of a CO_2 corrosion mechanism. Overall, the sum of the reactions provides a direction toward the formation of iron carbonate ($FeCO_3$) in anaerobic conditions. To be exact, when ferrous ions or materials are present in a system full of CO_2 gas (no air or oxygen-contained), the ferrous ions react with bicarbonate ions to form iron carbonate and can be finished in one step or in two paths. First of all, ferrous ions can simply form iron carbonate by combining with carbonate ions, or it can be accomplished through two paths where the formation of ferrous iron bicarbonate from the combination of ferrous ions with bicarbonate ions, and subsequently the ferrous iron bicarbonate dissociates into iron carbonate as a corrosion product along with carbon dioxide and water.

one step: $$Fe^{2+} + CO_3^{2-} \rightarrow FeCO_3 \quad (17)$$

two steps: $$Fe^{2+} + 2HCO_3^- \rightarrow Fe(HCO_3)_2 \quad (18)$$

$$Fe(HCO_3)_2 \rightarrow FeCO_3 + CO_2 + H_2O \quad (19)$$

What needs to be addressed is that the precipitation of $FeCO_3$ corrosion product swiftly happens as it is withdrawn from a solution owing to its limited solubility. The precipitate has the chance to form passive films on the surfaces of ferrous materials, which in this study are mild steels, and protect the materials from being corroded or reducing the corrosion reaction.

3.1.2. Pourbaix Diagram of Iron-Irion Oxide (water) System

The Pourbaix diagram, named after Marcel Pourbaix, was constructed to predict and understand the thermodynamic properties of material(s) of interest at a certain temperature, pressure, and ion concentration in a given environment with the help of potential and pH [24]. Generally speaking, a Pourbaix diagram provides information such as passivity, immunity, and corrosion in a given experimental condition in a specific medium for materials (metals). Based on the potential applied and the hydrogen ion concentration of the solution, the prediction or tendency of the material of interest to be corroded, oxidized, or maintain immunity became possible.

Ferrous Materials

Ferrous materials are undoubtedly the most popular engineering material in industry by far. Its abundant existence and easiness-to-weld feature make it appealing for industrial usage, covering architectural, agricultural, semiconductor, biotechnological, medical, and energy fields. The abundant existence of iron is used as a criterion to identify whether or not the material is a ferrous or a nonferrous material. Among various ferrous materials, typically they can be divided into two categories: iron-based or ferrous alloy materials, depending on types and amounts of different materials added into the material of interest. By varying the addition of carbon element, steel typically is defined with 0.05 to 2.0 wt.% of carbon element addition while cast irons generally contain 2.0 to 4.5 wt.% of carbon amount in their chemical compositions.

Within the category of steel, a total amount of 5 wt.% of noncarbon elements serves as a boundary line to distinguish low-alloy steels from high-alloy steels. While

small quantities of elements other than carbon and iron can change material characteristics dramatically, one thing that should be aware of is the cost of the chosen elements added. With that being said, the addition of other elements should be chosen to avoid tremendous material cost. Based on the types of elements and their concentrations, materials can be tailored for specific purposes and be improved in terms of higher strength, better corrosion resistance, ease to be shaped, and more. Chromium, for instance, can improve corrosion resistance of such material. The content of chromium for industrial use is usually found with 10 wt. % addition. At least 4 wt. % of chromium addition is considered as a minimum in order to increase the resistance from being corroded. If the material simply consists iron and carbon without other elements, then it is carbon steel, which is the most commonly used in industry. You can automate the figure/table caption numbering by clicking on the figure/table and then under the References tab, select Insert Caption. You can toggle the Label choices to either figure or table. If you don't want chapter numbers included in your numbering system, click on Numbering and then unclick the box that says "Include chapter number."

3.1.3. Carbon Steel (C1018)

Carbon steels, also named plain-carbon steels, are one of the major ferrous materials, mainly containing carbon and iron as its major element distribution. Due to its cheap cost and availability, carbon steels are widely used in industry. However, the problem of the carbon steels was identified by one of its drawbacks – lack of the ability to resist corrosion. For example, the addition of carbon in iron can increase the intensity, hardness, and strength of the material. The mechanical properties of steel with low content

of carbon is pretty much the same as iron: soft and easy to weld. The increase in the carbon content will affect the hardness and strength, lowing the ductility to be manufactured, and high content of carbon generally would reduce the temperature resistance and lower the melting point of steel.

Table 4: Major Element Contents of Types of Carbon Steels

Chemical Composition of Carbon Steel (C1018) by weight

	Carbon, C	Microstructure	Function(s)	Examples
Mild (low carbon) steel	0.02 – 0.25 %	Ferrite, pearlite	Less strong but cheap and easy to shape, surface hardness can be increased through carburizing	AISI 1018 steel
Medium carbon steel	0.14 – 0.84 %	Martensite	Balances ductility and strength, good wear resistance, used for large parts, forging and car parts	AISI 1040 steel
High carbon steel	0.59 – 0.65 %	Pearlite	Strong, used for springs and high-strength wires	AISI 1065 steel
Ultra-high carbon steel	0.96 – 2.1 %	-	Produce specific atomic and molecular microstructures	-

3.2. Experimental Approach

3.2.1. Experimental Preparation, Equipment, and Operation

Materials Sources

Due to economic efficiency and widespread acceptability in the Oil & Gas industry, mild-low carbon steel (C1018) was selected and purchased from Metal Samples (Alabama, USA) to study the corrosion behavior in both the sub-critical CO_2 and supercritical CO_2 environments in this chapter. It is a popular commercial material that shows a good balance of toughness, strength, and ductility. In addition, it has excellent weldability and can produce a solid and uniform product easily. The chemical composition of mild-low carbon steel consists C ($0.14 - 0.2\%$ in weight), Fe ($98.81 - 99.26\%$), Mn

$(0.6 - 0.9\%)$, P ($\leq 0.04\%$), S ($\leq 0.05\%$), as shown in Table 5. The mild-low carbon steel was a cylindrical coupon dimensioned using 1.72" x 0.25" and finished with a centerless ground.

Table 5: Chemical composition of mild-low carbon steel (C1018)

Mild-low Carbon steel (AISI C1018)					
Element	Carbon, C	Iron, Fe	Manganese, Mn	Phosphorous, P	Sulfur, S
Amount (%)	0.14 – 0.2	98.98 – 99.26	0.6 – 0.9	≤ 0.04	≤ 0.05

Testing Equipment

To process the study in the supercritical condition successfully, an autoclave system was employed for all tests. The autoclave system was composed of an autoclave itself, a three-electrode system for conducting electrochemical testing, a lid with twelve bolts to seal with the autoclave, a rupture valve for safety concerns, and two pipelines for gas-in and gas-out on the top. A booster pump was used to bring the pressure to supercritical level. A heating pad was wrapped around the autoclave body. A thermometer, pressure monitor, and draining outlet were installed at the bottom side of the autoclave.

Experimental Procedure

Each test included two carbon steel specimens; one was examined with Linear Polarization Resistance (LPR) to calculate the corrosion rate in both sub-critical and supercritical CO_2 environments, and the other specimen was performed with Electrochemical Impedance Spectroscopy (EIS) on it to study the kinetics of corrosion behavior. Prior to the test, all specimens were polished mechanically with 400, 600, and 800 grit silicon carbide (SiC) sandpapers respectively, and then were degreased and

cleaned with acetone, ethanol and deionized water (DI water) step by step. After the pretreatment was finished, one of the cylindrical mild-low carbon steels was mounted on a probe of the three-electrode system as a working electrode (WE) for the electrochemical testing. Hastelloy C-2000 alloy, a corrosion-resistant material from the nickel-chromium-molybdenum alloy family with addition of copper shown in Table 6, was used as the counter electrode (CE) and mounted on the second probe. Mounted on the third probe of the three-electrode system, a tungsten/tungsten oxide was prepared by the thermal oxidation method, which was previously established in the first part of this study and was employed as the reference electrode (RE). The positions of the three electrodes were fixed with a certain distance in between. Another specimen was attached to an individual pole solely to perform LPR testing. The autoclave was filled with 2.8 L of fluid, and sodium chloride (NaCl) was 1% of the solution by weight for conducting the electrochemical testing. Note that due to the experimental design, the actual area of the working electrode immersed in the solution was 1/3 of its calculated surface area, so as the counter electrode and reference electrode.

Table 6: Chemical composition of Hastelloy C-2000 alloy (UNS N06200)

Hastelloy C-2000 alloy (UNS N06200)													
Element	C	Mn	Si	P	S	Cr	Co	Mo	V	Fe	Al	Cu	Ni
Amount (%)	0 – 0.01	0 – 0.5	0 – 0.08	0 – 0.02	0 – 0.01	22 - 24	0 – 2	15 - 17	0 – 0.5	0 – 3.0	0 – 0.5	1.3 - 1.9	Bal

Electrochemical testing was conducted simultaneously in the autoclave vessel. After the sodium chloride solution was pulled in the autoclave, the lid was sealed securely on the top of the autoclave. To remove air bubbles from the solution, a research grade

nitrogen (N_2) cylinder with 99.9999% purity was used to de-aerate the autoclave for 1 hour in the process of increasing the temperature to 60ºC. A research grade of carbon dioxide (CO_2) cylinder with 99.9995% purity was followed to clear the nitrogen out for 10 minutes before the pressurizing process started. After the temperature was increased to the value of interest, which was set to 60, 80, 100, and 120ºC respectively, the high-purity CO_2 gas was injected to increase the pressure in the autoclave vessel. The pressure was targeted at 2.75 MPa (400 psi) for the sub-critical environment and 11.03 MPa (1600 psi) for the supercritical environment. The pressuring process reached 2.75 MPa for the sub-critical environment in seconds while it took minutes to achieve the supercritical level: 11.03 MPa. All the tests in this chapter were processed for 72 hours, and the specimens were taken out one day later after the autoclave vessel was cooled down for analyses of X-ray Diffraction (XRD), Scanning Electron Spectroscopy & Energy Dispersive Spectroscopy (SEM & EDS), and X-ray photoelectron Spectroscopy (XPS).

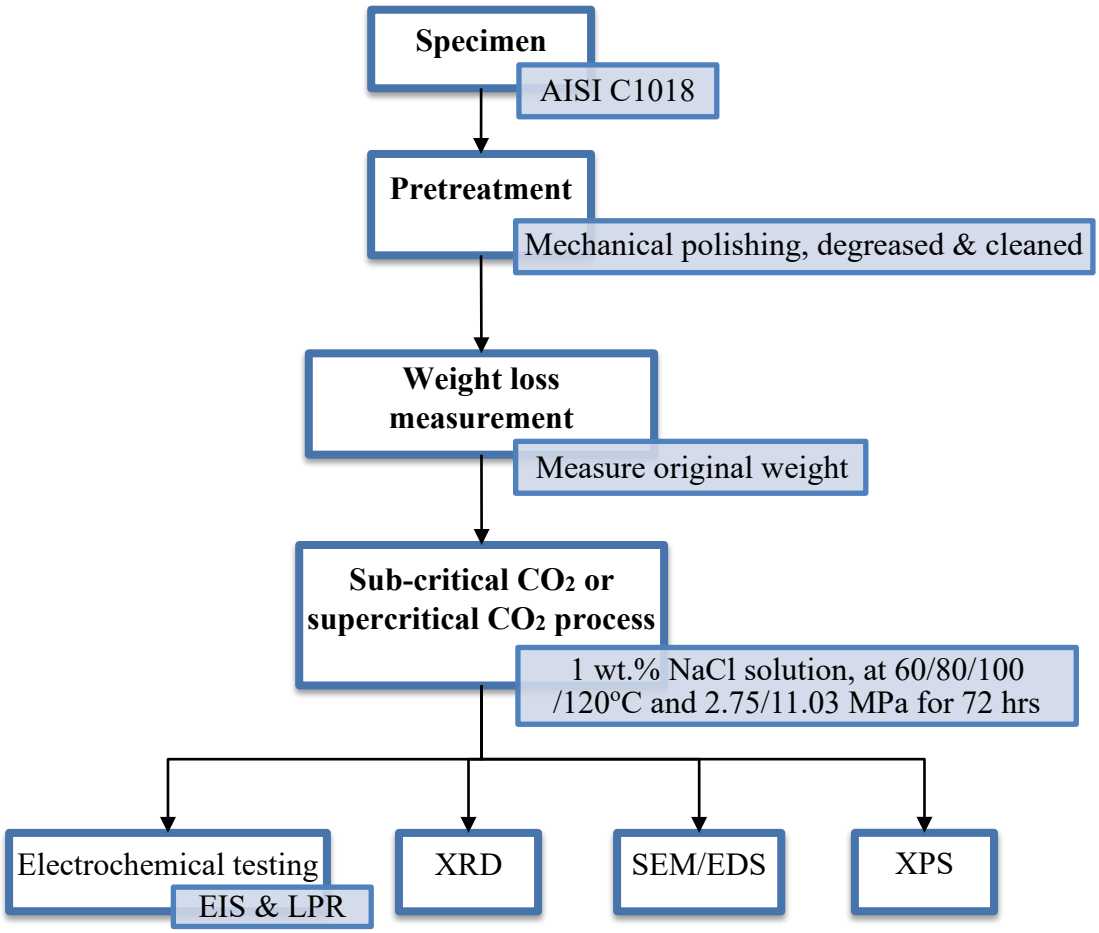

Figure 11: Experimental flow chart of sub-critical and supercritical CO_2 testing.

3.2.2. Electrochemical Measurements

Electrochemical Impendency Spectroscopy (EIS) and Linear Polarization Resistance (LPR) were employed as electrochemical measurements to study corrosion behavior. Both of them were performed with a three-electrode system configuration in the autoclave vessel for 72 hours when the sub-critical and supercritical testing were processed and performed on two separate cylindrical carbon steel specimens. In the three-electrode system, AISI C1018 was employed as a working electrode (WE) to study the corrosion behavior, whereas Hastelloy C-2000 alloy was used as a counter electrode. Both

were commercial materials and used broadly, especially in the Oil & Gas industry. The tungsten/tungsten oxide reference electrode was produced in-house previously and proved that the change in the potential had limited susceptibility to weak acidity at high temperature and high pressure.

Open Circuit Potential (OCP) testing was grouped in the series of testing to monitor the steady state of the potential for 30 minutes first before the EIS measurement started. It was applied for both the EIS and LPR testing. The EIS measurement was set up with 10 mV AC perturbations vs. the open circuit potential and in the frequency from 100k Hz to 0.01 Hz. The Linear Polarization Resistance (LPR) was scanned from -0.005 V to 0.005 V vs. the OCP at a scanning rate of 0.1 mV/s.

All specimens, prior to any further material analysis, were cleaned with anhydrous ethanol and de-ionized water after the autoclave test was finished. The final step to store them was to dehydrate them with high purity nitrogen gas and place them in zip lock bags.

3.2.3. Morphology and Microstructure of Mild Carbon Steel

Scanning Electron Microscopy (SEM)

Scanning Electron Microscopy (SEM) was carried out by using a multifunctional benchtop scanning microscope modeled "NeoScope™" JCM-6000 Plus benchtop SEM from JEOL. It was used to observe the surface morphology of the corroded products on top of the cylindrical carbon steel specimen surface. All the images were captured in the mode of Secondary Electron Image (SEI) and in an operation of 5kV as accelerating voltage at an approximate working distance of 13 mm. The images were recorded in resolutions of 1000x and 5000x. Energy Dispersive Spectroscopy (EDS) attached to the

benchtop SEM equipment was used to analyze the chemical composition of the corroded products on the surface of the carbon steel specimens. The function of mapping in the EDS analysis was utilized to show the distribution of elements on the surface identified in different colors.

X-ray Diffraction (XRD)

The crystal structure and phase transformation of the corroded products on the cylindrical carbon steel specimens were illustrated by using X-ray Diffraction (XRD) analysis. It was performed by utilizing a 2-dimensional multi-purpose X-ray diffraction equipment model D8 Discover from Bruker with state-of-the-art in-plane grazing incidence diffraction (IP-GID). Patented twist tube, micro-focus X-ray source (IuS), and PATHFINDER^{Plus} optical feathers were served to align the angle of e-beam to obtain the sample resolution properly. X-ray spectrum was scanned by a copper Kα X-ray source at 40kV and 40 mA, performed from 20^{o} to 100^{o} in 2-theta mode at a scanning rate of 1.33^{o}/m.

X-ray Photoelectron Spectroscopy (XPS)

The XPS spectrum of all specimens was obtained by using the XPS/UPS system with an Argus detector from Omicron, model DAR400. It was equipped with dual Mg/Al X-ray source to perform XPS measurements. The XPS system uses Omicron's 124 mm mean radius electrostatic hemispherical dispersive energy analyzer to perform electron analysis. With a 128-channel micro-channelplate Argus detector, the high sensitivity of the XPS system can snapshot image up to 6 mm x 6 mm as well as line-scan with lateral resolution down to 54 μm. Background noise can be reduced by the equipment of a CN10

charge neutralizer attached to the XPS system, and surface cleaning can be finished by using the a NGI3000 Argon ion sputter gun.

To pursue a better quality of signs, the samples finished at lower temperature like 60°C and 80°C for both sub-critical and supercritical CO_2 environments were scraped from the surface of the corroded carbon steel specimen before used in the XPS analysis. On the other hand, the samples processed at 100°C and 120°C in both environments were submitted to the XPS analysis directly without any post material treatments.

3.3. Experimental Results and Discussions

3.3.1. Morphology and Microstructure Characterization

Scanning Electron Microscopy and Energy-Dispersive Spectroscopy of the Corroded Products in Sub-critical CO_2 condition

Iron-oxidized corrosion products were generated on the surface of the cylindrical carbon steel specimen after the specimen was sealed and processed in both sub-critical and supercritical CO_2 environments for 72 hours. In macro level, the corrosion products were loose and could be easily removed from the surface of the carbon steel specimen at 60 and 80°C. The structure of the corrosion products became more condensed after the temperature was increased beyond 95°C at which temperature a phase transition of iron-oxidized product was expected in low acidic environment with brine solution.

Figure 12 showed surface morphology of the cylindrical carbon steel specimen after it was processed in the sub-critical CO_2 condition at (a)60°C, (b)80°C, (c)100°C, and (d)120°C. The SEM images showed that at all temperatures solid squarish corrosion products were produced on the surface of the specimen in the sub-critical CO_2

environment. At 60ºC, the corrosion products were generated but not sound. It is likely that the low temperature did not provide enough thermal energy for the corrosion products to grow completely in 3 days. As the temperature was increased to 80ºC, the corrosion products became more sound with clear edges and boundaries. In addition, the grain size of the corrosion products were also increased to approximately 5 μm per grain. When the temperature was increased to 100ºC, the grain size of the corrosion products were certainly enlarged to over 8 μm, but the size of each grain was not consistent. Note that the magnification of 100ºC and 120ºC was 1000x while the magnification of 60ºC and 80ºC was zoomed in to 5000x. However, the difference in the magnification did not interfere or affect the direct observation on the corrosion products on the surface of the carbon steel specimen since the size and shape of the corroded product were able to be observed simply and easily with the scale bar shown at the bottom of each image. At 120ºC, it was believed that the grain size of the corrosion products were increased although it was not clearly shown in Figure 12 (d).

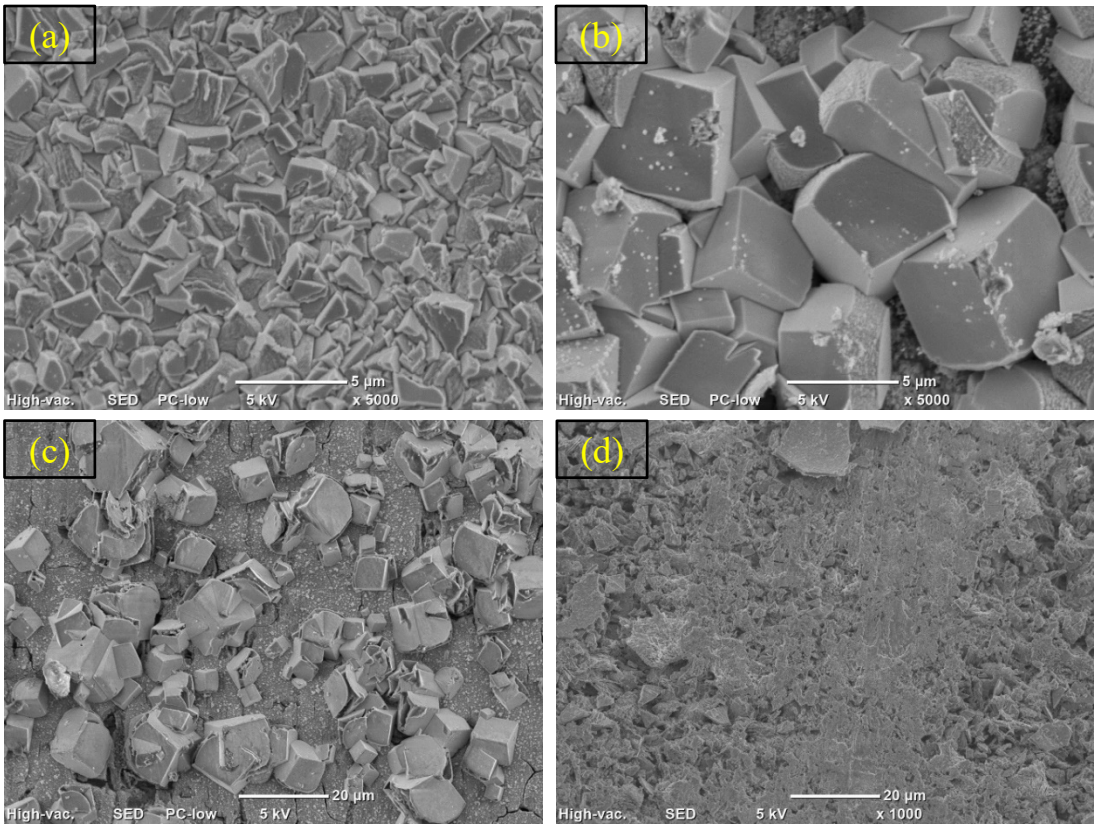

Figure 12: Surface morphology of SEM images of corrosion products processed in a sub-critical CO_2 gas environment at 60°C, 80°C, 100°C, and 120°C.

Figure 13 shows chemical composition of the corrosion products on the surface of the cylindrical carbon steel specimen at 60, 80, 100, 120°C, respectively, in correlation of the SEM images above. The types of elements in every corrosion product at all temperatures is mainly composed of carbon, iron, and oxygen, whereas a fair amount of molybdenum was also shown at 100 and 120°C. The plausible reason that could explain this unexpected phenomenon was contamination from the autoclave vessel body, which in this case was composed of Hastelloy C-2000 alloy (UNS N06200) where the net content of molybdenum was 15-17% by weight. The net amount of each element of the corrosion products were compiled and listed in Table 7 where C 23.65%, Fe 55.95%, and O 20.39%

were contained at 60°C. At all temperatures, the amount of carbon element in the corrosion products was remained consistent with less than one order of fluctuation. In addition, oxygen seemed to decrease from 55.95% to 45.35% as the temperature increased. On the other hand, iron increased to 31.34% from 20.39% when the temperature rose.

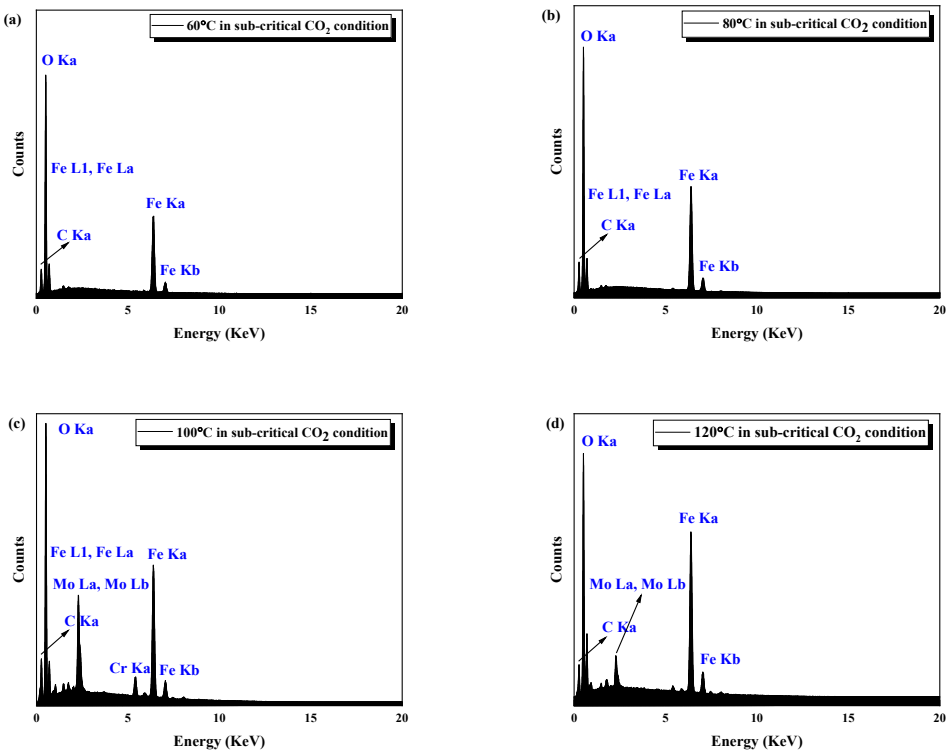

Figure 13: EDS spectrums of corrosion products processed in sub-critical CO_2 gas environment at (a)60°C, (b)80°C, (c)100°C, and (d)120°C.

Table 7: Statistics of chemical composition of the corrosion products on C1018 in sub-critical CO_2 environment at 60°C, 80°C, 100°C, and 120°C.

Temperatures	Atomic percentage (%) of elements		
	Carbon, C	Oxygen, O	Iron, Fe
60°C	23.65	55.95	20.39
80°C	25.42	52.1	22.49
100°C	-	-	-
120°C	23.32	45.35	31.34

Scanning Electron Microscopy and Energy-Dispersive Spectroscopy of the Corroded Products in Supercritical CO_2 condition

Figure 14 shows the surface morphology of the corrosion products generated on the cylindrical carbon steel specimen at various temperatures in the supercritical CO_2 environment. As shown in Figure 14 (a), the grain size of the corrosion products on the specimen were not consistent but became bigger than it was in the sub-critical CO_2 environment. The pressure increasing to 11.03 MPa from 2.75 MPa provided more energy to accelerate the grain growth of the corrosion products created in this circumstance. Although the corrosion products were covered by anonymous particles distributed over the surface, some grains of the corrosion products were still able to be observed on the surface of the cylindrical carbon steel specimens at 120°C in Figure 14 (d).

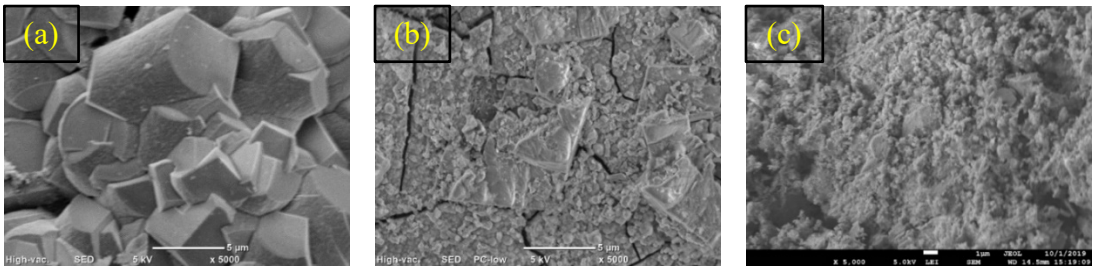

Figure 14: Surface morphology of SEM images of corrosion products processed in supercritical CO_2 gas environment at (a)60°C, (b)100°C, and (c)120°C.

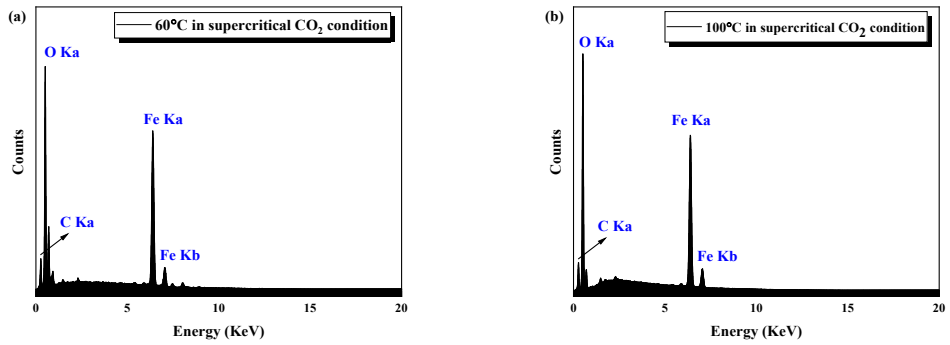

Figure 15: EDS spectrums of iron oxide corrosion products processed in sub-critical CO_2 gas environment at (a)60°C and (b)100°C.

Table 8: Statistics of chemical composition of the corrosion products on C1018 in supercritical CO_2 environment at 60°C, 80°C, 100°C, and 120°C.

Temperatures	Atomic percentage (%) of elements		
	Carbon, C	Oxygen, O	Iron, Fe
60°C	24.96	43.18	29.98
80°C	-	-	-
100°C	23.55	46.21	30.24
120°C	-	-	-

X-ray Diffraction Analysis of the Corroded Products in Sub-critical & Supercritical CO_2 conditions

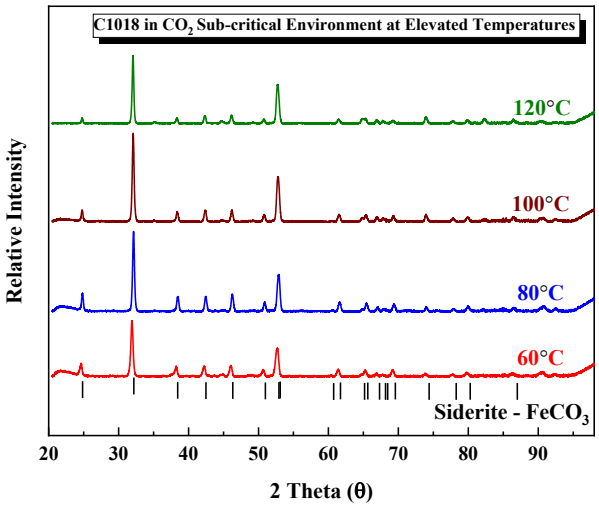

Figure 16: X-ray diffraction spectrums of the corrosion products on C1018 processed in sub-critical CO_2 environment at 60°C, 80°C, 100°C, and 120°C.

Figure 16 presents the XRD spectrum of the corrosion products generated on the surface of the cylindrical carbon steel specimen in the sub-critical CO_2 environment. All XRD spectrums at 60, 80, 100, and 120°C showed identical peak distribution, indicating all the corrosion products at each temperature were the same crystal structure, except for slight difference in peak intensity among some peaks. Three peaks with the strongest peak intensity were located at 24.85°, 32.17°, and 52.92° corresponding to the crystal plane (012), (104), and (018), respectively. As the temperature rose, the peak intensity of the crystal plane (012) decreased, whereas the peak intensity of the other two crystal planes (104) and (018) increased. These changes in peak intensity illustrated that the crystal planes at higher angles favored growth in the sub-critical environment from 60°C to 120°C. Although the variation in temperature altered the peak intensity of the three major peaks, grain size of them seemed not under affected. All the peak locations were examined with ICSD card 100678 and matched with a single type of crystal structure of iron-

oxidized corrosion products named iron carbonate – $FeCO_3$. Hence, all the corrosion products created in the sub-critical CO_2 environment at all temperatures belonged to a single phase, which is well-known as siderite in nature. Due to the dissociation of deionized water and the combination of carbon dioxide (CO_2) with hydroxyl (OH^-), the mixed brine solution provided abundant carbonate ions for the carbon steel specimen to react and form corrosion products. As a matter of fact, the high pressure of the CO2 environment provided plenty of the carbon dioxide to lower the pH value to 3.4 – 3.5 as calculated in OLI simulation software. This experimental condition was beneficial to the production of iron carbonate.

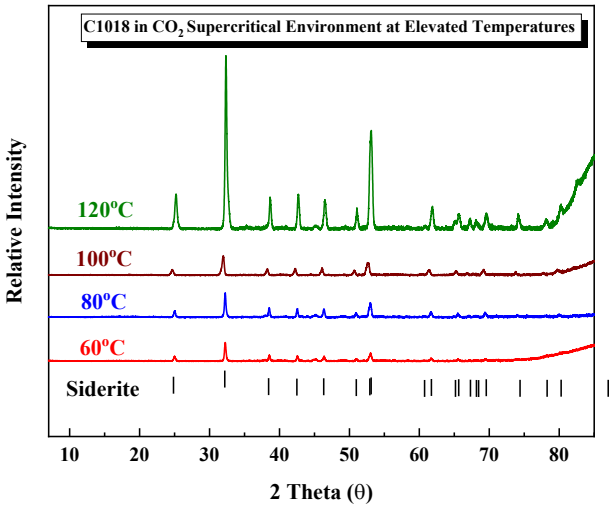

Figure 17: X-ray diffraction spectrums of the corrosion products on C1018 processed in supercritical CO_2 environment at 60°C, 80°C, 100°C, and 120°C.

Figure 17 represents the XRD spectrum of the corrosion products generated on the surface of the cylindrical carbon steel specimen in the supercritical CO_2 environment at 60, 80, 100, and 120°C. The corrosion products produced in the supercritical CO_2

environment at all the temperatures remained consistent compared to the ones in the sub-critical CO_2 environment, which were single phase for the corrosion products. The XRD spectrum indicated that the corrosion products were still iron carbonate without any other forms of iron-related corrosion products created, and that the crystal structure of it was $FeCO_3$ as siderite. As the pressure was increased, the change in peak intensity was not enormously intensified until 120°C, and grain size also seemed enlarged shown in the green line of Figure 17.

X-ray Photoelectron Spectroscopy of the Corroded Products in Sub-critical & Supercritical CO_2 conditions

Figure 18 shows the XPS spectrums of the corrosion products created on the surface of the carbon steel specimen in sub-critical CO_2 environment at 60°C, 80°C, 100°C, and 120°C, respectively for (a) whole spectrum, (b)iron, and (c)carbon elements. In Figure 18 (a), peaks shown at 712 eV and 724 eV represent the electronic orbital Fe 2p of iron element while peaks at 284 eV and 531 eV reveal carbon 1S (C 1S) and oxygen 1S (O 1S) electronic orbitals, respectively. In Figure 18 (b), a close-up observation of iron element was scanned from binding energy of 702 eV to 732 eV, detecting two broad peaks at 711.4 eV and 725.0 eV. The former peak at binding energy 711.4 eV illustrated that it belongs to the electronic orbital of Fe $2p_{3/2}$, and the later one at 725.0 eV reveals the characteristic value of Fe $2p_{1/2}$.

In Figure 18 (c), a pronounced and a broad peaks were observed at 285.0 eV and 289.2 eV, respectively, associated with carbon-carbon single bond (C-C) and carbon-oxygen double bond (C=O); the former bond was correspondent to iron carbonate, and the

later was the result of the hydrocarbons adsorbed on the surface of the carbon steel specimen. The combination of the peaks from the iron and carbon spectrums is the evidence of the formation of the iron carbonate in the sub-critical CO_2 condition which was de-aerated and full of carbon dioxide gas. The result was in agreement with the XRD result, shown in Figure 16.

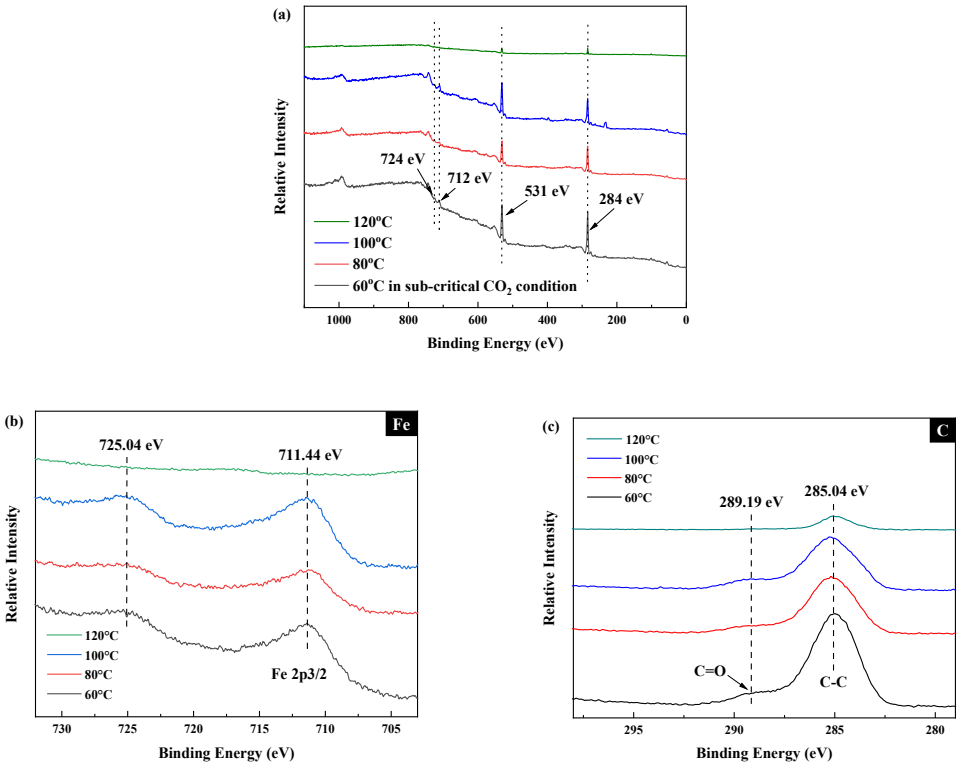

Figure 18: XPS spectrums of the corrosion products on C1018 processed in sub-critical CO_2 environment at 60°C, 80°C, 100°C, and 120°C.

Figure 19 shows the XPS spectrums of the corrosion products created on the surface of the carbon steel specimen in supercritical CO_2 environment at 60°C, 80°C, 100°C, and 120°C, respectively for (a) whole spectrum, (b)iron, and (c)carbon elements. As expected, all the spectrums related to the supercritical CO_2 condition illustrated the

same peak locations as the peaks populated in sub-critical CO_2 condition. The peaks linked with the same characteristic binding energy, matching the correspondent electronic orbitals of shown elements, which meant that peaks shown at 712 eV, 724 eV, and 742 eV represented the electronic orbital Fe 2p of iron element, whereas peaks distributed at 284 eV and 531 eV depicted carbon 1S (C 1S) and oxygen 1S (O 1S) electronic orbitals, respectively. The peak shown at 742 eV contributed to the electronic orbital of Fe $2p_{5/2}$.

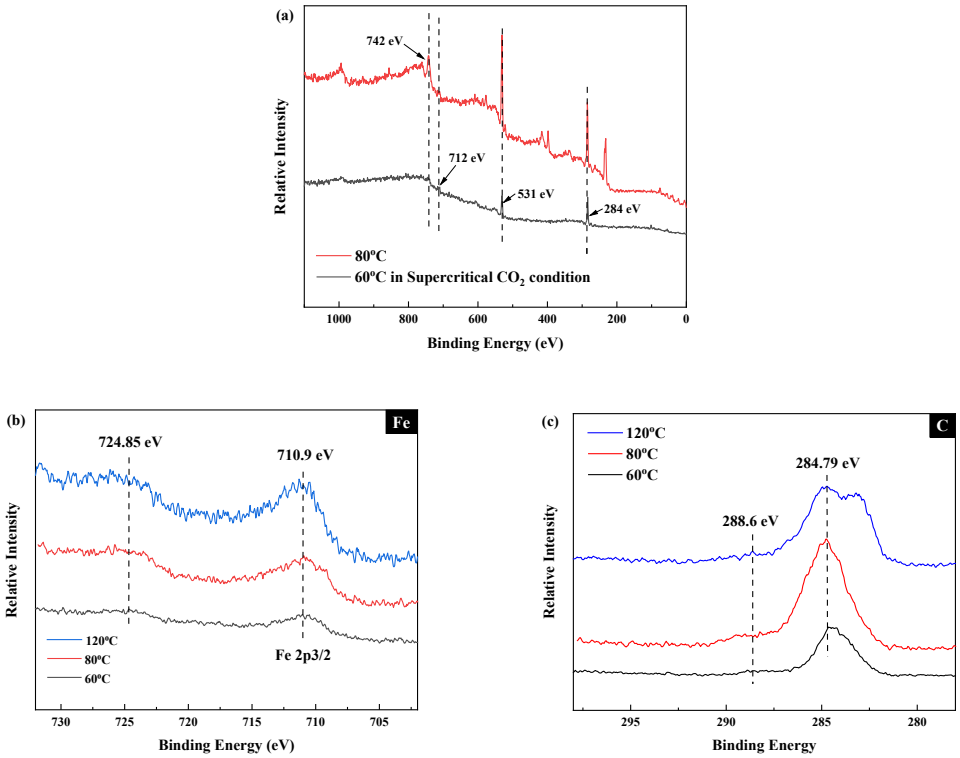

Figure 19: XPS spectrums of the corrosion products on C1018 processed in sub-critical CO_2 environment at 60°C, 80°C, 100°C, and 120°C.

In Figure 19 (b), a zoom-in scanning for iron element was performed from binding energy of 702 eV to 732 eV as the same range in sub-critical CO_2 condition, detecting two broad peaks at 710.9 eV and 724.85 eV. The former peak at binding energy 710.9 eV

belonged to the electronic orbital of Fe $2p_{3/2}$, and the latter one at 724.85 eV revealed the characteristic value of Fe $2p_{1/2}$.

In Figure 19 (c), a pronounced and a broad peaks were observed at 284.79 eV and 288.6 eV, respectively, associated with carbon-carbon single bond (C-C) and carbon-oxygen double bond (C=O); the single bond was correspondent to iron carbonate, and the double bond was the result of the hydrocarbons adsorbed on the surface of the carbon steel specimen. The combination of the peaks from the iron and carbon spectrums was evidence of the formation of iron carbonate in the supercritical CO_2 condition which was de-aerated and full of carbon dioxide gas. The result was in the agreement with the XRD result, shown in Figure 17. Interestingly, a peak at lower binding energy of 282.95 eV was detected at 120°C.

3.3.2. *In-situ* Corrosion Behavior of C1018

Linear Polarization Resistance of Sub-critical CO_2 and Supercritical CO_2 Conditions

Figure 20 shows the variation of corrosion rate and open circuit potential (OCP) on carbon steel at (a)60, (b)80, (c)100, and (d)120°C in a sub-critical CO_2 environment for over 72 hours of exposure in 1 wt.% sodium chloride solution. Both corrosion rate and open circuit potential presented same tendency at all temperatures. Among all of the graphs in Figure 20, the open circuit potential of the carbon steel was increased over time while the corrosion rate of carbon steel was decreased. The increase in the open circuit potential of the corrosion monitoring indicated that the surface reaction of the carbon steel specimen became more noble as it was corroded, and the corrosion products was more protective and CO_2-corrosion-resistive than the original steel surface in the environment

full of CO_2 gas. Such phenomenon was considered the result of the produced corrosion products covered on the surface of the carbon steel specimen, which is in the agreement with the XRD analysis (shown in Figure 16), confirmed as iron carbonate ($FeCO_3$). Hence, the iron carbonate corrosion products provided a protective film covering the steel surface, reducing the corroded spots, and lowering the corrosion rate at the same time.

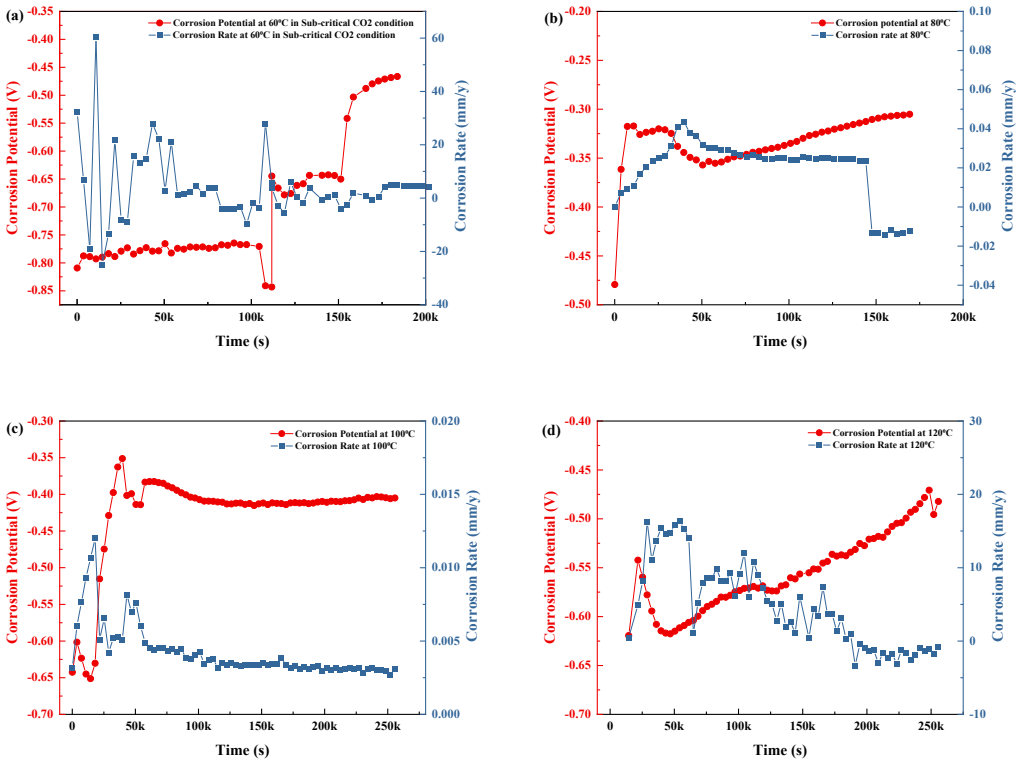

Figure 20: Corrosion potential and corrosion rate of C1018 in sub-critical CO_2 environment at (a)60ºC, (b)80ºC, (c)100ºC, and (d)120ºC.

Figure 21 shows the variation of the corrosion rate and open circuit potential (OCP) on carbon steel at (a)60ºC, (b)80ºC, (c)100ºC, and (d)120ºC in supercritical CO_2 environment for over 72 hours of exposure in 1 wt.% sodium chloride solution. Both the corrosion rate and open circuit potential of the C1018 in the supercritical CO_2 condition, as expected, presented the same inclination as the ones in the sub-critical CO_2 condition

at all temperatures; the increase in potential and the decrease in corrosion rate as the time progressed to the third day. In the beginning of each temperature, the corrosion rate was high and decreased over time. This was due to the same reason as in the sub-critical CO_2 condition - the formation of iron carbonate covering the steel surface as a protective layer.

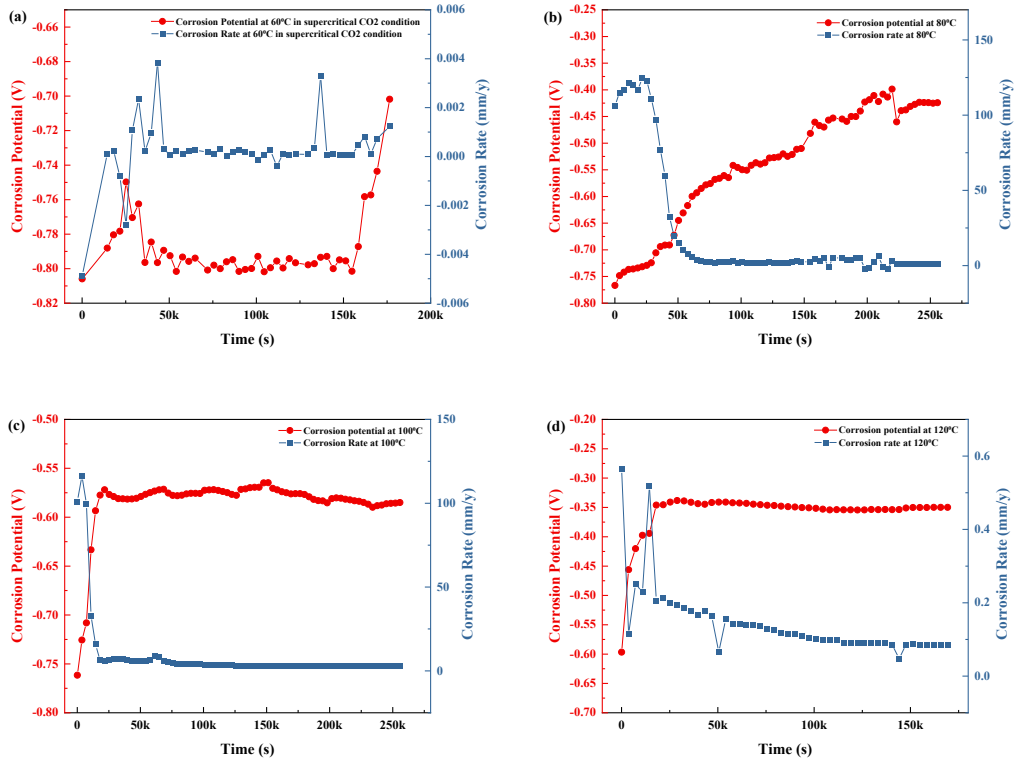

Figure 21: Corrosion potential and corrosion rate of C1018 in supercritical CO_2 environment at (a)60ºC, (b)80ºC, (c)100ºC, and (d)120ºC.

Figure 22 shows experimental and theoretical values of corrosion rate on C1018 in sub-critical CO_2 and supercritical CO_2 conditions from 25ºC to 150ºC. The theoretical values of the corrosion rate on carbon steel - C1018 were simulated at 2.76 MPa (sub-critical CO_2 condition) and 11.03 MPa (supercritical CO_2 condition) from 25ºC to 150ºC via the help of OLI simulation software. It is worth noting that the corrosion rate in the supercritical CO_2 condition is hard to monitor since the fluid droplets were so subtle that

it was not easy to form a good connection for the detection of the electric signal. Despite the corrosion spots where no electric signal output was detected, the simulated result depicted that the corrosion rate in both environments followed the same trend; increase in the corrosion rate from 25°C to 60°C, reaching the climax of the corrosion rate at 65°C, and a decrease in corrosion rate afterwards (70°C to 150°C). At lower temperatures (from 25°C to 55°C), the corrosion rate presented the same values in both low and high partial pressure of CO_2 conditions. However, the highest corrosion rate observed at 65°C in sub-critical CO_2 condition was slightly lower (1.365 mm/y) than the one in supercritical CO_2 condition (1.4318 mm/y). This was attributed to the high partial pressure of CO_2 gas in the supercritical CO_2 condition. As the temperature rose above 70°C, the corrosion rate started decreasing and reached a stable value.

The experimental values of the corrosion rate in the supercritical CO_2 condition showed the same tendency as the theoretical value computed by the OLI simulation software. However, it seemed that the entire variation for corrosion rate was postponed as the highest corrosion rate occurred at 100°C, not at 65°C predicted by theory. Here it is assumed that a hysteresis effect related to phase transformation took place on the steel surface.

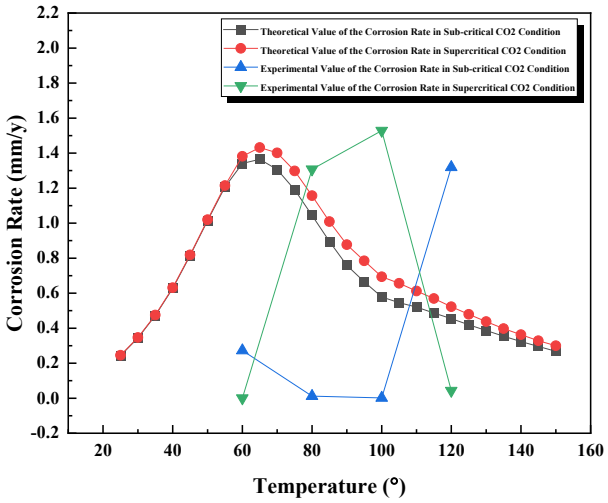

Figure 22: Experimental and theoretical values of corrosion rate on C1018 in sub-critical CO_2 and supercritical CO_2 conditions from 25°C to 150°C.

Table 9: Comparison of real corrosion rate with theoretical value at 60°C, 80°C, 100°C, and 120°C in sub-critical and supercritical CO_2 environments.

Environmental Conditions	Pressure (psi)	Temperature (°C)	Real Corrosion Rate (mm/y)	Theoretical Corrosion Rate (mm/y)
Sub-critical CO_2	400 (2.76 MPa)	60	0.2724	1.3409
		80	0.0119	1.0443
		100	0.0018	0.5783
		120	1.3189	0.4545
Supercritical CO_2	1600 (11.03 MPa)	60	2.5×10^{-5}	1.3814
		80	1.3075	1.1572
		100	1.5284	0.6936
		120	0.0432	0.5224

Electrochemical Impendence Spectroscopy of Sub-critical and Supercritical CO_2 Conditions

Due to the complexity of the simulated harsh environment, it was unfortunate that some Nyquist plots such as the final stage at 80°C, shown in Figure 23 (b), as well as the

middle and final stages at 100ºC, shown in Figure 23 (c), were complicated or unavailable to be analyzed as EIS testing usually required high demand on the environment it was performed on or pursue a highly stabilized condition at a dynamic equilibrium. Unluckily, either the water-saturated sub-critical or supercritical CO_2 environment is well-known as a harsh environment where multiple corrosion and chemical reactions can take place spontaneously and interact with each other. The difficulty of EIS testing also happened in the water-saturated supercritical CO_2 condition on the measurement performed in (a) the middle and final stages at both 60ºC (Figure 24 (a)) and 100ºC (Figure 24 (c)).

Water-Saturated Sub-critical CO_2 Condition

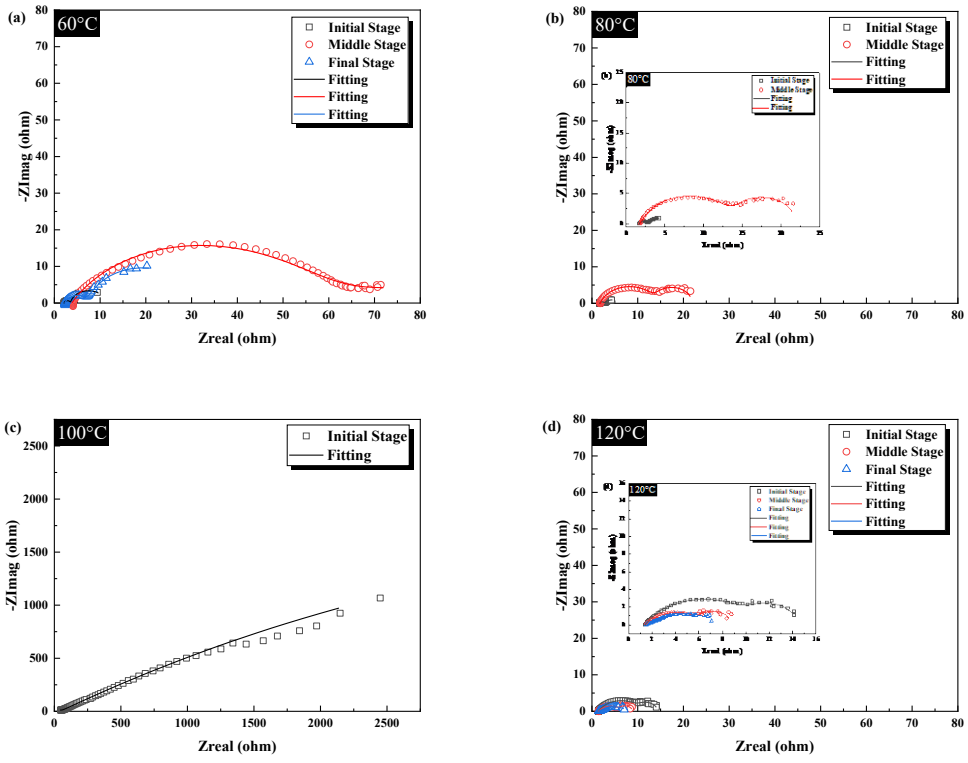

Figure 23: Nyquist plots of C1018 in sub-critical CO_2 condition at (a)60ºC, (b)80ºC, (c)100ºC, and (d)120ºC for 3 days.

Figure 23 shows the Nyquist plots of C018 processed in the sub-critical CO_2 condition at (a)60°C, (b)80°C, (c)100°C, and (d)120°C for 3 days. To understand the corrosion behavior on C1018 simply and more intuitively, the Nyquist plots were accordingly classified into three stages: initial stage (0-15 hours), middle stage (15 hours - 50 hours), and final stage (50 hours – 72 hours) based on similar results.

Effect of Time

In the aspect of time response, the Nyquist plots of C1018 in the initial, middle, and final stages depicted 2 double capacitive loops at all temperatures i.e. 60°C, 80°C, 100°C, and 120°C. As time elapsed, the first capacitive loops at the high frequency at (a) 60°C and (b) 80°C were enlarged in the middle period compared to the ones at the high frequency in the initial period, which was mainly caused by the decreased corrosion damage on the carbon steel surface. However, the entire Nyquist plot of C1018 at (d) 120°C behaved a difficulty in terms of evolving tendency compared to the ones at lower temperatures (60°C and 80°C). It seemed continuously shrank as the test progressed to the final stage from the initial one. This phenomenon was attributed to the corrosion product – iron carbonate ($FeCO_3$) generated when CO_2 corrosion was dominating the system. It is not a secret that iron carbonate corrosion product acted as a passive layer to protect the carbon steel surface, which also reflected the gradual formation of the intermediate-low frequency as time went by at 60°C, 80°C, and 120°C.

Effect of Temperature

At low (60°C and 80°C) and intermediate (100°C) temperatures, the corrosion behavior on C1018 in water-saturated sup-critical CO_2 (SC-CO_2) phase presented two

time constants caused by double capacitive loops; one capacitive loop was in the high frequency, and the other one was in the low frequency. The capacitive loop at high frequency most likely resulted from a double layer capacitance and charge transfer resistance while the other capacitive loop at lower frequency was attributed to corrosion products. Furthermore, as temperature increased, the scale of Nyquist plots of C1018 seemed bigger at low temperature and shrank at intermediate and high temperatures in the SC-CO_2 condition, indicating that high temperature promoted the corrosion of steel. In other words, the corrosion phenomenon became more severe at higher temperatures.

Water-saturated Supercritical CO_2 condition

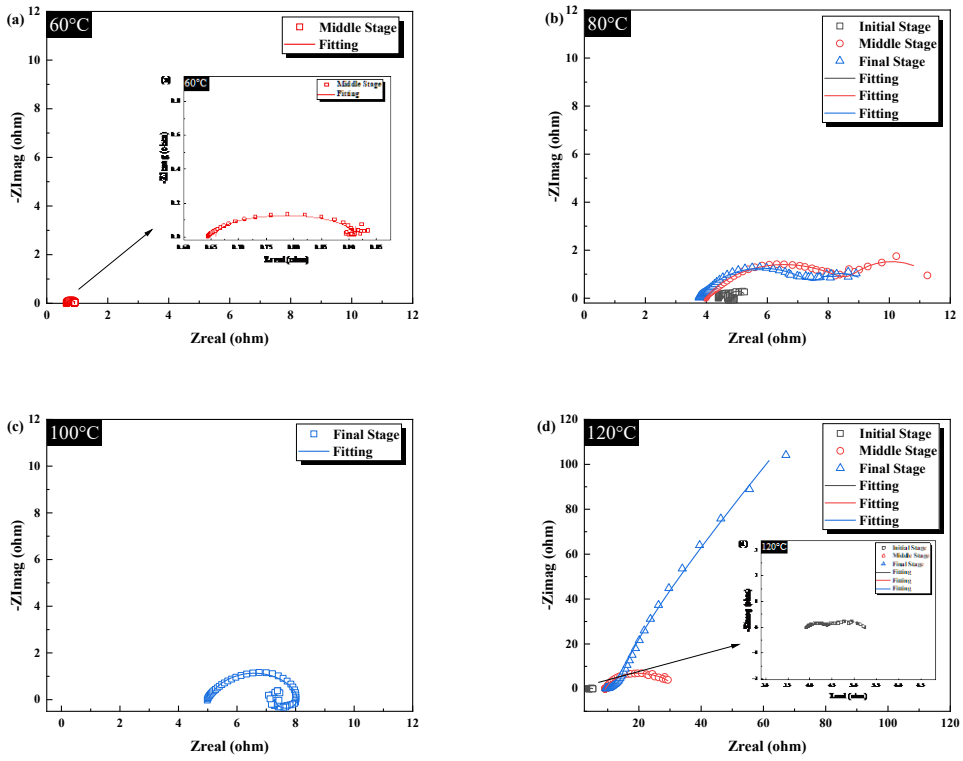

Figure 24: Nyquist plots of C1018 in supercritical CO_2 condition at (a)60°C, (b)80°C, (c)100°C, and (d)120°C for 3 days.

Figure 24 shows the Nyquist plots of C018 processed in supercritical CO_2 condition at (a)60ºC, (b)80ºC, (c)100ºC, and (d)120ºC for 3 days. All the Nyquist plots of C1018 in the water-saturated supercritical CO_2 environment at all temperatures were also subjected to the classification that was used in the water-saturated sub-critical CO_2 condition to organize and rationalize the corrosion mechanism routed for the supercritical CO_2 condition; They were divided into three stages: initial stage (0-15 hours), middle stage (15 hours - 50 hours), and final stage (50 hours – 72 hours) based on similar results.

Effect of Time

The Nyquist plots of C1018 in the water-saturated supercritical CO_2 condition at all temperatures show similar results to the ones of C1018 in the water-saturated sub-critical CO_2 condition at all temperatures; two time constants were present. In other words, double capacitive loops were shown; one was located at the high frequency, and the other one was detected at low frequency. As mentioned above, some of the Nyquist plots were hard or unavailable to be analyzed owing to the severe environment in the water-saturated supercritical CO_2 condition. At 80ºC of the supercritical CO_2 condition shown in Figure 24 (b), the scale of the Nyquist plots seemed enlarged in the middle and final stages compared to the ones in the initial stage as the time propagated. As the capacitive loop at high frequency was grown, it was usually explained by the reason that the steel surface was covered by a passive layer, which here was the iron carbonate corrosion product, same as the one created in the sub-critical CO_2 condition. The iron carbonate corrosion product gradually isolated the steel surface from directly contacting the solution as it was created continuously on the surface. The less the steel surface was in contact with the solution, the

smaller the corrosion rate of the steel surface became. So, it was not hard to understand that the corrosion rate was decreased in the elongated period of immersing time in the acidic solution where the CO_2 corrosion was dominating the system with the protection of the $FeCO_3$ passive layer. On the second capacitive loop at low frequency, it contributed to the formation of the $FeCO_3$ thin film. As the time elapsed, the second capacitive loop became sounder and more mature, which meant that more $FeCO_3$ corrosion product was created as a second layer and covered the steel surface.

In addition, in the Nyquist plot of C1018 at 120ºC shown in Figure 24 (d), a significant scale change in the second capacitive loop at low frequency was detected in the final stage by comparison with the one at 80ºC (Figure 24 (b)). It was attributed to the compact and protective $FeCO_3$ corrosion product covering on the steel surface, so the scale of the second Nyquist semicircle was enlarged. With that being said, the compact $FeCO_3$ passive layer, covered densely on the surface, provided a great protection for the surface and prevent it from being corroded. Hence, it largely slowed down the corrosion reaction in the system.

Effect of Pressure

The effect of pressure was found by comparing the EIS results from the water-saturated sub-critical CO_2 condition (Figure 23) and supercritical CO_2 condition (Figure 24). It was understood that the high partial pressure of CO_2 applied in the water-saturated supercritical environment basically didn't create an essential change in the damage mechanism of CO_2 corrosion, demonstrated in the EIS results of both sub-critical and supercritical CO_2 conditions above. Both of them presented two time constants in the

Nyquist plots from the available data. In both the equivalent circuits, the model that fit the corrosion mechanism for the sub-critical CO_2 environment was composed of two constant phase elements, whereas the supercritical CO_2 environment was fit with the model constituted by a constant phase element and a capacitor.

3.3.3. Discussions

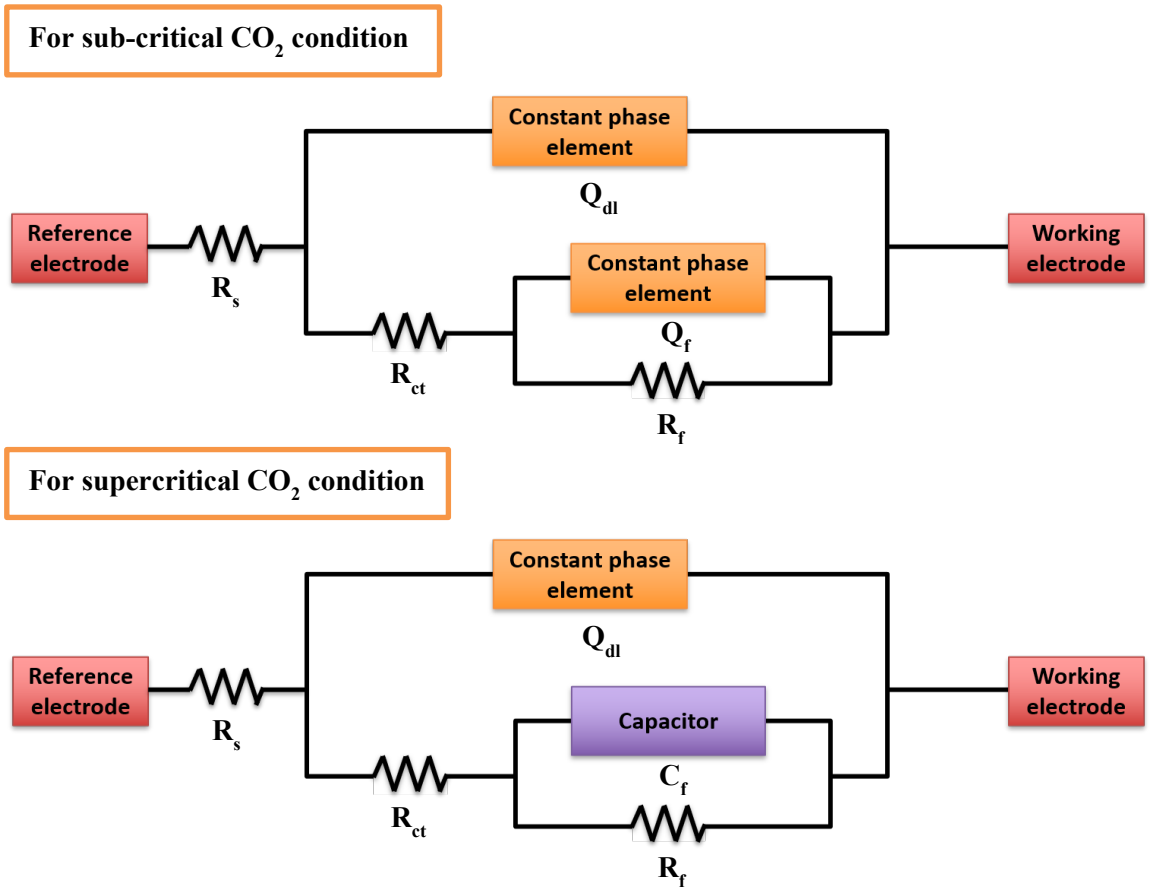

Figure 25: Simulated equivalent circuits of the corrosion products on C1018 in water-saturated sub-critical and supercritical CO_2 conditions.

In Figure 25, R_s is the solution resistance, R_{ct} is the charge transfer resistance, R_f is the resistance of the corrosion product film, Q_{dl} is the constant phase element (CPE) which serves as the resistance of double layer, Q_f is the constant phase element (CPE) that

represents the capacitance of corrosion product film for water-saturated sub-critical CO_2 condition. For water-saturated supercritical CO_2 condition, R_s is the solution resistance, R_{ct} is the charge transfer resistance, R_f is the resistance of the corrosion product film, Q_{dl} is the constant phase element (CPE) which serves as the resistance of double layer, C_f is defined as the capacitor of the corrosion product.

It is important to highlight that either one of the constant phase elements had no integer power dependence on frequency, so any of them were used to serve as the capacitance of a double layer and its corrosion scale, explaining the deviation of an ideal capacitive behavior from the material of interest. Factors such as roughness, inhomogeneous surface topography, and adsorption effects of ions could be seriously considered. The impedance of the constant phase angle was derived by the following equation:

$$\boldsymbol{Z_{CPE} = \frac{1}{Y_0}(j\omega)^{-n}} \quad \textbf{(20)}$$

Where Y_0 is a proportional factor, $j = \sqrt{-1}$, ω is equivalent to $2\pi f$, and n is defined as the dispersion coefficient that is ascribed to inhomogeneous surface level. Two cases would be interpreted based on the value of n:

Case 1: if $n = 0$, then $Z_{CPE} = Y_0^{-1} = R$ $\Rightarrow$ in which the constant phase element becomes a resistance.

Case 2: if $n = 1$, then $Z_{CPE} = Y_0 = C$ $\Rightarrow$ in which the constant phase element is considered as a capacitor.

In our case, the severe corrosion damage from the water-saturated supercritical CO_2 condition was well-explained by this theory.

3.4. Conclusion

- The sub-critical CO_2 and supercritical CO_2 environments present similar corrosion mechanisms without any significant change in between.
- In the supercritical CO_2 environment, iron carbonate ($FeCO_3$) corrosion product dominated the system at 120°C; the formation of the $FeCO_3$ thin film offered a protection layer on the contact surface and lowered the corrosion rate gradually as time passed.
- The severe supercritical CO_2 environment caused a porous structure on the steel surface, making the surface more susceptible to accumulate ions and electrons, which resulted in capacitor performance for the material.

3.5. References

1. Heuer, J.K. and J.F. Stubbins, *An XPS characterization of FeCO3 films from CO2 corrosion.* Corrosion Science, 1999. **41**(7): p. 1231-1243.

4. CORROSION BEHAVIOR ON MILD CARBON STEEL C1018 IN SUPERCRITICAL CO_2 ENVIRONMENT WITH THE EFFECT OF H_2S

4.1. Motivations and Objectives

H_2S corrosion is as important as CO_2 corrosion in oil and gas fields. Such corrosion takes place in a wet environment where a level of H_2S gas is present. With the existence of H_2S gas in a CO_2 environment, it is called a sour environment compared to a sweet environment which contains gaseous CO_2 only. The presence of H_2S will cause numerous serious damage on materials like hydrogen blistering (HB), hydrogen induced cracking (HIC), sulfide stress cracking (SSC), and stress-oriented hydrogen induced cracking (SOHIC), especially on carbon steel and low alloy steels [1]. Although corrosion-resistive alloys (CRAs) are supposedly a better candidate of materials to construct facilities including pipelines and instruments based on safety concerns, economically carbon steels are more popular materials due to cost efficiency. In the past few decades, many oil and gas fields have been exploited with considerable amounts of CO_2 and H_2S injected to the steel-made piping and facilities to help promote more production of crude oils extracted underground for financial reasons. Pipelines and facilities at the same time also encounter great threat because of the potential H_2S corrosion, which would lead to integrity failure and cost more money because of economic loss. Sometimes assets would last for decades, but disasters also can happen just in hours.

With the help of advanced technologies nowadays, CO_2/H_2S corrosion has been widely studied in terms of its corrosion mechanism and behavior in a CO_2 environment

with the addition of H_2S gas in laboratories [2]. However, a number of questions to the CO_2/H_2S corrosion in supercritical state remain unanswered, especially the corrosion behavior in the system with the co-existence of CO_2 and H_2S gas as well as the synergetic effect of H_2S corrosion with CO_2 corrosion. It is known that the corrosion process is an electrochemical reaction involving electrons transferred from material to solution, from one species to another, and from an original exposed surface to corrosion products. It is necessary to investigate electrochemical properties through electrochemical measurements. Many researchers investigated corrosion behavior, kinetics, and materials microstructure of carbon steels in a non-supercritical CO_2/H_2S environment by using the Weight Loss method and Linear Polarization Resistance method. However, the issue about the corrosion behavior in supercritical CO_2 environments with the presence of H_2S is little touched as various chemical reactions happened spontaneously at the same time and interact with each other, resulting in a more complex environment to analyze.

This chapter was designed to focus on studying the real-time corrosion behavior in the supercritical CO_2 environment with various H_2S concentrations from 5ppm, 50 ppm, 100 ppm, and 200 ppm at elevated temperatures like 60ºC, 80ºC, 100ºC, and 120ºC. The variation of the corrosion rates on mild carbon steel C1018 with exposure time, temperature, pressure, and H_2S concentration were monitored by Linear Polarization Resistance and Electrochemical Impendence Spectroscopy. Final corrosion rates of C1018 were confirmed with the Weight Loss method. The surface morphology and microstructure of the corrosion products on the steel surface were investigated by Scanning Electron Spectroscopy and X-ray Diffraction analysis, respectively.

4.2. Research Background

4.2.1. Introduction of H_2S corrosion

H_2S corrosion is induced by hydrogen sulfide (H_2S), which is a common species naturally existing in the reservoirs of natural gas [3]. It is easy to dissolve in an aqueous medium to form a weak acid (Equation (21), which can aggressively attack materials, causing corrosion on the surface (Equation (22) and (23). Equation (21) is a direct hydration from gaseous hydrogen sulfide into aqueous hydrogen sulfide. The process is considered as the dominant cathodic reaction among all the other reactions happening on a cathode.

$$\boldsymbol{H_2S_{(g)} \leftrightarrow H_2S_{(aq)}} \quad \textbf{(21)}$$

$$\boldsymbol{H_2S_{(aq)} \leftrightarrow HS^-_{(aq)} + H^+_{(aq)}} \quad \textbf{(22)}$$

$$\boldsymbol{HS^-_{(aq)} \leftrightarrow S^{2-}_{(aq)} + H^+_{(aq)}} \quad \textbf{(23)}$$

Factors triggering and aggravating H_2S corrosion are multifold; level of H_2S [4], impurity concentration, and NaCl concentration are equally important as environmental parameters such as pH, temperature, and pressure while material property like hardness is also primarily related to sulfide stress cracking, a mechanical form of corrosion. Hydrogen permeation would happen at lower pH (pH < 4) and higher (pH > 7.6) with a low level of H_2S concentration whereas diffusion rate of H_2S would be found minimal at pH 7. As for the H_2S concentration, a high partial H_2S pressure would lead to an increase in hydrogen permeation. Temperature-wise, blistering or cracking-related issues (HIC and SOHIC) would take place from ambient temperature to 150°C (300°F) and higher, and SSC generally was found below 82°C (180°F). Typically, an arbitrary value of 50 wppm H_2S

in water phase is often used as a rule of thumb to define whether wet H_2S damage becomes a problem or not in American Petroleum Institute (API) 571 RP. However, Ma et. al in 2000 reported that [5] a low H_2S concentration of ≤ 0.04 mmol/dm^{-3} inhibited corrosion rate under a restricted condition of pH 3-5 in a long exposure time. Abelev et al. [6] also reported an inhibition effect on corrosion with 5 ppm of H_2S in the supercritical CO_2 environment. While no absolute criterion about level of H_2S has been reported to affect corrosion, it is understandable to take other environmental factors into account as well.

As reported elsewhere [4], H_2S species was considered as a dual role in a CO_2 environment. While trace amount of H_2S species would instantly form an iron sulfide (FeS) layer to protect the exposed surface, a high amount of H_2S concentration also would promote corrosion process, speeding up the corrosion rate. It was suggested that the alternative result was determined by the partial pressure of H_2S - either an inhibited effect or a catalyst effect. Flow rate was the reason to explain the phenomenon. Furthermore, it was reported that when H_2S concentration was below 690 Pa, a protective iron sulfide film would be formed whereas a non-protective film would be created once the concentration exceeded 690 Pa [7-9]. On the other hand, some researchers indicated that the dominant cathodic reaction might be the direct hydration of H_2S [10-14] and Kahyarian and Nesic [15] more recently reported that H_2S also played as a buffering role in the corrosion process of a relative sweet environment.

Abadeh and Javidi [3] investigated the effects of sodium chloride concentration and hydrogen sulfide gas concentration at various temperatures on four types of microstructure of API 5L X52 carbon steel electrochemically; be it annealed, normalized, normalized-

tempered, and quench-tempered. At low temperatures (40°C and 60°C), the kinetics of corrosion behavior formation was somewhat limited. The presence of 100 ppm of H_2S gas resulted in creating FeS as corrosion products, which forbad corrosion rate. However, an increase in corrosion rate was observed with 200 ppm of H_2S addition because of the formation of defects in the corrosion products.

Gao et al. [2] studied the corrosion rate on API X65 carbon steel under the effect of H_2S at different temperatures in sub-critical CO_2 environment.

Choi et al. [4] studied the effect of H_2S on C1018 mild carbon steel in 1 wt.% NaCl solution at 25°C and atmospheric pressure in pH 3 and pH 4 conditions. 100 ppm of H_2S gas introduced an inhibition effect to C1018 mild carbon steel and rapidly decreased the corrosion rate because of the formation of iron sulfide (FeS) thin film grown on the steel surface, which suppressed the anodic dissolution reaction. The precipitation of iron sulfide as well as iron carbonate film is possible in the acidic solutions due to the local supersaturation in regions immediately above the steel surface, and these films provide corrosion protection in the acidic solutions.

Asadian [16] studied the corrosion behavior on ASTM-106 in co-existence of CO_2 and 200 ppm H_2S (not supercritical condition). ASTM A-106 was used to transport oil and gas in the presence of H_2S and CO_2 at different temperatures (25~85°C), 3 wt.% NaCl. Temperature increased corrosion rate of the steel, and the presence of CO_2 and H_2S enhanced the corrosion rate. Iron carbonate and iron sulfide didn't have sufficient stability at high temperature to protect the metal surface against corroding agents, and they couldn't form a uniform coating on the steel surface. The corrosion rate is high with the presence

of CO_2 and H_2S at high temperatures. The corrosion potential decreased, indicating the whole system became more active and more susceptible to the corrosive environment. However, the author did not provide information about pH value and the partial pressure of CO_2. So, the EIS result did not show signal of any other corrosion products, but only the signal of double layer, which is contradicted to our observation.

Santos et. al. [17] studied the effect of sodium chloride on API X65 carbon steel with and without sodium thiosulfate in different concentrations of brine solution at 90ºC and 120ºC in 1 bar of CO_2 environment and confirmed that sodium thiosulfate could be used as a chemical source to generate H_2S gas, which was proven by their XRD result (not supercritical condition). At 120ºC with the existence of sodium thiosulfate, mackinawite, greigite, and pyrite were the corrosion products formed on the surface of the carbon steel and possessed protective properties to lower the corrosion rate. 0.1 wt.% and 3.5 wt.% NaCl.

4.2.2. H_2S Solubility, Dissociation, and its Sulfide Products

H_2S corrosion is largely related to the nature of rapid H_2S solubility. Gaseous hydrogen sulfide (H_2S) possesses characteristics of instant solubility and partial dissociation when it contacts a water solution in which H_2S dissociation usually can be broken into two steps. Equation (24) to (26) present reactions corresponding to H_2S dissolution and dissociation in a H_2S-H_2O system, where K_{H_2S} is the solubility constants of aqueous H_2S, $K_{a,1}$ and $K_{a,2}$ are the first and second dissociation constants, respectively. Numerous studies proposing differentiated formulas to predict solubility constant [18-22] and dissociation constants of H_2S [23-30] were reviewed by Jing et. al [31] who verified the

formulas by testing mild steels in the range of H_2S concentration from 40 ppm to 8000 ppm at room temperature, 60°C, and 80°C in NaCl solution.

H_2S solubility:

$$\boldsymbol{H_2S_{(g)} \overset{K_{H_2S}}{\Longleftrightarrow} H_2S_{(aq)}} \qquad \boldsymbol{K_{H_2S} = \frac{[H_2S]}{p_{H_2S}}} \tag{24}$$

Two steps of H_2S dissociation:

$$\boldsymbol{H_2S_{(g)} \overset{K_{a,1}}{\Longleftrightarrow} H^+ + HS^-} \qquad \boldsymbol{K_{a,1} = \frac{[H^+][HS^-]}{[H_2S]}} \tag{25}$$

$$\boldsymbol{HS^- \overset{K_{a,2}}{\Longleftrightarrow} H^+ + S^{2-}} \qquad \boldsymbol{K_{a,2} = \frac{[H^+][S^{2-}]}{[HS^-]}} \tag{26}$$

Corrosion products created through H_2S corrosion are polymorphous, depending on the solubility limit, the H_2S concentration and reaction time. It is believed that different forms of the H_2S corrosion products behaved differently in electrochemical properties on steel surface due to their physicochemical features [32], which are listed in Table 10. The polymorphism of H_2S corrosion products, for example, are amorphous iron sulfide (FeS), mackinawite (FeS), pyrrhotite ($Fe_{1-x}S$ [x = 0 ~0.17]), troilite (FeS), greigite (Fe_3S_4), and pyrite (FeS_2), which have been frequently detected as corrosion products on mild carbon steels in laboratory testing involved with H_2S gas. They were also produced in several research facilities in efforts studying the corrosion mechanism of H_2S corrosion [33]. Other forms of H_2S-related corrosion products like cubic ferrous sulfide (FeS), smythite ($Fe_{3+x}S_4$), and marcasite (FeS_2) are not considered because of the sources, conditions, and restricted environments where they are produced.

Table 10: Types of H_2S corrosion-related products and their physiochemical properties.

Types of H_2S corrosion-related products	Chemical formula	Phase	Stability	Remark
Amorphous iron sulfide	FeS	Amorphous, non-crystalized	Unstable	Transform into mackinawite quickly.
Mackinawite	Fe1+xS (x = 0 ~ 0.11)	Tetragonal	Metastable	Initial corrosion product.
Pyrrhotite	$Fe_{1-x}S$ (x = 0 ~ 0.17)	Monoclinic in Fe_7S_8 or hexagonal in $Fe_{10}S_{11}$	Thermodynamic stable	The most abundant iron sulfide existed naturally on Earth.
Troilite	FeS	Hexagonal	Stable	End member of stoichiometric FeS group.
Greigite	Fe_3S_4	Cubic	Metastable	Between Fe^{2+} and Fe^{3+} sulfide
Pyrite	FeS_2	Cubic	Thermodynamic stable	The most abundant mineral existed naturally on Earth.
Cubic ferrous sulfide	FeS	Cubic	Unstable	Only found in very restricted experimental conditions.
Smythite	$Fe_{3+x}S_4$ (x = 0 ~ 0.3)	Trigonal-hexagonal	Metastable	In the category of $Fe_{1-x}S$ group
Marcasite	FeS_2	Orthorhombic	Metastable	common mineral in hydrothermal system and sedimentary

Amorphous Iron Sulfide (FeS)

Amorphous iron sulfide consists numerous short-range orders, which is shown by a broad range of angles with low intensity (a.k.a low crystallinity) in the XRD spectrum. Kornicker [31] suggested that amorphous iron sulfide was a hydrate as its physical properties changed after being dried out. Wolthers [34] determined that amorphous iron sulfide was nanocrystalline mackinawite with crystal size of 2.2 ± 1.7 nm in average. Richard et al. [35, 36] concluded that amorphous iron sulfide did not exist but was nanocrystal mackinawite by using thermogravimetric analysis and nuclear magnetic resonance spectroscopy.

Mackinawite (FeS)

Due to a low solubility limit, it is well-known that mackinawite is considered as the initial corrosion product created in H_2S corrosion and rapidly transforms into other forms of iron sulfides. Mackinawite existed as a two-dimensional crystal structure with

stoichiometric to non-stoichiometric ($Fe_{1+x}S$, x = 0 ~ 0.11) quantity as $Fe_{0.91}S$ [37], $Fe_{1.09-1.15}S$ [38] pyrrite, $Fe_{0.995-1.023}S$ [31], and $Fe_{0.99 \pm 0.02}S$ [31] were found from testing in the laboratory. Rickard and Luther [39] suggested that the observations about the iron-rich mackinawite, $Fe_{1+x}S$, obtained in previous studies resulted from the co-existence of rhombic sulfur. Thus, Richard et al. [35] reported that the previous experimental results about the non-stoichiometric mackinawite compositions ($Fe_{1 \pm x}S$) were involved with analytic artifacts, and they corrected that the real composition of mackinawite were supposed to be stoichiometric.

Greigite (Fe_3S_4)

Greigite is a one of the metastable forms related to the iron sulfide group. It is known as an intermediate phase between mackinawite and final sulfide product during a long exposure period in the presence of H_2S [40].

Pyrrhotite ($Fe_{1-x}S$ [x = 0~0.17]) and Troilite (FeS)

Pyrrhotite and troilite are differentiated only in stoichiometric quantity as the growth path of the crystals deviated below 150°C after nucleation. Troilite can be considered as a stoichiometric type of pyrrhotite at low temperature. Several pyrrhotites with different x values were observed with elevated temperature. Pyrrhotite is a synthetic iron sulfide whose crystal structure is hexagonal and non-stoichiometric ($Fe_{1-x}S$, where x = 0 ~ 0.17) whereas troilite is the stoichiometric end member (FeS) of the pyrrhotite group when x equals 0. Both are thermodynamically stable and can co-exist when the temperature is below 150°C [41]. Troilite exists on Earth abundantly and naturally, and

most of this phase reached equilibrium at earth surface temperature whereas the iron composition of the synthetic pyrrhotite varied with temperature from 25°C to 140°C.

Pyrite (FeS_2)

Pyrite is a natural cubic mineral abundantly existing on Earth, and it is the same as pyrrhotite, the most stable form among the iron sulfide family. Owing to its yellow and greyish luster, it is also known as "fool's gold". It can be created as a corrosion product during a long exposure period to an environment containing H_2S gas. Mackinawite (FeS), greigite (Fe_3S_4), pyrrhotite ($Fe_{1-x}S$), and pyrite (FeS_2) mentioned above are commonly found as the corrosion products on mild carbon steel in a CO_2 environment with the presence of H_2S gas [31]. Thermodynamically predicted by the simplified Pourbaix diagram of the H_2S-H_2O-Fe system shown in Figure 26, mackinawite was identified as the initial corrosion product on mild carbon steel in an aqueous solution containing H_2S in a short exposure time because of its fast precipitation kinetics. As time increased, greigite was produced as an intermediate phase converted from mackinawite at higher potential and could exist in a wider pH range compared to mackinawite while pyrrhotite and pyrite were favored to precipitate after a long exposure time. Note that pyrite, compared with pyrrhotite, was formed at a higher potential in a much wider pH range in an oxygenated solution.

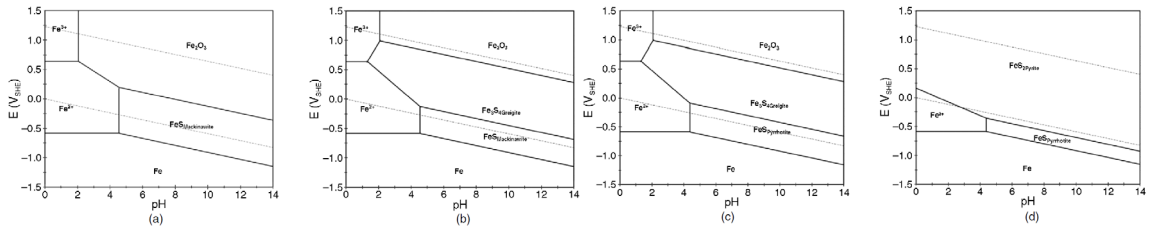

Figure 26: Simplified Pourbaix diagram of H_2S-H_2O-Fe system at 25°C with different polymorphic corrosion products: (a) mackinawite, (b) mackinawite + greigite, (c) mackinawite + greigite + pyrrhotite, and (d) mackinawite + greigite + pyrrhotite + pyrite.

4.3. Experimental Approach

4.3.1. Material Sources and Pretreatment

In the section of this study, mild-low carbon steel (AISI C1018) continued to be used as the material of study to investigate its corrosion behavior under the effect of low concentration of H_2S gas on top of water-saturated supercritical CO_2 condition. The mild carbon steel purchased from Metal Samples (Alabama, USA) was machined into a cylindrical shape with a dimension of 1.72" x 0.25" and a centerless ground. Its chemical composition was 0.14 – 0.2% C, 98.81 – 99.26% Fe, 0.6 – 0.9% Mn, ≤ 0.04% P, and ≤ 0.05% S. It was abraded with silicon carbide paper up to 1000 grit to remove oxides on the surface and decrease the surface roughness and then stored in a desiccator. Before each testing started, the carbon steel samples were degreased with acetone, cleaned with alcohol, and rinsed with deionized water. If any of the specimens were rusted on the surface, it was polished with the highest number of silicon carbide paper again.

4.3.2. Research Scope and Experimental Configuration

The research scope of this study covered low concentrations of H_2S gas from 5 ppm, 50 ppm, 100 ppm, and 200 ppm at 60°C, 80°C, 100°C, and 120°C in 400 psi and 1600 psi, respectively, for sub-critical CO_2 condition and water-saturated supercritical

CO_2 condition for 2 days. The scope of each corrosion test with detailed experimental operating parameters in terms of CO_2 partial pressure, temperature, and concentration of H_2S is shown in Table 11.

Table 11: Research scope of C1018 under the effect of H_2S gas in sub-critical and supercritical CO_2 conditions.

		H_2S concentration			
Water-saturated sub-critical CO_2 condition (400 psi)	60°C	5 ppm	50 ppm	100 ppm	200 ppm
	80°C	5 ppm	50 ppm	100 ppm	200 ppm
	100°C	5 ppm	50 ppm	100 ppm	200 ppm
	120°C	5 ppm	50 ppm	100 ppm	200 ppm
Water-saturated supercritical CO_2 condition (1600 psi)	60°C	5 ppm	50 ppm	100 ppm	200 ppm
	80°C	5 ppm	50 ppm	100 ppm	200 ppm
	100°C	5 ppm	50 ppm	100 ppm	200 ppm
	120°C	5 ppm	50 ppm	100 ppm	200 ppm

In each corrosion test, two out of the four carbon steel specimens were employed as working electrodes in an autoclave system, which was the same equipment used in the previous chapter - an autoclave vessel body and lid, booster pump, temperature control, heating pad, dual thermal and pressure digital monitoring panel, visual standard pressure gauge, venting valves, cooling circulating system, gas-in and gas-out pipelines, and a research grade of carbon dioxide gas cylinder.

A three-electrode system was constructed to carry out the electrochemical measurement in each corrosion test. Each test required four carbon steel specimens; two specimens were electrochemically analyzed in real time by Electrochemical Impendence Spectroscopy (EIS) and Linear Polarization Resistance (LPR) individually. In the three-electrode system, the cylindrical mild carbon steels were used as working electrodes

(WEs) for the electrochemical testing. Hastelloy C-2000 alloy, a corrosion-resistant material from the nickel-chromium-molybdenum alloy family with addition of copper, was used as the counter electrode (CE) and mounted on the second probe. The third probe was mounted with a tungsten/tungsten oxide, which was previously established in the second chapter of this study and was employed as a reference electrode (RE). The positions of the three electrode probes were fixed at a certain distance between them.

The last two specimens were processed solely without any electrochemical testing imposed on them, which later were characteristically being examined by X-ray Diffraction Spectroscopy (XRD), Scanning Electron Microscopy/Energy Dispersive Spectroscopy (SEM/EDS), and X-ray Photoelectron Spectroscopy (XPS) later after the corrosion testing was finished.

Reported elsewhere [42], an estimation of 0.74g (4333 ppmv) of water was dissolved in a 1 liter of supercritical CO_2 condition. In addition, about 0.19 g per gram of H_2S could be lost as the average water loss after purging the air with CO_2 at room temperature for 2 hours. Hence, to ensure saturating the moisture in the supercritical CO_2 environment, 10 g deaerated deionized water was added into the autoclave.

4.3.3. Experimental procedure

Wet chemical solution method

To study the effect of low concentration H_2S gas in a water-saturated supercritical CO_2 environment on the corrosion behavior of mild carbon steel, this chapter explored 5 ppm, 50 ppm, 100 ppm, and 200 ppm of H_2S gas. The procedure of creating the water-saturated supercritical CO_2 environment for Chapter 3 continued to be used in this chapter

to mimic the water-saturated supercritical CO_2 environment. To control the H_2S content precisely in the water-saturated supercritical CO_2 state, this chapter used a wet chemical solution method to produce H_2S gas by dissolving sodium sulfide nonahydrate in 2.8 liters of deionized water with 1 wt.% sodium chloride concentration. This method was proposed not only due to safety concerns but also because of the constant gas dissolution into the fluid as time passed.

In many studies [2, 16], H_2S gas was added in the autoclave vessel by an injection method to study the effect of H_2S on corrosion behavior of mild steel API 5L X65 and ASTM A-106 steel in a supercritical CO_2 environment. However, a problem occurred when the corrosion testing proceeded further, the H_2S gas would continuously dissolve into electrolyte fluid, but it was hard to predict the amount of H_2S gas dissolved in the supercritical CO_2 aqueous phase and calculate how much pressure of H_2S partial was left in the supercritical CO_2 fluid. By using the wet chemical solution method, the solubility of sulfur ion (S^{-2}) was limited in the sodium chloride solution and was able to be calculated.

The amounts of sodium sulfide nonahydrate were calculated by the thermodynamic prediction of OLI software. It provided information including the amount of sodium sulfide nonahydrate needed in 2.8 liters of deionized water to create the desired concentrations of H_2S in each experimental condition of interest, reaction trend and final products of each possible chemical reaction and predicted general corrosion rate at final pH value and potential.

The amounts of sodium sulfide nonahydrate were dissolved in the 2.8 liters of 1 wt.% NaCl solution first before putting it in the autoclave body vessel. After the autoclave was sealed, gas-in and gas-out pipelines were connected to the autoclave body. Highly pure N_2 gas was injected into the sealed autoclave body for 1 hour to purge the air and dissolved oxygen gas from the solution as the temperature was increased to 50ºC slowly. This slow temperature-increasing step helped shorten the time needed for purging but not promote the chemical reaction. After the purging was finished, the temperature (60ºC, 80ºC, 100ºC, and 120ºC) and CO_2 pressure (400 psi and 1600 psi) were increased to the research level of interest in order. The CO_2 cylinder had to be kept open for extra time because the thermodynamic system in the autoclave was not stabilized yet as the CO_2 gas was continuously dissolved in the solution and part of the solution would mix with CO_2 gas to become supercritical CO_2 fluid. In addition, as the CO_2 gas continuously dissolved in the solution, it would bring down the pH to our level of interest and promote the production of H_2S gas by reacting with S^{-2} ion.

The autoclave was filled with 2.8 L of fluid, and sodium chloride (NaCl) was 1% of the solution by weight for conducting the electrochemical testing. Note that due to the experimental design, the actual area of the working electrode immersed in the solution was 1/3 of its calculated surface area, so as the counter electrode and reference electrode. Due to the current limitation of the experimental configuration, no direct pH sensing was available to measure the in-situ pH value during a test. Hence, the pH calculated via OLI software was 3.1 at balance when the partial pressure of CO_2 and the concentration of H_2S gas were increased to the research level of the interest. However, from 5.6-5.9 of pH values

was obtained through a pH meter after the system was depressurized. The increase of the pH value was understandable after the H^+ concentration was consumed through a series of chemical reactions inside; the reduction of iron carbonate and the reduction of iron sulfide.

After every test was finished, the specimens were taken out, rinsed with deionized water, and dried by nitrogen gas. They were then sealed in zip lock bags separately in nitrogen gas and stored in a desiccator. One day later, they were taken out and weighed again by the same electronic scale for Weight Loss measurement.

Weight Loss Method

Weight loss testing was used to study the corrosion rate of mild carbon steel C1018 that was processed in a corrosion testing in a 4 L autoclave system for water-saturated subcritical and water-saturated supercritical CO_2 system with various amounts of H_2S gas. Although the weight loss method could not reflect the instant corrosion rate at each timing point during corrosion test, it could provide a clear picture of how severe the whole system is overall in terms of a thermodynamic perspective.

The weight loss method started with the specimens weighed by using an accurate electronic scale with a precision of 0.001 mg.

$$\boldsymbol{R_G = \frac{87600 \cdot \Delta m}{S \cdot \rho \cdot t}} \qquad \textit{(27)}$$

Where R_G is the general corrosion rate (mm/y); Δm is the weight loss (g); S is the exposure surface area (cm^2); ρ is the density of the mild carbon steel (g/cm^3); and t is the exposure time (h).

Electrochemical testing

Electrochemical Impendency Spectroscopy (EIS) and Linear Polarization Resistance (LPR) were employed as electrochemical measurements to study corrosion behavior. Both were performed with a three-electrode system configuration in the autoclave vessel for 72 hours when the sub-critical and supercritical tests were processed and performed on two separate cylindrical carbon steel specimens. In the three-electrode system, AISI C1018 was employed as a working electrode (WE) to study the corrosion behavior, whereas Hastelloy C-2000 alloy was used as a counter electrode. Both were commercial materials and broadly used, especially in the Oil & Gas industry. The tungsten/tungsten oxide reference electrode was produced in-house previously and proved that the change in the potential had limited susceptibility to weak acidity at high temperature and high pressure.

Open Circuit Potential (OCP) testing was grouped in the series of tests to monitor the steady state of the potential for 30 minutes first before the EIS measurement started. It was applied for both the EIS and LPR testing. The EIS measurement was set up with 10 mV AC perturbations vs. the open circuit potential and in the frequency from 100k Hz to 0.01 Hz. The Linear Polarization Resistance (LPR) was scanned from -0.005 V to 0.005 V vs. the OCP at a scanning rate of 0.1 mV/s.

All specimens, prior to any further material analysis, were cleaned with anhydrous ethanol and de-ionized water after the autoclave test was finished. The final step to store them was to dehydrate them with high purity nitrogen gas and place them in zip lock bags.

Scanning Electron Microscopy (SEM)

Scanning Electron Microscopy (SEM) was carried out by using a multifunctional benchtop scanning microscope identified as the "NeoScope™" JCM-6000 Plus benchtop SEM from JEOL. It was used to observe the surface morphology of the corroded products on top of the cylindrical carbon steel specimen surface. All the images were captured in the mode of Secondary Electron Image (SEI) and in an operation of 5kV as accelerating voltage at an approximate working distance of 13 mm. The images were recorded in resolutions of 1000x and 5000x. Energy Dispersive Spectroscopy (EDS) attached to the benchtop SEM equipment was used to analyze the chemical composition of the corroded products on the surface of the carbon steel specimens. The function of mapping in the EDS analysis was utilized to show the distribution of elements on the surface identified in different colors.

X-ray Diffraction (XRD)

The crystal structure and phase transformation of the corroded products on the cylindrical carbon steel specimens were illustrated by using X-ray Diffraction (XRD) analysis. It was performed by utilizing a 2-dimensional multi-purpose X-ray diffraction equipment model D8 Discover from Bruker with state-of-the-art in-plane grazing incidence diffraction (IP-GID). Patented twist tube, micro-focus X-ray source (IuS), and PATHFINDERPlus optical feathers were served to align the angle of e-beam to obtain the sample resolution properly. X-ray spectrum was scanned by a copper Kα X-ray source at 40 kV and 40 mA, performed from 20^{o} to 100^{o} in 2-theta mode at a scanning rate of 1.33^{o}/m.

4.4. Experimental Results and Discussions

Weight Loss Method

Effect of temperature

Figure 27 shows the corrosion rates of carbon steel measured by the Weight Loss method after exposure in a supercritical CO_2 environment at (a) 60°C, (b) 80°C, (c) 100°C, and (d) 120°C for 2 days. With all H_2S concentrations (5 ppm, 50 ppm, 100 ppm, and 200 ppm), the trend of the corrosion rates on carbon steel were similar from 60°C, 80°C, 100°C, and 120°C; the corrosion rates reached their maximum at 100°C and then decreased at 120°C with 5 ppm, 50 ppm, and 200 ppm of H_2S gas, except for the corrosion rate with 100 ppm of H_2S which still increased as the temperature rose to 120°C.

Effect of CO_2 pressure

Figure 28 shows the comparison of the corrosion rates on C1018 in the sub-critical CO_2 environment with the ones in the supercritical CO_2 environment at each H_2S concentration; (a)5 ppm, (b)50 ppm, (c)100 ppm, and (d)200 ppm. With 5 ppm of H_2S, the corrosion rates on C1018 in the sub-critical CO_2 environment were higher than the ones in the supercritical CO_2 environment at low temperatures (60°C and 80°C) where the corrosion rates are reversed at higher temperatures (100°C and 120°C), shown in Figure 28 (a). It was suggested that the addition of 5 ppm H_2S helped control the corrosion process in the supercritical CO_2 environment at low temperatures but at higher temperatures the effect of temperature still outweighed the low H_2S concentration as a phase transformation of iron carbonate from iron ion occurred at 95°C.

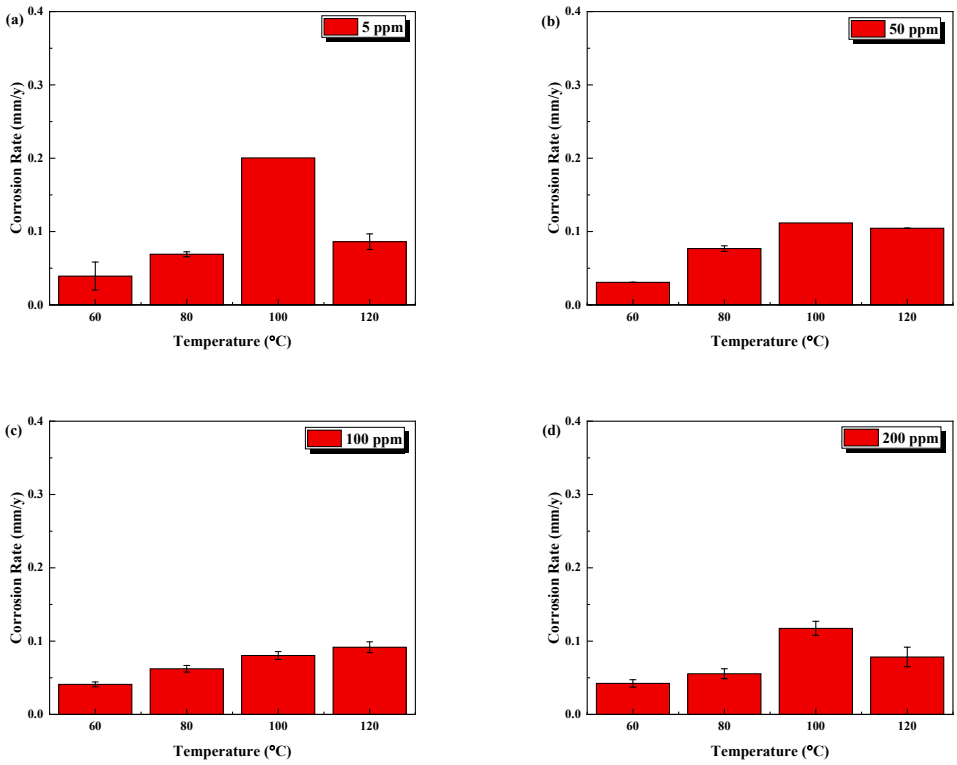

Figure 27: Corrosion rate of carbon steel from Weight Loss method after exposed in the supercritical CO_2 condition at 60°C, 80°C, 100°C, and 120°C with H_2S gas of (a)5 ppm, (b)50 ppm, (c)100 ppm, and (d)200 ppm for 2 days.

Table 12: Statistics of the corrosion rates of C1018 measured by Weight Loss method after exposed to the supercritical CO_2 environment with various H_2S concentrations at elevated temperatures for 2 days.

Corrosion rate of C1018 in supercritical CO_2 environment measured by Weight Loss method				
H_2S concentration(s)	60°C	80°C	100°C	120°C
5 ppm	0.0393 ± 0.0190	0.0691 ± 0.0033	0.2005	0.0861 ± 0.0107
50 ppm	0.0307 ± 0.0002	0.0768 ± 0.0038	0.1117	0.1046 ± 0.0003
100 ppm	0.0413 ± 0.0033	0.0623 ± 0.0045	0.0804 ± 0.0054	0.0917 ± 0.0073
200 ppm	0.0424 ± 0.0050	0.0556 ± 0.0068	0.1174 ± 0.0097	0.0784 ± 0.0133

In Figure 28 (b), the corrosion rates of C1018 in the supercritical CO_2 environment were all lower than the ones in the sub-critical CO_2 environment at all temperatures,

indicating that the H_2S concentration increasing to 50 ppm could be beneficial to the corrosion rate even at higher temperatures. However, with the presence of 100 ppm and 200 ppm of H_2S concentrations, the corrosion rates in the supercritical CO_2 environment were higher than the ones in the sub-critical CO_2 environment at all temperatures. It was assumed that the higher amount of H_2S gas already lost its own protective function on the steel surface due to H_2S corrosion-related issues.

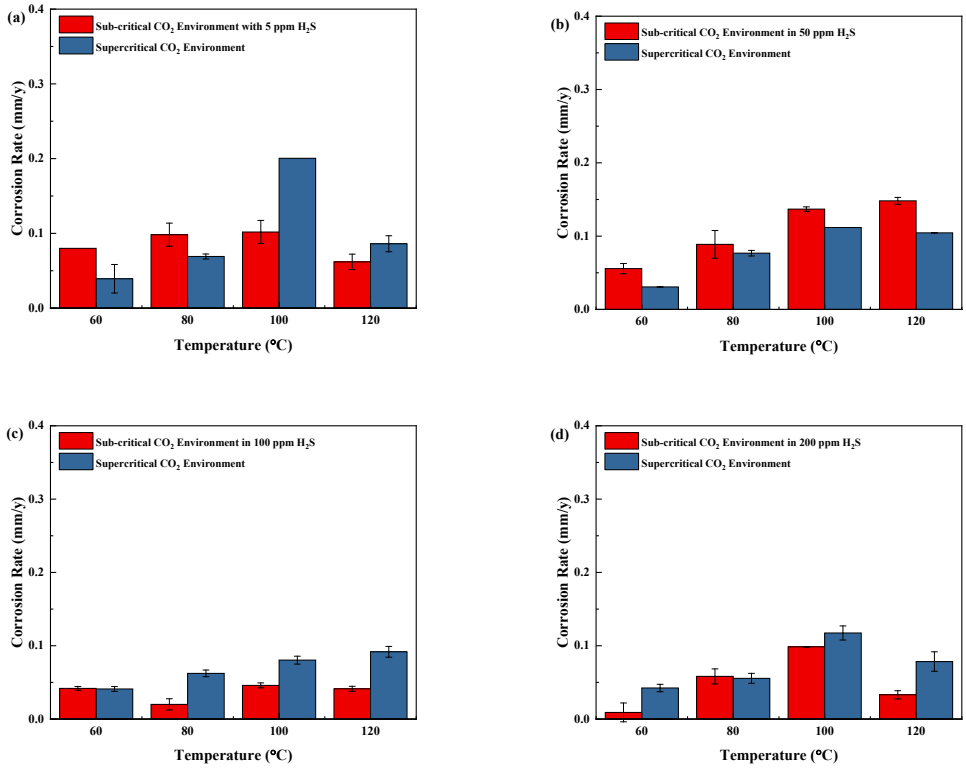

Figure 28: Comparison of the corrosion rates on C1018 from Weight Loss method after exposed in sub-critical and supercritical CO_2 conditions at 60°C, 80°C, 100°C, and 120°C with H_2S gas of (a)5 ppm, (b)50 ppm, (c)100 ppm, and (d)200 ppm for 2 days.

Effect of H_2S concentration

Figure 29 shows the corrosion rate on C1018 with 5 ppm, 50 ppm, 100 ppm, and 200 ppm of H_2S at 60°C, 80°C, 100°C, and 120°C in the supercritical CO_2 environment. At 60°C, the increase in the H_2S concentration did not have a huge effect on the corrosion rate. As the temperature increased to 80°C, the corrosion rate reached its peak with the addition of 50 ppm H_2S but decreased with increasing H_2S concentration. This phenomenon was the same as the trend of the corrosion rate at 120°C. Interestingly, the corrosion rates with all H_2S concentrations at 100°C did not show a trend, meaning they reacted differently compared to the corrosion rates at other temperatures. As the temperature was close to the phase transformation temperature of iron carbonate – 95°C, it was assumed that the corrosion process had not been completed yet after 2 days or due to the synergetic effect of H_2S corrosion combined with CO_2 corrosion.

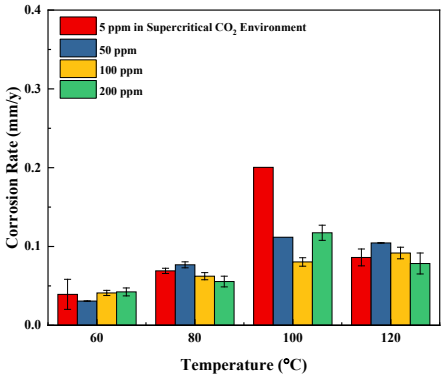

Figure 29: Corrosion rates of C1018 in supercritical CO_2 condition with various H_2S concentrations at elevated temperatures for 2 days.

X-ray Diffraction Spectrum

Figure 30 shows the crystal structure of the C1018 surface exposed in the sub-critical CO_2 environment (a) with addition of 5 ppm H_2S gas at 60°C, 80°C, 100°C, and 120°C, and (b) with the addition of 200 ppm H_2S gas at 60°C and 80°C for 2 days, examined by XRD analysis. In Figure 30 (a), it clearly shows that as the temperature was increasing, a series of phase transformations occurred from 80°C to 120°C. At 60°C and 80°C, the major phase was alpha iron (α-Fe) with a strong peak intensity located at 44.75°, 65.06°, and 82.32° correspondently with the crystal plane (110), (200), and (211), respectively.

Along with the major phase of alpha iron, only a weak peak at 37.61° was identified as part of a common corrosion product that could be easily found in CO_2 corrosion; iron carbonate -$FeCO_3$. This was a different result from the XRD analysis of C1018 in only the CO_2-involved environment at 60°C and 80°C reported in the last chapter. It was clearly seen that iron carbonate promoted to the creation of corrosion products at these two low temperatures, indicating that the water-saturated sub-critical and supercritical CO_2 environments favored the formation of iron carbonate, whereas the water-saturated sub-critical CO_2 environment with 5 ppm H_2S addition did not promote the formation of iron carbonate even with a low dose of H_2S gas concentration.

At 100°C shown on the yellow line, it could be seen that the peaks belonging to alpha iron started decreasing compared to the peaks of alpha iron at 60°C and 80°C. It was assumed that the phase of alpha iron was inhibited due to the increase of the temperature and inhibition of the H_2S addition. Meanwhile, peaks at 32.2°, 42.98°, 49.26°, and 54.54°

appeared and were confirmed as other types of corrosion products related to iron sulfide - mackinawite and troilite [2]. As the temperature was raised to 120°C, a phase transformation of iron sulfide occurred as shown on the blue line. Peaks of troilite at 32.09°, 42.47°, 52.93°, 61.64°, 64.78°, and 65.42° shows strong peak intensity, meaning crystalline troilite took place on the steel surface whereas the peak belonging to mackinawite disappeared. It was deduced that the troilite phase was generated as a film covering the steel surface and iron carbonate. However, the film is not thick enough to cover the entire surface, so part of the iron carbonate is still exposed without iron sulfide covering.

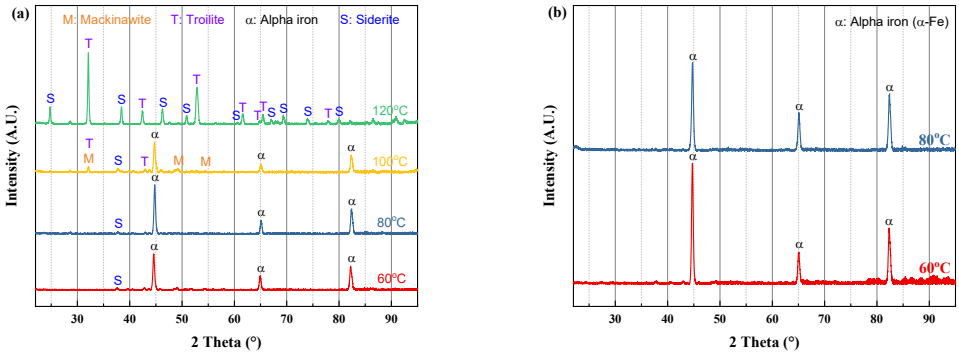

Figure 30: Crystal microstructure of C018 in the sub-critical CO_2 environment (a) with the addition of 5 ppm H_2S at 60°C, 80°C, 100°C, and 120°C, and (b) with the addition of 200 ppm H_2S at 60°C and 80°C.

Scanning Electron Microscopy & Energy Dispersive Spectroscopy

Sub-critical CO_2 environment with different concentration of H_2S addition

Figure 31 shows the surface morphology of C1018 in the sub-critical CO_2 environment at 60°C, 80°C, 100°C, and 120°C with the addition of 5 ppm H_2S for 2 days and examined by SEM. With H_2S gas introduced in the sub-critical CO_2 environment, the formation of the corrosion products would be more complicated than if it was created

merely in an environment containing CO_2 gas because H_2S corrosion was competing with CO_2 corrosion. At 60°C, a layer of corrosion products was created on the steel surface as shown in Figure 31 (a) and (b), and it was assumed to be a layer of sulfur or iron sulfide, which was not identified in the XRD analysis above. The reason why it did not show peaks in the XRD result was because with the small amount of H_2S gas at the low temperature, it would exist as an amorphous phase, so the formation of its crystalline phase was not promoted yet. Also, it was well known that the thin film was so brittle that it was easy to crack due to the inner stress. In Figure 31 (c), the EDS result shows a strong characteristic peak of sulfur.

At 80°C, in addition to a cracked layer of sulfur or iron sulfide found on the steel surface, other corrosion products seemed populated randomly on the surface. From the EDS result shown in Figure 31 (e) for the corrosion products exposed at 80°C, as the sulfur-related film was still compact on the surface, it was not difficult to understand that the peaks belonging to sulfur/iron sulfide were stronger than the peaks of iron. On the other hand, a secondary type of corrosion products were also precipitated on the surface, and it was believed that they were related to iron sulfide.

As the temperature was raised to 100°C, the compact film seemed broken and was detached from the surface. The SEM image shown as Figure 31 (f) was two types of corrosion products that were mixed and hidden underneath the thin film. Given the information that some of the corrosion products were in the cubic/solid shape and combined with the XRD result, it was confirmed that they were siderite - iron carbonate ($FeCO_3$), which is well-known as the corrosion product related to CO_2 corrosion. Siderite

has solid and three-dimensional structure, which was bigger than iron sulfide corrosion products but hidden beneath. Based on this observation, it was deduced that iron carbonate has a preferential crystallization happening prior to the formation of iron sulfide in an CO_2 environment containing H_2S. The other type of corrosion product was assumed to be mackinawite (FeS). This result was also consistent with the XRD result shown above.

At 120°C, the SEM image, shown as Figure 31 (h), presents more iron carbonate that was covered by another type of sulfides on the steel surface. The sulfides, confirmed with the XRD result, were another type of sulfide - troilite. In addition, at this high temperature the iron carbonate was scaled on top of the surface as a thick and compact layer of corrosion products that covered the steel surface, preventing the X-ray from penetrating to the steel surface [2]. That was why the peak of α-Fe was not detected by the X-ray at 120°C.

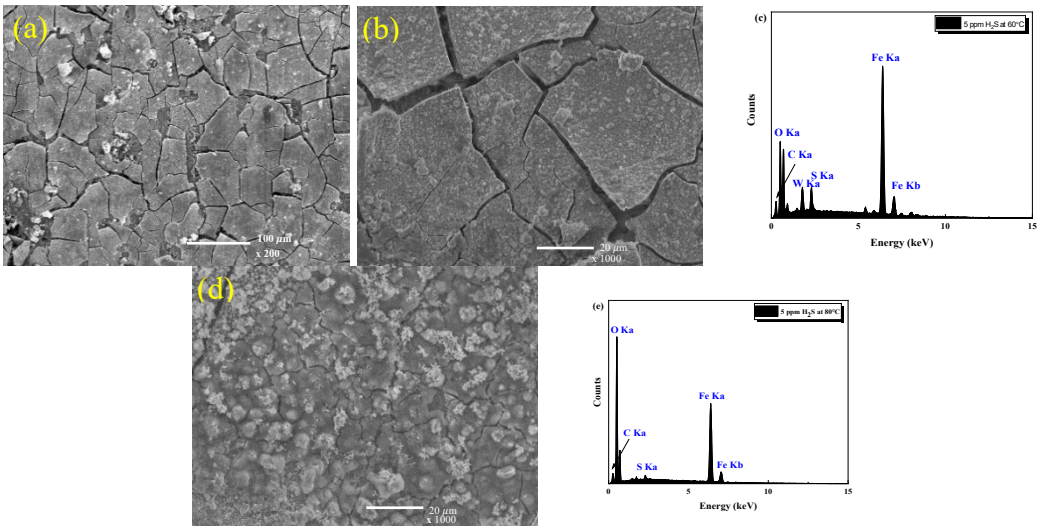

Figure 31: Surface morphology of C1018 in sub-critical CO_2 condition with the addition of 5 ppm H_2S at 60°C, 80°C, 100°C, and 120°C.

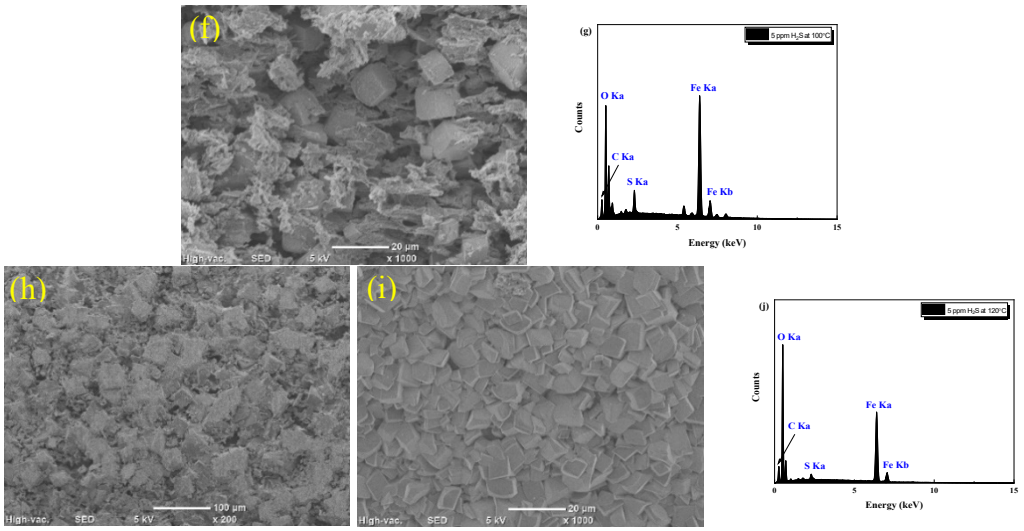

Figure 32 Continued: Surface morphology of C1018 in sub-critical CO_2 condition with the addition of 5 ppm H_2S at 60°C, 80°C, 100°C, and 120°C.

Table 13: EDS result of the corrosion products on C1018 in the sub-critical CO_2 condition at 60°C, 80°C, 100°C, and 120°C with 5 ppm H_2S.

Temperature	Silicon, S (atom %)	Carbon, C	Oxygen, O	Iron, Fe
60°C	-	-	-	-
80°C	0.46	15.35	52.65	31.54
100°C	1.92	26.11	34.6	37.37
120°C	0.45	24.03	49.63	25.9

Figure 32 presents the surface morphology of C1018 in the sub-critical CO_2 environment at 60°C, 80°C, 100°C, and 120°C with the addition of 50 ppm H_2S for 2 days, examined by SEM. In all SEM images (Figure 32 (a), (d), (g), and (i)) representing for 60°C, 80°C, 100°C, and 120°C, respectively, the layer of sulfur/iron sulfide with 50 ppm H_2S became thicker than the one with only 5 ppm of H_2S addition. However, the continuity of the sulfur/iron sulfide layer seemed better at 60°C, 80°C, and 100°C than it was at 120°C. It has to be kept in mind that the testing environment contained not only H_2S gas, but also CO_2 gas. The two different gases would result in generating correspondent corrosion products, and the corrosion products related to H_2S corrosion could be more

diverse like mackinawite, troilite, pyrrhotite, and pyrite owning to elevated temperatures, pH, and concentration of H_2S [2].

At 120°C, the high temperature largely promoted the formation of iron carbonate that further increased the inner stress. Then, it increased the roughness of the surface and broke the sulfur-related layer from the inside. This phenomenon explained why the continuity of the layer at lower temperatures (60°C, 80°C, and 100°C) was better than it was at 120°C even though the thickness of the corrosion layer was greater with 50 ppm H_2S addition than it was with 5 ppm H_2S addition. Furthermore, the exposure of the inner layer – iron carbonate is also one of the reasons that contributed to the increase of the corrosion rate. As a matter of fact, many environmental factors could affect the corrosion rate, so it cannot be explained merely based on the sources of mediums inside the system like CO_2 or H_2S gas. Essentially, pH value, temperature, and pressure also played an important role to explain the kinetics of the entire chemical system.

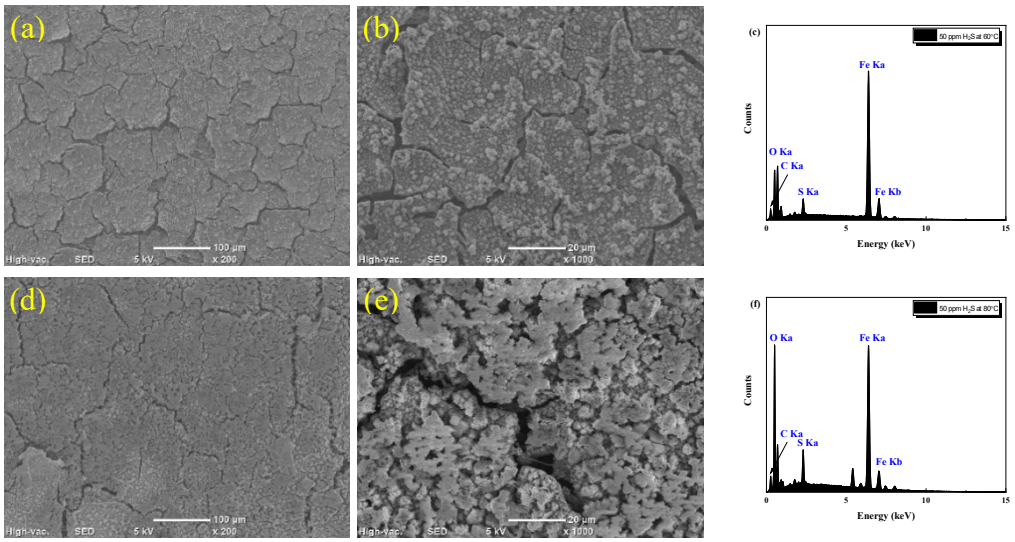

Figure 33: Surface morphology of C1018 in the sub-critical CO_2 condition with the addition of 50 ppm H_2S at 60°C, 80°C, 100°C, and 120°C.

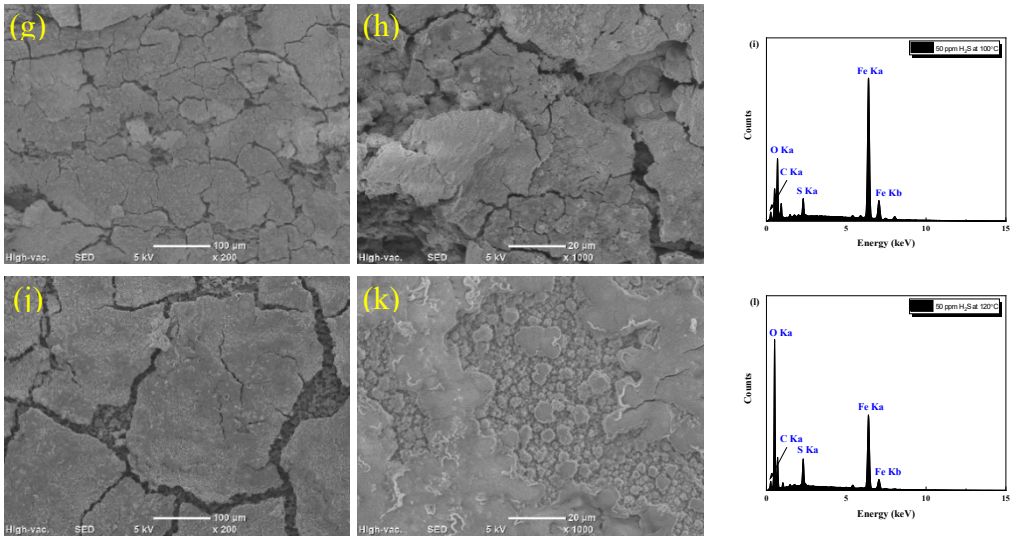

Figure 34 Continued: Surface morphology of C1018 in the sub-critical CO_2 condition with the addition of 50 ppm H_2S at 60°C, 80°C, 100°C, and 120°C.

Table 14: EDS result of the corrosion products on C1018 in the sub-critical CO_2 condition at 60°C, 80°C, 100°C, and 120°C with 50 ppm H_2S.

Temperature	Silicon, S (atom %)	Carbon, C	Oxygen, O	Iron, Fe
60°C	1.93	19.42	18.83	59.82
80°C	2.7	19.28	38.6	39.42
100°C	2.47	12.66	18.05	66.82
120°C	2.94	14.74	52.6	29.05

Figure 33 shows the surface morphology of C1018 in the sub-critical CO_2 environment at 60°C, 80°C, 100°C, and 120°C with the addition of 100 ppm H_2S for 2 days, examined by SEM. As the H_2S concentration was increased to 100 ppm, the layer of sulfur/iron sulfide seemed to become thicker and denser at 60°C compared to it with 50 ppm H_2S addition at the same temperature. In addition, at 60°C (Figure 33 (b)) and 80°C (Figure 33 (d)), some needle or flat sheet-like corrosion products were found on the steel surface. These corrosion products were identified as another type of iron sulfide - FeS_2 by Alpermann through his research conducted in a supercritical CO_2 condition with a mixture of 10% H_2S in an initial dry condition [43]. However, he did not clearly specify whether

they were marcasite nor pyrite. At 120°C (Figure 33 (i)), some corrosion products with solid shapes covered by iron sulfide were also found on the steel surface, which was the same as in the sub-critical CO_2 environment with 5 ppm of H_2S addition at 120°C.

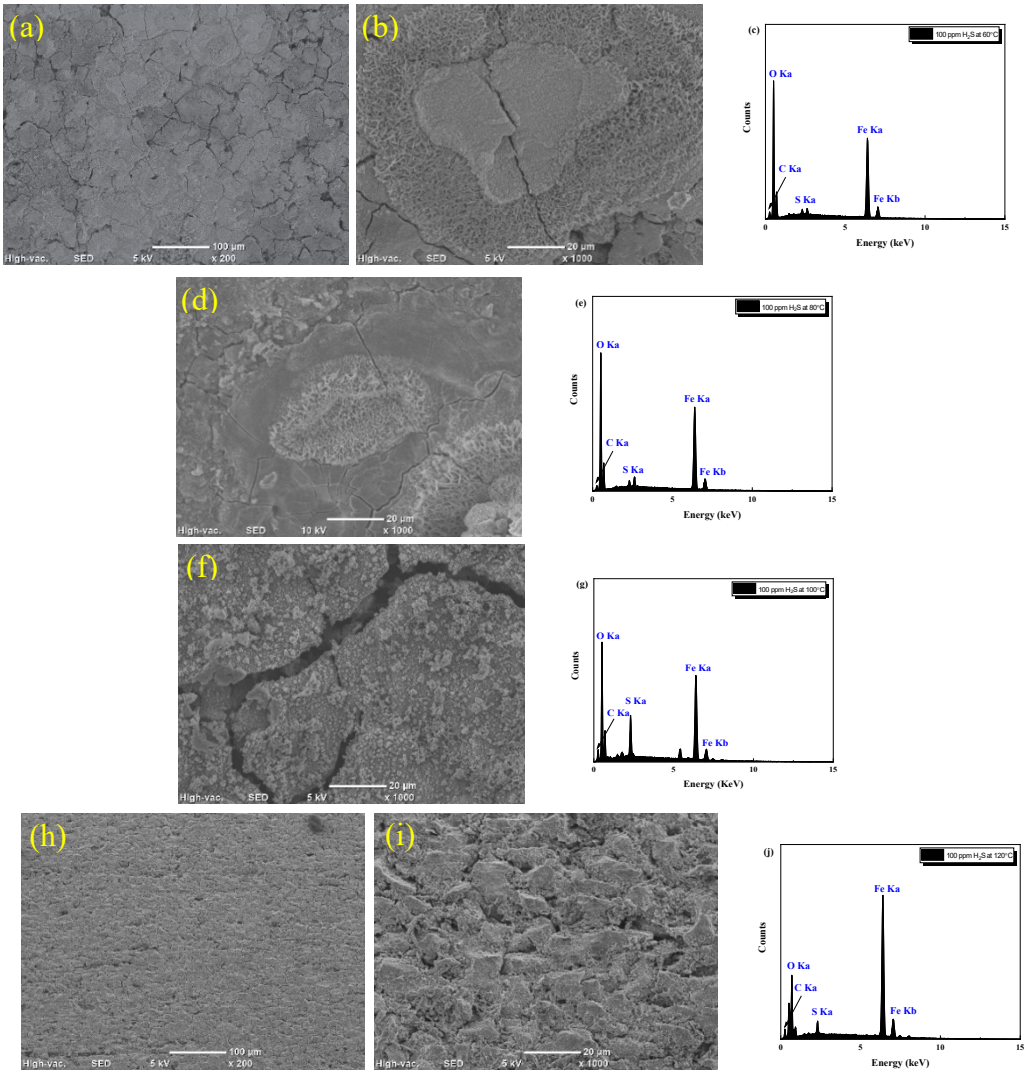

Figure 35: Surface morphology of C1018 in the sub-critical CO_2 condition with the addition of 100 ppm H_2S at 60°C, 80°C, 100°C, and 120°C.

Table 15: EDS result of the corrosion products on C1018 in the sub-critical CO_2 condition at 60°C, 80°C, 100°C, and 120°C with 100 ppm H_2S.

Temperature	Silicon, S (atom %)	Carbon, C	Oxygen, O	Iron, Fe
60°C	0.22	8.97	52.22	38.58
80°C	0.81	7.27	53.37	38.55
100°C	4.27	20.74	43.58	31.41
120°C	1.75	19.03	14.09	65.03

Figure 34 shows the surface morphology of C1018 in the sub-critical CO_2 environment at 60°C, 80°C, 100°C, and 120°C with the addition of 200 ppm H_2S for 2 days, examined by SEM. It could be seen that the layer of corrosion products was thicker, denser, and more compact with 200 ppm of H_2S addition at 60°C and 80°C in comparison with the one with lower concentrations of H_2S. It seems that the higher the H_2S concentration, the thicker the layer of the corrosion products. At higher temperatures like 100°C and 120°C, iron carbonate seemed to become more populated compared to the lower temperatures. However, it should be noted that the iron carbonate corrosion products were also formed at lower temperatures like 60°C and 80°C as indicated in the XRD analysis. The reason why it was not shown in the SEM imagines was because iron sulfide precipitated later and covered over it.

On the other hand, flaky sheet-like corrosion products were also observed on the steel surface, and it was identified as pyrrhotite by Gao and his co-workers [2] with the simulation of Pourbaix diagrams of H_2S at 120°C as thermodynamic model. As mentioned before, the pH value drifted from pH 5.6 to pH 5.9, depending on the temperature. This pH range favored the formation of pyrrhotite.

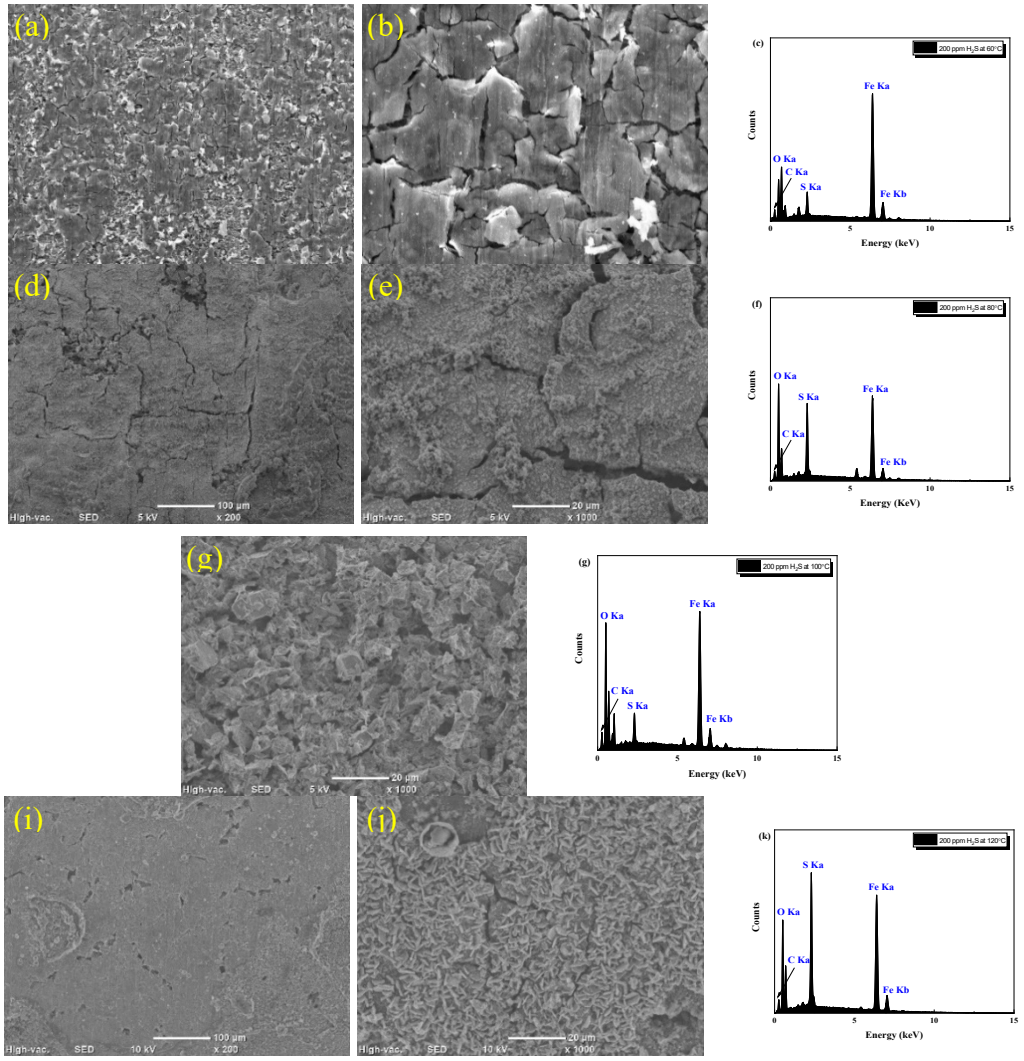

Figure 36: Surface morphology of C1018 in the sub-critical CO_2 condition with the addition of 200 ppm H_2S at 60°C, 80°C, 100°C, and 120°C.

Table 16: EDS result of the corrosion products on C1018 in the sub-critical CO_2 condition at 60°C, 80°C, 100°C, and 120°C with 200 ppm H_2S.

Temperature	Silicon, S (atom %)	Carbon, C	Oxygen, O	Iron, Fe
60°C	0.22	8.97	52.22	38.58
80°C	0.81	7.27	53.37	38.55
100°C	4.27	20.74	43.58	31.41
120°C	1.75	19.03	14.09	65.03

Supercritical CO_2 environment with different concentration of H_2S addition

Figure 35 shows the surface morphology of C1018 in the supercritical CO_2 environment at 60°C, 80°C, 100°C, and 120°C with the addition of 5 ppm H_2S for 2 days, examined by SEM. In the supercritical CO_2 environment with 5 ppm of H_2S addition, similar surface morphology was observed as it was in sub-critical CO_2 environment with the same amount of H_2S concentration; a thick layer of corrosion products was covered on the steel surface, and some areas were found with a bundle of flat sheet-like corrosion products, FeS_2, which were the same corrosion products observed in the sub-critical CO_2 environment at 60°C and 80°C with 100 ppm of H_2S addition. As the temperature was increased to 100°C and 120°C, it was easier to find iron carbonate exposed on the surface without a thin layer of iron sulfide.

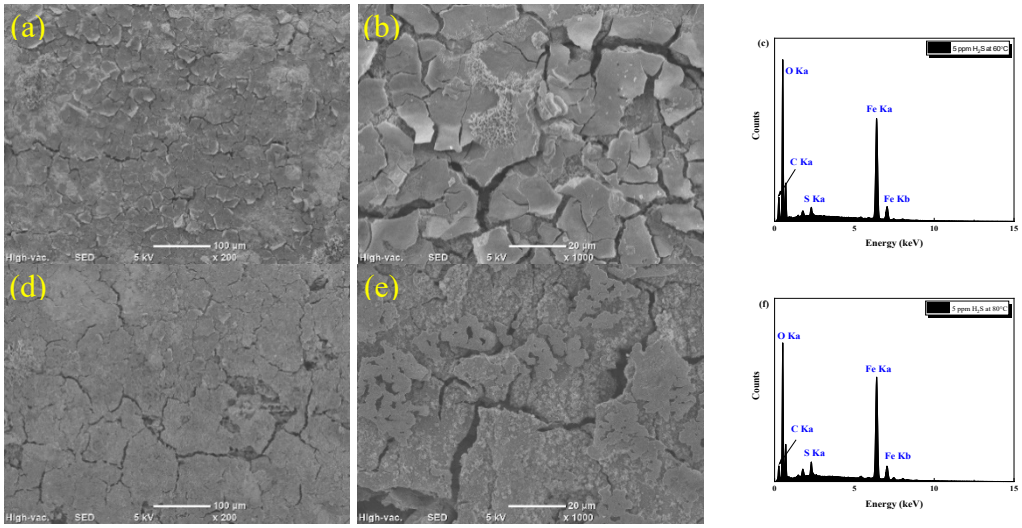

Figure 37: Surface morphology of C1018 in the supercritical CO_2 condition with the addition of 5 ppm H_2S at 60°C, 80°C, 100°C, and 120°C.

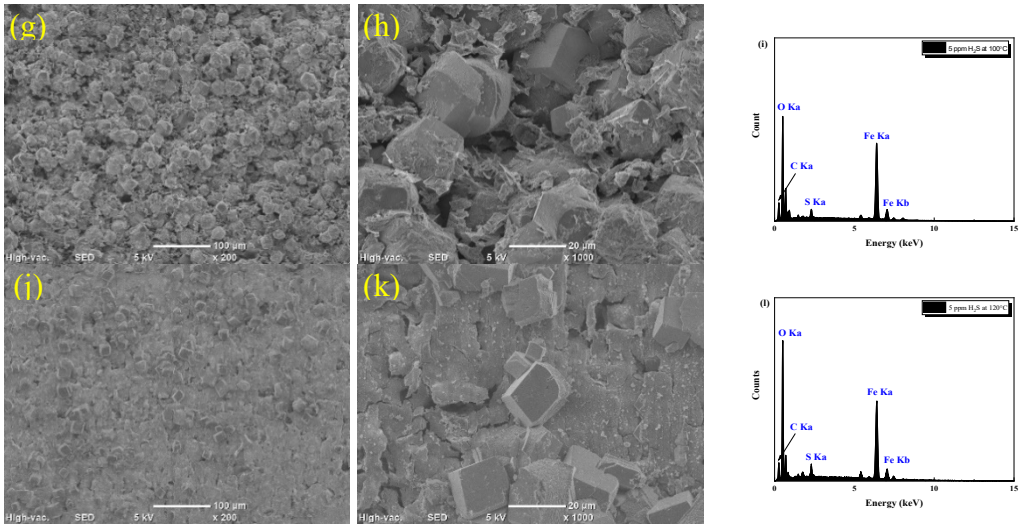

Figure 38 Continued: Surface morphology of C1018 in the supercritical CO_2 condition with the addition of 5 ppm H_2S at 60°C, 80°C, 100°C, and 120°C.

Table 17: EDS result of the corrosion products on C1018 in the supercritical CO_2 condition at 60°C, 80°C, 100°C, and 120°C with 5 ppm H_2S.

Temperature	Silicon, S (atom %)	Carbon, C	Oxygen, O	Iron, Fe
60°C	0.57	27.2	44.28	27.95
80°C	1.17	21.2	43.58	34.04
100°C	0.92	28.53	40.7	29.84
120°C	1.02	24.75	48.05	26.18

Figure 36 shows the surface morphology of C1018 in the supercritical CO_2 environment at 60°C, 80°C, 100°C, and 120°C with the addition of 50 ppm H_2S for 2 days, examined by SEM. The surface morphology obtained in the supercritical CO_2 environment with 50 ppm H_2S at all temperatures was similar to what it was in the sub-critical CO_2 environment with the same amount of H_2S addition. At 60°C, 80°C, and 100°C, the steel surface was covered with a layer of iron sulfide, and the continuity of the iron sulfide layer was more coherent than it was at 120°C where the steel surface had a higher roughness with more iron carbonate exposed on the surface. It suggested that more iron carbonate

was nucleated and grew already in 2 days. More iron carbonate was created, resulting in a highly porous surface.

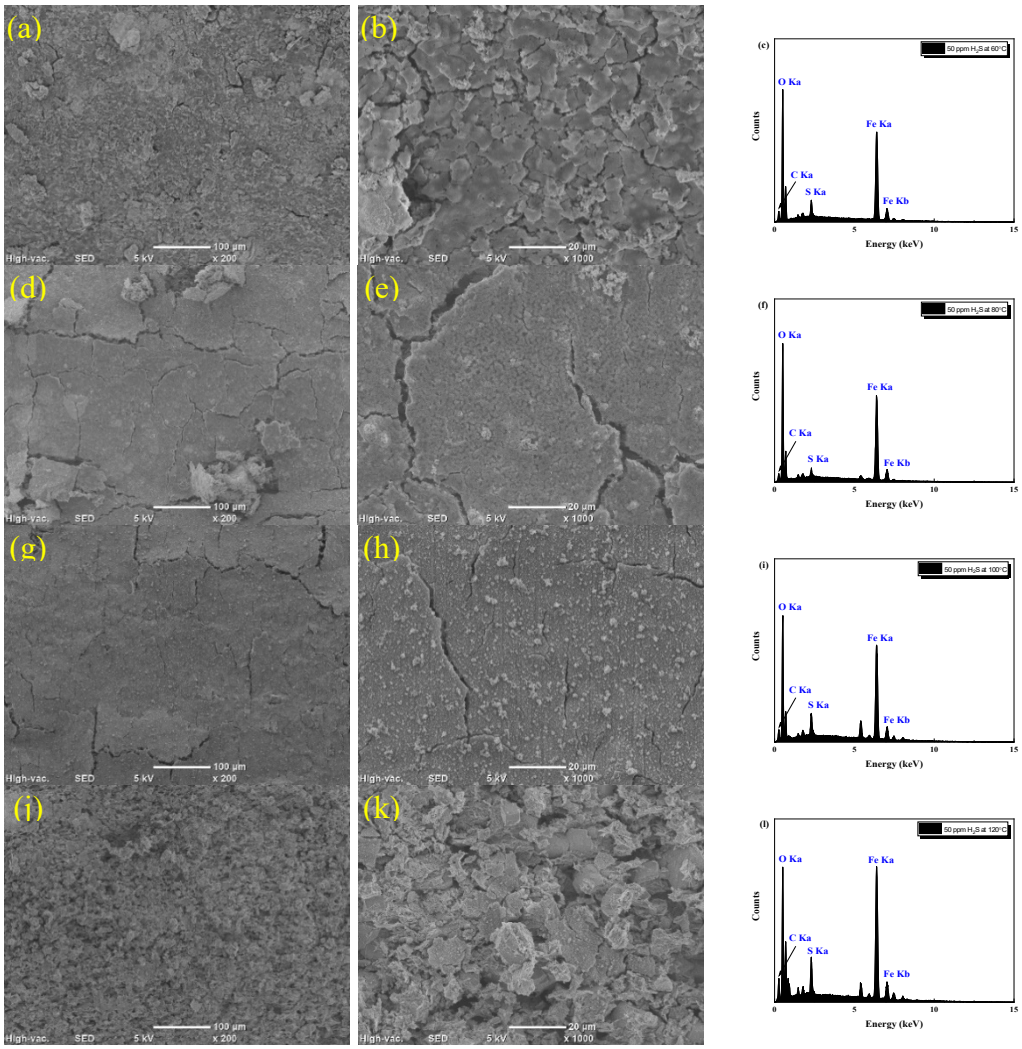

Figure 39: Surface morphology of C1018 in the supercritical CO_2 condition with the addition of 50 ppm H_2S at 60°C, 80°C, 100°C, and 120°C.

Table 18: EDS result of the corrosion products on C1018 in the supercritical CO_2 condition at 60°C, 80°C, 100°C, and 120°C with 50 ppm H_2S.

Temperature	Silicon, S (atom %)	Carbon, C	Oxygen, O	Iron, Fe
60°C	1.71	16.46	46.8	35.03
80°C	0.83	13.02	50.47	35.68
100°C	2.08	18.39	41.22	34.63
120°C	2.62	26.15	33.38	35.51

Figure 37 shows the surface morphology of C1018 in the supercritical CO_2 environment at 60°C, 80°C, 100°C, and 120°C with the addition of 100 ppm H_2S for 2 days, examined by SEM. With this amount of H_2S concentration, the corrosion products seemed thicker than the ones with lower doses of H_2S concentration. Meanwhile, at all temperatures, more troilite (FeS_2) was observed (not shown) as corrosion products with this amount of H_2S dose compared to the created corrosion products with a lower dose of H_2S concentration in the supercritical CO_2 environment. It suggests a quicker phase transformation from mackinawite to troilite occurred at 1600 psi over that at 400 psi. Interestingly, the layer of the iron sulfide at 120°C still remained intact. It was assumed that the effect of the high pressure and of the higher concentration of H_2S promoted the stability of the iron sulfide layer over the formation of iron carbonate.

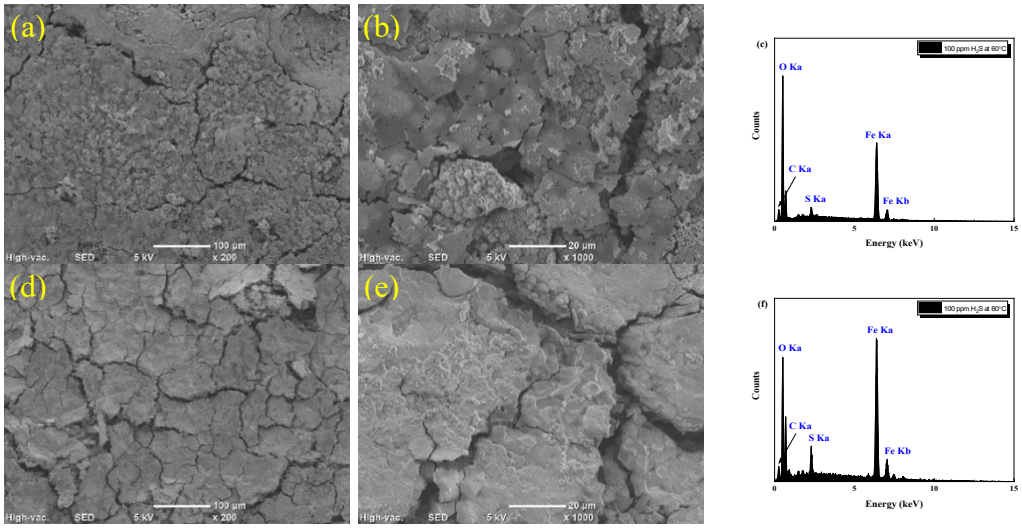

Figure 40: Surface morphology of C1018 in the supercritical CO_2 condition with the addition of 100 ppm H_2S at 60°C, 80°C, 100°C, and 120°C.

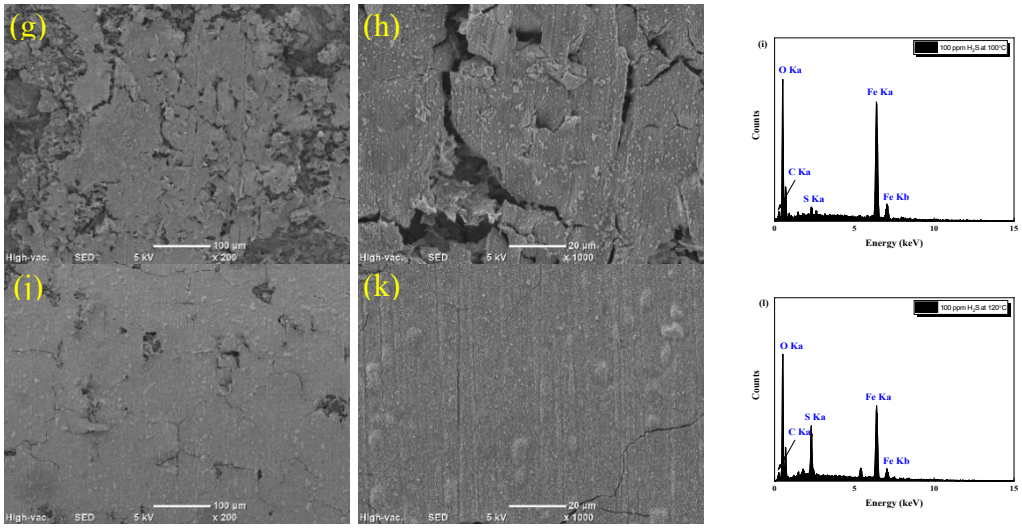

Figure 41 Continued: Surface morphology of C1018 in the supercritical CO_2 condition with the addition of 100 ppm H_2S at 60°C, 80°C, 100°C, and 120°C.

Table 19: EDS result of the corrosion products on C1018 in the supercritical CO_2 condition at 60°C, 80°C, 100°C, and 120°C with 100 ppm H_2S.

Temperature	Silicon, S (atom %)	Carbon, C	Oxygen, O	Iron, Fe
60°C	0.94	19.12	50.12	29.82
80°C	2.17	19.32	36.03	42.47
100°C	0.89	12.75	43.03	43.33
120°C	5.28	15.61	50.14	28.97

Figure 38 shows the surface morphology of C1018 in the supercritical CO_2 environment at 60°C, 80°C, 100°C, and 120°C with addition of 200 ppm H_2S for 2 days, examined by SEM. At all temperatures, the steel surface was covered by a thick layer of corrosion products which was comprised of flaky sheet-like corrosion products, troilite. In addition, big solid crystals were found underneath the layer of the corrosion products at higher temperatures where some of the corrosion layers were broken. Given the SEM images from 60°C to 120°C, from the sub-critical CO_2 environment to the supercritical CO_2 environment, and from 5 ppm of H_2S to 200 H_2S ppm, a series of phase

transformations of H_2S-related corrosion products was observed. Therefore, it is possible that the corrosion mechanism of C1018 in a CO_2-contained environment with low concentration of H_2S could explain the experimental results observed above. Firstly, the corrosion products transferred from mackinawite through troilite to pyrrhotite as the temperature rose, and the growth rate of the corrosion products speeded up under the effect of temperature. Secondly, the dose of H_2S concentration correlated with the stability and thickness of the iron sulfide layer. Thirdly, the effect of pressure impacted the integrity of the corrosion product layer as the formation of iron carbonate was also ongoing underneath. As mentioned above, the iron sulfide layer was so brittle that it would be easy to be broken apart if the inner stress was increased beyond the tolerance of its hardness, and vice versa. Like the corrosion layer formed at 120°C in supercritical CO_2 environment with 100 ppm of H_2S addition, a subtle relationship between pressure, temperature, and H_2S concentration was reached in balance, so the corrosion layer was retained relatively intact compared to the corrosion layers at the other temperatures with different amounts of H_2S dose.

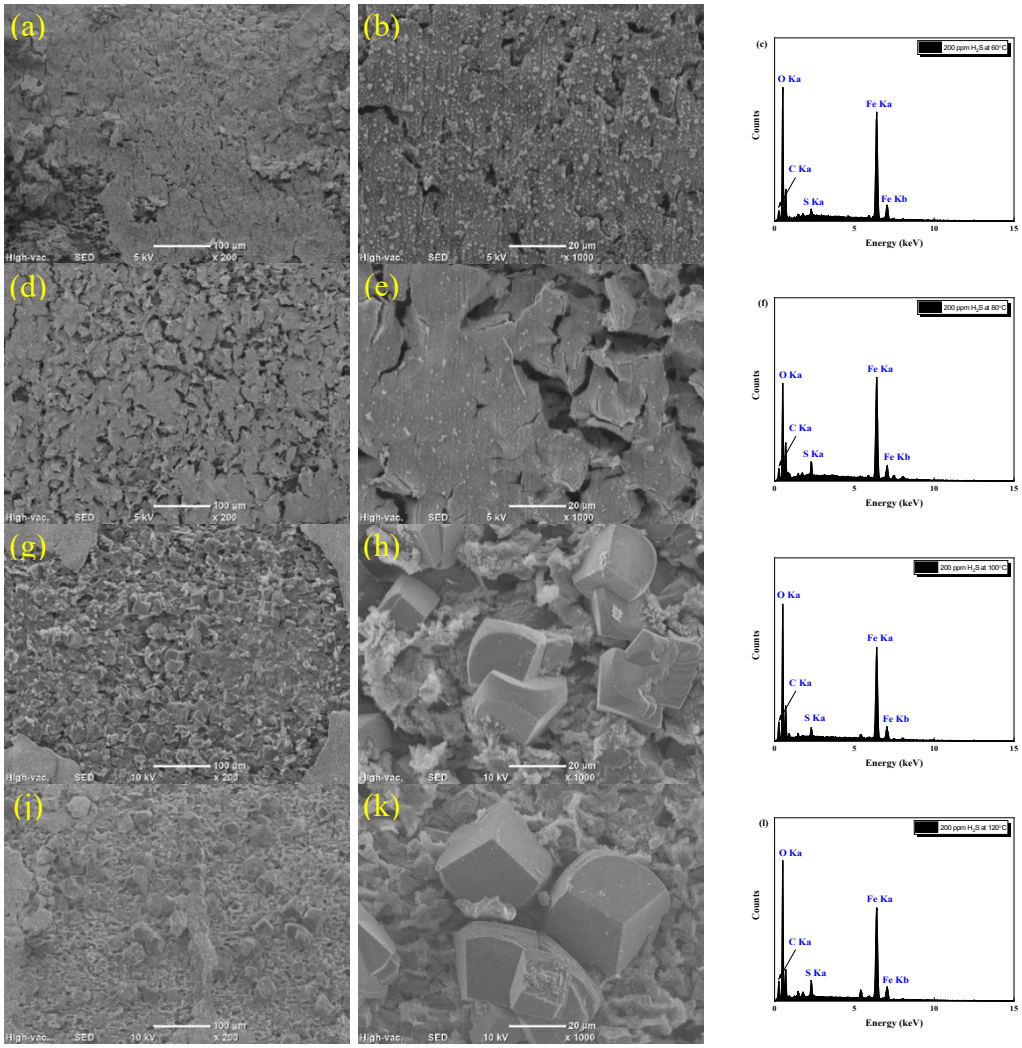

Figure 42: Surface morphology of C1018 in the supercritical CO_2 condition with the addition of 200 ppm H_2S at 60°C, 80°C, 100°C, and 120°C.

Table 20: EDS result of the corrosion products on C1018 in the supercritical CO_2 condition at 60°C, 80°C, 100°C, and 120°C with 200 ppm H_2S.

Temperature	Silicon, S (atom %)	Carbon, C	Oxygen, O	Iron, Fe
60°C	0.68	15.99	44.53	38.79
80°C	1.67	21.9	37.05	39.39
100°C	0.86	25.29	44.21	29.64
120°C	1.49	25.13	43.83	29.55

Linear Polarization Resistance Method

Figure 39 presents statistics of the LPR results for C1018 exposed to the sub-critical CO_2 environment at 60ºC, 80ºC, 100ºC, and 120ºC with various H_2S concentrations, which shows final corrosion rates and final corrosion potential after 2 days of testing. In the sub-critical CO_2 environment with all H_2S concentrations, Figure 39 (a) shows an increase in the final corrosion rate when temperature was raised to 100ºC. Theoretically, the higher the temperature is, the higher the corrosion rate is observed. However, a lower corrosion rate was obtained at 120ºC, instead. It was assumed that after 2 days of testing, the corrosion process was already complete or reached a dynamic balance between the dissolution of irons to the solution and the formation of iron carbonate precipitated on the steel surface. Either cause could be explained by the tendency of the final corrosion potential of C1018 at all temperatures with various H_2S concentrations, which are shown in Figure 39 (b). The figure shows an increase in the final corrosion potential as the temperature went up to 120ºC from 60ºC for all H_2S concentrations; at 120ºC, the final corrosion potential reached the highest value among the four temperatures for all the four H_2S concentrations, indicating that regardless of H_2S concentration the system became more noble at 120ºC compared to the ones at lower temperatures.

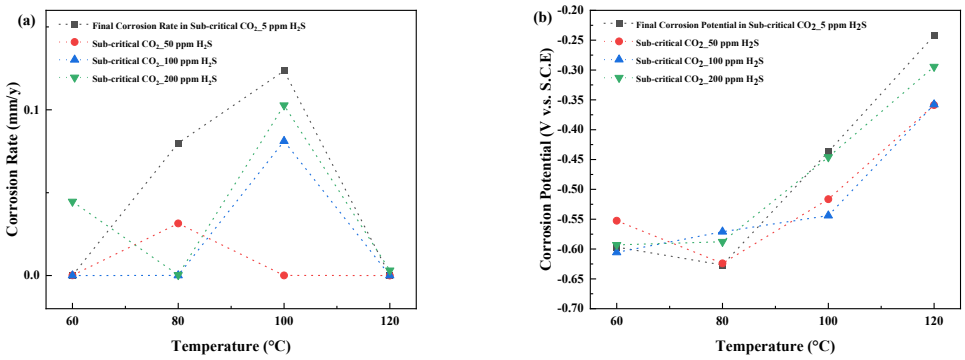

Figure 43: (a)Final corrosion rate and (b)final corrosion potential of C1018 exposed to the sub-critical CO_2 condition with various H_2S concentrations at different temperatures after 2 days.

Figure 40 presented statistics of the LPR results of C1018 exposed to the supercritical CO_2 environment at 60°C, 80°C, 100°C, and 120°C with various H_2S concentrations, which shows final corrosion rates and final corrosion potentials after 2 days of testing. The result shows that the variations for the final corrosion rates of C1018 as temperature went up became smaller in the supercritical CO_2 environment compared to the ones in the sub-critical CO_2 environment (Figure 39). Also, lower final corrosion rates were observed at 120°C, which was the same for the sub-critical CO_2 environment. It was assumed that the corrosion process at 120°C in the supercritical CO_2 environment after 2 days also reached a dynamic balance.

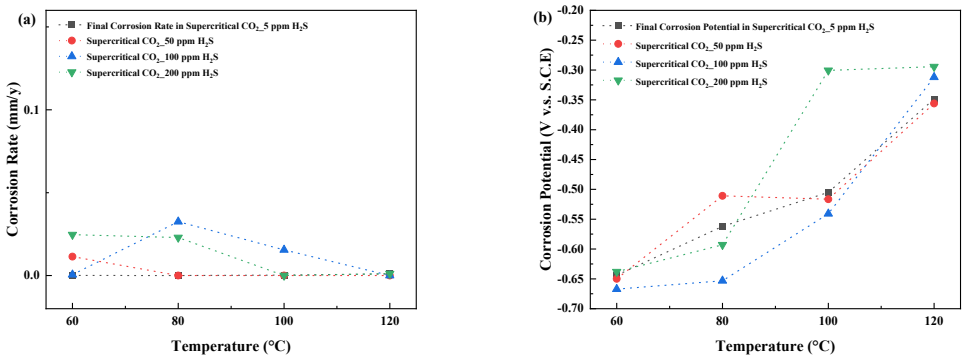

Figure 44: (a)Final corrosion rate and (b)final corrosion potential of C1018 exposed to the supercritical CO_2 condition with various H_2S concentrations at different temperatures after 2 days.

Table 21: Statistics of final corrosion rates on C1018 from LPR in the sub-critical and supercritical CO_2 conditions with various H_2S concentrations at different temperatures.

	Sub-critical CO_2 condition				Supercritical CO_2 condition			
	5 ppm	50 ppm	100 ppm	200 ppm	5 ppm	50 ppm	100 ppm	200 ppm
60°C	0.002	0.004	0.001	1.759	0.002	0.754	0.02	0.971
80°C	3.149	1.239	0.002	0.014	0.001	0.0001	1.281	0.904
100°C	4.863	0.003	3.194	4.048	0.007	0.001	0.61	0.0002
120°C	0.004	0.001	0.001	0.123	0.042	0.001	0.001	0.048

Table 22: Statistics of final corrosion potential on C1018 from LPR in sub-critical and supercritical CO_2 conditions with various H_2S concentrations at different temperatures.

	Sub-critical CO_2 condition				Supercritical CO_2 condition			
	5 ppm	50 ppm	100 ppm	200 ppm	5 ppm	50 ppm	100 ppm	200 ppm
60°C	-0.597	-0.553	-0.606	-0.593	-0.644	-0.650	-0.667	-0.638
80°C	-0.627	-0.624	-0.571	-0.588	-0.562	-0.511	-0.653	-0.593
100°C	-0.437	-0.517	-0.544	-0.446	-0.505	-0.517	-0.541	-0.301
120°C	-0.242	-0.359	-0.358	-0.294	-0.349	-0.356	-0.312	-0.294

Electrochemical Impendence Spectroscopy Method

The EIS testing was performed at 60ºC, 80ºC, 100ºC, and 120ºC in both sub-critical (400 psi) and supercritical CO_2 (1600 psi) environments with H_2S additions of 5 ppm, 50 ppm, 100 ppm, and 200 ppm. With H_2S gas introduced in both the sub-critical and supercritical CO_2 environments (shown later), the thermodynamics and kinetics in the systems became more complicated to be interpreted than the ones without H_2S gas. As a matter of fact, under the effect of H_2S gas, a series of electrochemical reactions related to H_2S gas took place during the testing. To understand the corrosion behavior on C1018 in both more thoroughly, the Nyquist plots were classified into three stages: initial stage (0-5 hours), middle stage (5 hours - 25 hours), and final stage (25 hours – 40 hours).

Effect of time

Figure 41 presents the Nyquist plots from the EIS testing of C1018 exposed to a sub-critical CO_2 environment at 60ºC, 80ºC, 100ºC, and 120ºC with (a)-(d) 5 ppm and (e)-(h) 50 ppm of H_2S addition. At all temperatures with 5 ppm and 50 ppm of H_2S, shown in Figure 41 (a)-(h), all Nyquist results show compressed single or double capacitor semicircles in the complex impendence plane; one capacitor semicircle is at high frequency, and the other one is at low frequency. The one at high frequency was correlated to the double layer capacitance and charge transfer resistance while the one at low frequency reflected the corrosion product film on the steel surface. As reported in many papers [1, 3, 44], the compressed characterization resulted from high roughness of the surface, which was a typical case for solid metal electrodes shown in the frequency distribution of the impedance spectrum.

At 60°C, with 5 ppm (Figure 41 (a)) and 50 ppm of H_2S addition (Figure 41 (d)), both the size of the two semicircles at high frequency and at low frequency shrank in terms of the diameter and altitude as the time elapsed, indicating the corrosion rates on the corrosion product film and the steel surface were constantly increasing with the prolongation of exposure time at low temperature. As the temperature rose to 80°C (Figure 41 (b)), the size of the capacitor semicircle at high frequency also shrank, and the amplitude of the decrease was larger than the one at 60°C, depicting the corrosion rate on the steel surface at 80°C. Moreover, the position of the starting point of the first capacitor semicircle shifted from low resistance to high resistance, showing that the solution resistance was increasing. At this point, it was believed that more iron ion dissolved into the NaCl solution, meaning the solution contained a higher iron concentration. However, the size of the capacitor semicircle at low frequency was increasing, and the formation of the corrosion product film could explain this observation.

When the temperature was increased to 100°C and 120°C with 5 ppm of H_2S addition (Figure 41 (c-d)), the capacitor resistance at low frequency enlarged tremendously at the 25th hour and 40th hour, showing the corrosion product film possessed high corrosion resistance. It was deduced that the formation of the corrosion product film on the steel surface was accomplished at the 25th hour. It served as a protective layer on top of the steel surface, so the system became more inactive at 100°C and 120°C compared to the ones at the same timing at 60°C and 80°C. At 120°C, chemical reactions in the system even reached equilibrium earlier, which was proven by the EIS result at 5th hour

(the red line in Figure 41 (d)), showing the system behaved more vigorously compared to 100ºC because the system reached high corrosion resistance in a such short time.

Time is a function of the corrosion rate for sure, but the corrosion rate is not always constant as time progresses. The corrosion rate of material can be determined by outside environmental factors like temperature, pressure, types of media in contact as well as by its own material nature, formed corrosion products on surface, surface morphology, and types of corrosion products. The EIS result at 80ºC with 5 ppm of H_2S addition, shown in Figure 41 (b), is a good example to reflect the transition of corrosion rate. When the testing started, two capacitor semicircles were observed. Sulfur/iron sulfide was already formed on the steel surface. As mentioned above, one at high frequency represents the capacitance of a double layer, and the other one at low frequency depicts a resistance of double layer and a charge transfer resistance. When the time progressed, the capacitor semicircle at high frequency continuously shrank, indicating the steel surface remained active and corroding, which resulted in an increase in the corrosion rate during the whole period. However, the size of the capacitor semicircle at low frequency shrank at the 5^{th} hour but enlarged at the 25^{th} hour and the 40^{th} hour. It was assumed that the corrosion product film was active for the first few hours and then became inactive as the time progressed. In response, the corrosion rate of the corrosion product film increased in the initial period but decreased afterwards. Ruling out the possibility of iron carbonate precipitation, which was proven by the XRD and SEM results, it was deduced that the sulfur/iron sulfide corrosion product film continuously formed for the first 5 hours. However, since the amount of H_2S addition was only 5 ppm, the corrosion product formed little as a thin film,

so it either covered the steel surface as a thin layer or just incompletely covered on the surface. As the time elapsed to 25th hour, the formation of sulfur was close to finishing, so its corrosion rate decreased. The steel surface, on the other hand, remained active and resulted in a high corrosion rate as the testing continued to the end.

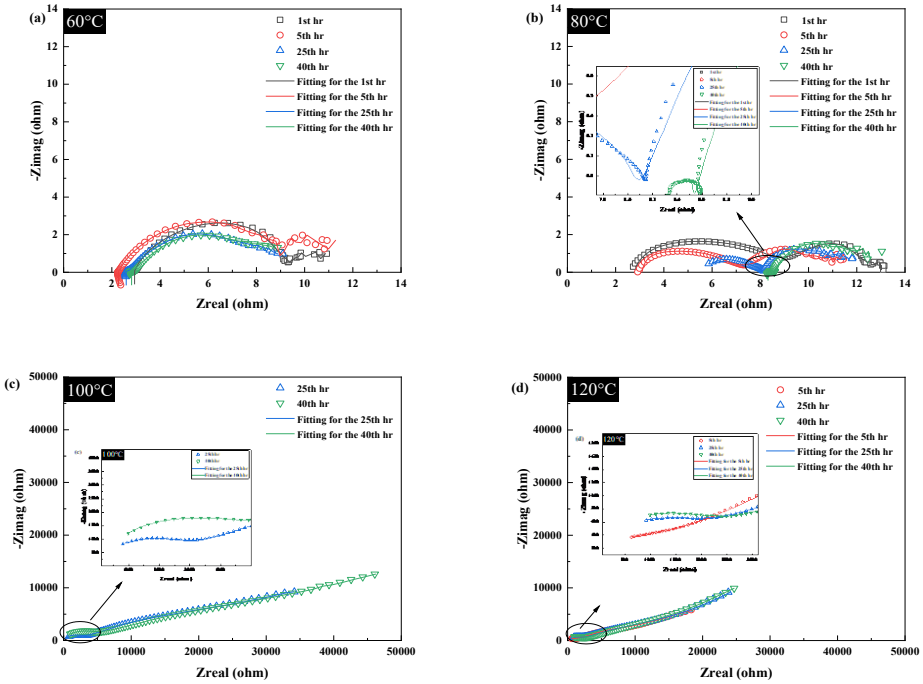

Figure 45: Corrosion behavior of the corrosion products in the sub-critical CO_2 environment at 60°C, 80°C, 100°C, and 120°C with (a)-(d)5 ppm and (e)-(h)50 ppm of H_2S additions.

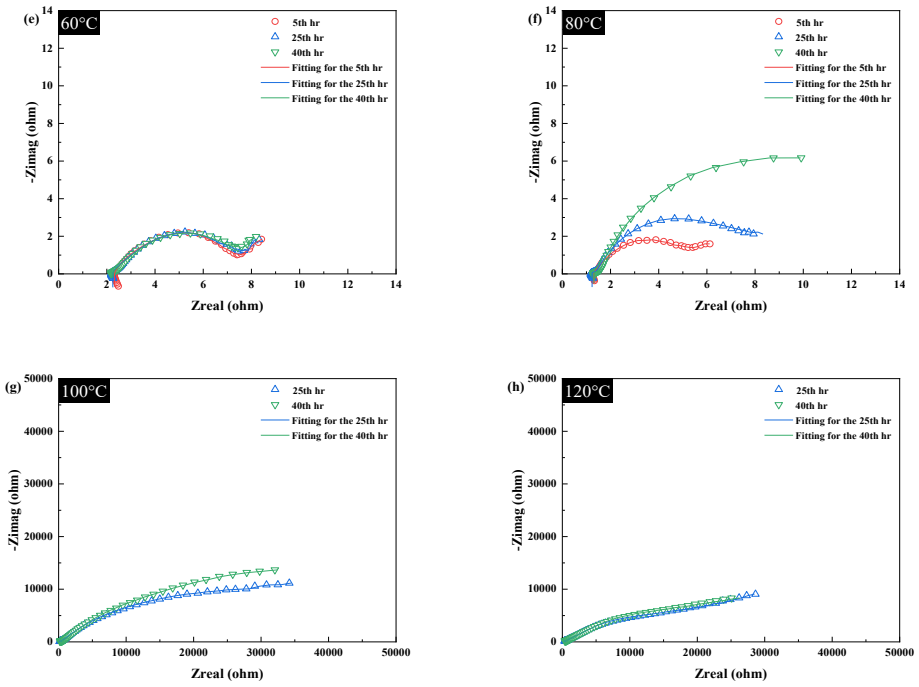

Figure 46 Continued: Corrosion behavior of the corrosion products in the sub-critical CO_2 environment at 60°C, 80°C, 100°C, and 120°C with (a)-(d)5 ppm and (e)-(h)50 ppm of H_2S additions.

Equivalent circuit:

To understand the electrochemical reactions for the system quantitatively, an equivalent circuit, shown in Figure 42, was constructed to compute the electric parameters of each medium, where $\boldsymbol{R_s}$ is solution resistance, $\boldsymbol{Q_f}$ is a constant phase element which represents the capacitance of the corrosion product film, $\boldsymbol{R_f}$ is resistance of the corrosion product film, $\boldsymbol{Q_{dl}}$ is defined as a constant phase element representing the double-charge layer capacitance, and $\boldsymbol{R_{ct}}$ is charge transfer resistance. Values of each electric parameter from 60°C to 120°C in a sub-critical CO_2 environment with 5 ppm and 50 ppm of H_2S additions at different times were output by using this equivalent circuit and listed in Table 23. The data shows that in the sub-critical CO_2 environment with both H_2S concentrations

at 80°C and below the charge transfer resistance, $\boldsymbol{R_{ct}}$, was relatively higher compared to the resistance of the corrosion product film, $\boldsymbol{R_f}$, and the resistance of the corrosion product film was decreasing with the duration of the exposure time while the charge transfer resistance increased at first and then decreased as time elapsed.

This phenomenon can be understood by a phase transition of sulfur to iron sulfide on top of the surface. In the initial period, which would vary from the 1st hour to the 5th hour, or from the 1st hour to longer, depending on the interaction and the dynamic balance between temperature, pressure, and H_2S concentration, the corrosion product film at low temperatures (60°C and 80°C) was mainly composed of two products – sulfur and iron sulfide. It is not a secret that sulfur is a non-metallic material, which was not considered as a conductor whereas iron sulfide is electronically conductive [1]. In the initial period, sulfur ion (S^{2-}) was adsorbed onto the surface and was precipitated from sulfur ion to element sulfur (S). As time elapsed, a layer consisting of sulfur gradually built up, which led to the increase in the charge transfer resistance. Meanwhile, part of the inner sulfur ion in contact with the steel surface was converted to iron sulfide with the reduction of iron ion, which caused the resistance of the corrosion product to decrease. Hence, the effect of time on the phase transition from sulfur ion, through sulfur, to iron sulfide was the main reason for the variation of the resistance of the corrosion product and of the charge transfer resistance.

Reduction of H_2S:

$$\boldsymbol{H_2S + 2e^- \rightarrow HS^- + H_2} \quad \textbf{(28)}$$

$$\boldsymbol{2HS^- + 2e^- \rightarrow 2S^{2-} + H_2} \quad \textbf{(29)}$$

For sub-critical and supercritical CO_2 condition with various H_2S

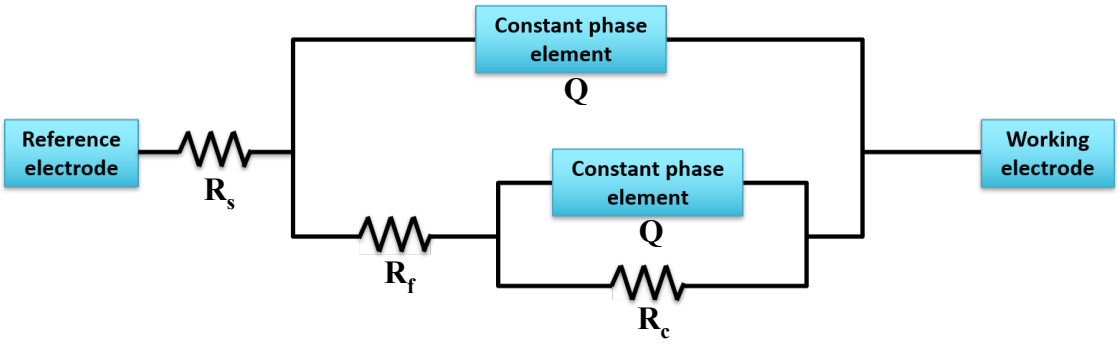

Figure 47: Equivalent circuit constructed to simulate the electrochemical properties of each parameter in the sub-critical and supercritical CO_2 conditions with H_2S addition.

Table 23: EIS fitting results of C1018 exposed to the sub-critical CO_2 environment at 60°C, 80°C, 100°C, and 120°C with 5 ppm and 50 ppm H_2S.

H_2S concentration (ppm)	Temperature (°C)	Time (h)	R_s ($\Omega\ cm^2$)	Q_f ($\Omega^{-1}s^n cm^{-2}$)	n	R_f ($\Omega\ cm^2$)	Q_{dl} ($\Omega^{-1}s^n cm^{-2}$)	n	R_{ct} ($\Omega\ cm^2$)
5	60	1st	2.944	12.6 x 10^{-2}	0.83	6.621	5.315	1	1.82
		5th	2.277	3.65 x 10^{-2}	0.78	7.343	3.223	0.94	2.767
		25th	2.597	3.45 x 10^{-3}	1	0.154	0.129	0.69	6.576
		40th	2.82	1.98 x 10^{-1}	0.66	6.725	1.303	1	0.0863
5	80	1st	2.407	3.01 x 10^{-4}	0.65	6.227	4.12 x 10^{-4}	0.65	4.467
		5th	2.966	3.36 x 10^{-5}	0.85	2.782	1.34 x 10^{-1}	0.26	9.24
		25th	5.21	3.8 x 10^{-4}	0.57	2.87	3.09 x 10^{-1}	0.72	3.919
		40th	8.318	3.97 x 10^{-4}	1	0.203	3.28 x 10^{-1}	0.77	4.38
5	100	25th	1.52 x 10^{-3}	1.75 x 10^{-8}	0.78	1.89 x 10	3.7 x 10^{-5}	0.28	7.26 x 10^4
		40th	126.4	4.59 x 10^{-9}	0.87	1.77 x 10	2.91 x 10^{-5}	0.22	1.53 x 10^5
5	120	5th	1.31 x 10^{-3}	1.43 x 10^{-8}	0.77	1.02 x 10	8.75 x 10^{-5}	0.2	6.45 x 10^5
		25th	228.2	2.9 x 10^{-9}	0.91	4.42 x 10	7.09 x 10^{-5}	0.2	6.12 x 10^6
		40th	2.859	1.75 x 10^{-8}	0.76	1.23 x 10	7.22 x 10^{-5}	0.22	6.12 x 10^6

Table 24 Continued: EIS fitting results of C1018 exposed to the sub-critical CO_2 environment at 60°C, 80°C, 100°C, and 120°C with 5 ppm and 50 ppm H_2S.

50	60	5th	2.318	6.46×10^{-2}	0.79	5.682	8.029	1	5.103
		25th	2.25	1.04×10^{-1}	0.74	6.21	10.1	1	12.54
		40th	2.249	1.38×10^{-1}	0.72	6.458	10.29	1	90.1
50	80	5th	1.308	2.42×10^{-1}	0.78	4.964	12.19	1	3.633
		25th	1.233	2.16×10^{-2}	1	0.223	2.76×10^{-1}	0.82	7.581
		40th	1.311	3.36×10^{-2}	0.9	0.311	2.58×10^{-1}	0.85	15.8
50	100	25th	1.16×10^{-4}	2.81×10^{-5}	0.38	7.46 x 10	1.28×10^{-5}	0.61	5.69×10^{4}
		40th	6.65×10^{-2}	1.79×10^{-5}	0.39	8.46 x 10	1.41×10^{-5}	0.58	7.01×10^{4}
50	120	25th	1.446	1.01×10^{-9}	1	2.91 x 10	3.6×10^{-5}	0.39	4.14×10^{4}
		40th	41.43	1.21×10^{-9}	1	2.79 x 10	3.12×10^{-5}	0.4	4.77×10^{4}

Effect of Temperature

Figure 43 shows the Nyquist plots from the EIS testing of C1018 exposed to a sub-critical CO_2 environment with 100 ppm of H_2S addition at (a)60°C, (b)80°C, (c)100°C, and (d)120°C. The EIS results at 60°C, 80°C, and 120°C present high corrosion resistance while low corrosion resistance appears in the EIS result at 100°C. It shows that the corrosion rate was relatively higher at 100°C in the 1st hour, 5th hour, 25th hour, and 40th hour compared to different temperatures in the same time periods. It is because at 95°C iron carbonate was favored to generate under an environment containing CO_2 gas. Abundant irons were oxidized to iron ions (Fe^{2+}) and released into the solution, which resulted in an increase in the current, which is why the current increased. Therefore, the dissolution of iron ion was dominating the system at 100°C. Nonetheless, it is not always the case that high temperature results in a high corrosion rate although it is theoretically true. At high temperature, types and scaling of the corrosion products on the material

surface also need to be considered because it is well-known that iron carbonate can serve as a function of protection for carbon steel as its nature is noble to CO_2 environment [45]. Thus, it explains well for the corrosion phenomenon at 120°C, shown in Figure 43 (d). At 120°C, the corrosion resistance went up again, which meant the corrosion rate became lower. It was due to the iron carbonate formed from the iron ions combined with carbonate ions (CO_3^{2-}) and precipitating on top of the steel surface. Hence, as the iron carbonate continued to scale on the steel surface, the system became less active compared to the system at 100°C. This transition of corrosion rate was also proven by our LPR results at 100°C in a sub-critical CO_2 environment with 100 ppm of H_2S (not shown).

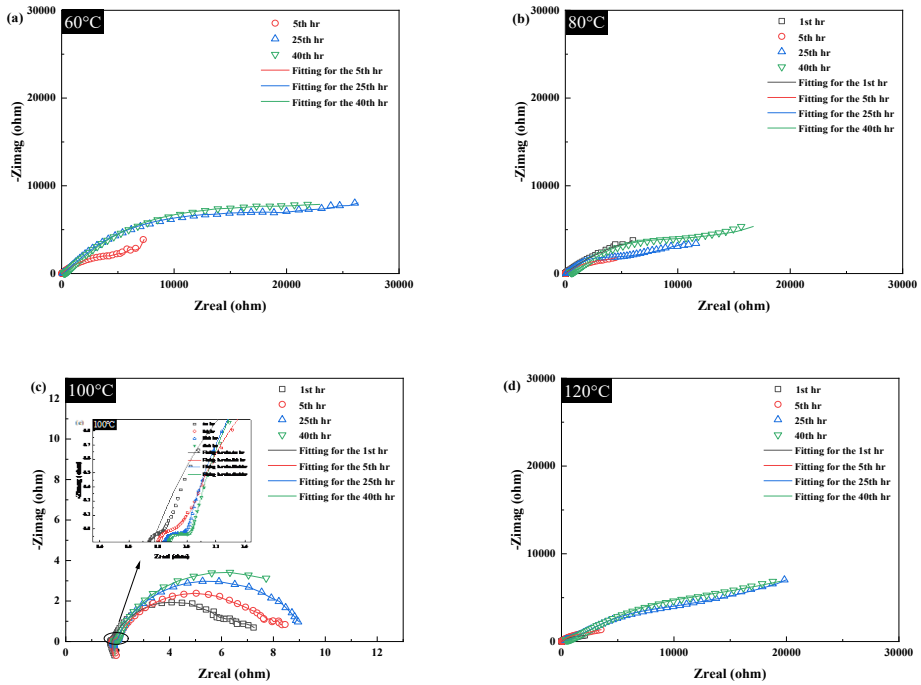

Figure 48: Corrosion behavior of the corrosion products in the sub-critical CO_2 environment at 60°C, 80°C, 100°C, and 120°C with 100 ppm H_2S.

Table 24 shows the electric parameters of each medium output by using the same equivalent circuit for the EIS testing exposed to a sub-critical CO_2 environment with 100 ppm of H_2S addition at 60°C, 80°C, 100°C, and 120°C. In the sub-critical CO_2 environment with 100 ppm of H_2S, the charge transfer resistances were higher than the resistances of the corrosion product film at the four temperatures at different times, which was the same as the resistance comparison in both 5 ppm and 50 ppm of H_2S, respectively. Hence, the effect of the charge transfer resistance was more significant than the effect of the resistance of the corrosion product film.

On the other hand, while the charge transfer resistance was high at 60°C and at 80°C, it decreased significantly at 100°C. This was attributed to the formation of iron carbonate at 95°C; carbonate ions (CO_3^{2-}) abundantly reacted with iron ions (Fe^{2+}) to form iron carbonate [2]. The abundant carbonate ions, which combined with iron ions, released a lot of electrons into the solution, which lowered the corrosion resistance and caused the increase in the corrosion rate. When the temperature was raised to 120°C, the charge transfer resistance went up again. This increase in the charge transfer resistance could be contributed from the iron carbonate scaling up over the steel surface, covering the active sites of available spots, which further resulted in lowering the corrosion rate.

Reduction of CO_2:

$$2H_2CO_3 + 2e^- \rightarrow 2HCO_3^- + H_2 \quad (30)$$

$$2HCO_3^- + 2e^- \rightarrow 2CO_3^{2-} + H_2 \quad (31)$$

Table 25: EIS fitting results of C1018 exposed to the sub-critical CO_2 environment at 60°C, 80°C, 100°C, and 120°C with 100 ppm H_2S.

H_2S concentration (ppm)	Temperature (°C)	Time (h)	R_s ($\Omega\ cm^2$)	Q_f ($\Omega^{-1}s^n cm^{-2}$)	n	R_f ($\Omega\ cm^2$)	Q_{dl} ($\Omega^{-1}s^n cm^{-2}$)	n	R_{ct} ($\Omega\ cm^2$)
100	60	5th	10.63	1.77 x 10^{-4}	0.45	92.77	4.73 x 10^{-5}	0.62	1.25 x 10^4
		25th	44.44	2.62 x 10^{-5}	0.43	284	1.65 x 10^{-5}	0.67	3.4 x 10^4
		40th	19.97	4.34 x 10^{-6}	0.49	374.6	3.26 x 10-5	0.57	3.42 x 10^4
100	80	1st	3.85 x 10^{-3}	1.96 x 10^{-4}	0.38	15.8	2.31 x 10^{-4}	0.56	2.94 x 10^4
		5th	3.83 x 10^{-3}	1.59 x 10^{-4}	0.4	72.04	2.37 x 10^{-4}	0.49	9.16 x 10^3
		25th	65.86	4.29 x 10^{-7}	0.76	66.1	6.8 x 10^{-5}	0.49	1.21 x 10^4
		40th	221.7	3.71 x 10^{-9}	0.97	302.1	4.52 x 10^{-5}	0.46	2.52 x 10^4
100	100	1st	1.779	8.37 x 10^{-2}	0.85	4.724	8.347	1	1.232
		5th	1.817	6.48 x 10^{-2}	0.69	0.658	2.07 x 10^{-2}	1	6.07
		25th	1.856	7.67 x 10^{-3}	1	0.151	0.182	0.87	7.26
		40th	1.896	9.28 x 10^{-3}	1	0.145	0.254	0.88	8.06
100	120	1st	9.68	3.71 x 10^{-5}	0.62	22.84	6.94 x 10^{-4}	0.45	3.36 x 10^3
		5th	20.41	6.14 x 10^{-6}	0.68	26.26	3.9 x 10^{-4}	0.5	4.98 x 10^3
		25th	98.52	4.98 x 10^{-8}	0.78	363	6.05 x 10^{-5}	0.38	3.46 x 10^4
		40th	102.2	4.61 x 10^{-8}	0.78	417.6	5 x 10^{-5}	0.39	4.36 x 10^4

Effect of CO_2 Pressure with H_2S addition

Figure 44 shows the Nyquist plots from EIS testing of C1018 exposed to the sub-critical CO_2 environment with 200 ppm of H_2S at (a)80°C, (b)100°C, (c)120°C and the supercritical CO_2 environment with 200 ppm of H_2S at (d)60°C, (e)80°C, (f)100°C, and (g)120°C. In the sub-critical CO_2 environment with 200 ppm of H_2S, two compressed capacitor semicircles were observed at both 80°C (Figure 44 (a)) and 100°C (Figure 44 (b)) as well; again, one at high frequency represented a double layer resistance and a charge transfer resistance, and the other one at low frequency was for corrosion product resistance. At each temperature, the capacitor semicircle at low frequency was larger than

the one at high frequency, meaning the corrosion rate of the corrosion product film was lower than the one for the double layer resistance and charge transfer resistance. Moreover, the capacitor semicircle at low frequency at 100°C was smaller compared with the one at 80°C, illustrating the corrosion rates on both the corrosion product and the steel surface at 100°C (shown in the inner plots inside Figure 44 (a) and (b)) were higher than they were at 80°C. At 120°C shown in Figure 44 (c), a small capacitor semicircle was observed in the 1st hour, showing the corrosion rate was high, whereas two bigger capacitor semicircles were formed in the 25th hour and 40th hour. Note that the first capacitor semicircle was larger in the 25th hour and 40th hour than the second capacitor semicircle, showing the corrosion rate was low on the corrosion film and on the steel surface.

On the other hand, the Nyquist result of C1018 exposed to the supercritical CO_2 environment with 200 ppm of H_2S (Figure 44 (d)-(g)) does not show a clear second compressed capacitor resistance at low frequency until 120°C. At 60°C, the entire system remained active to the end of the testing, which was proven by the decrease in the size of the semicircle in the 40th hour, meaning the corrosion process continued during the entire period. This result was the opposite compared to the Nyquist results of C1018 exposed to the sub-critical CO_2 environment at the same temperature. The possible reason was that at this temperature, the system in the supercritical CO_2 condition led to a lower pH value, providing sufficient carbonate ions to react with iron ions. Hence, the corrosion process continued till the end. The same tendency of the size transition of the semicircle also was observed in the Nyquist result tested at 80°C in supercritical CO_2 environment with 200 ppm of H_2S. Here, it was assumed that the high partial pressure of CO_2 outweighed the

protective layer of hydrogen sulfide in the system because even with the layer of hydrogen sulfide generated on the steel surface, the corrosion rate was still increasing for the entire testing period. When the temperature was increased to 120°C, two capacitor semicircles were clearly observed in the 5th hour, 25th hour, and the 40th hour. The curve in the 25th and 40th hours shifted to a higher resistance compared to the one in the 5th hour, indicating the iron concentration in the solution was increased with the increase of time. Also, the corrosion rate of the corrosion products was lower than the corrosion rate on the steel surface, which was proven by the larger semicircle at low frequency compared to the smaller semicircle at high frequency. Note that the corrosion products were composed of iron sulfide and iron carbonate, and at 120°C in the supercritical CO_2 environment with the addition of 200 ppm of H_2S iron carbonate was dominating the system as it was scaled all over the steel surface without intact iron sulfide observed.

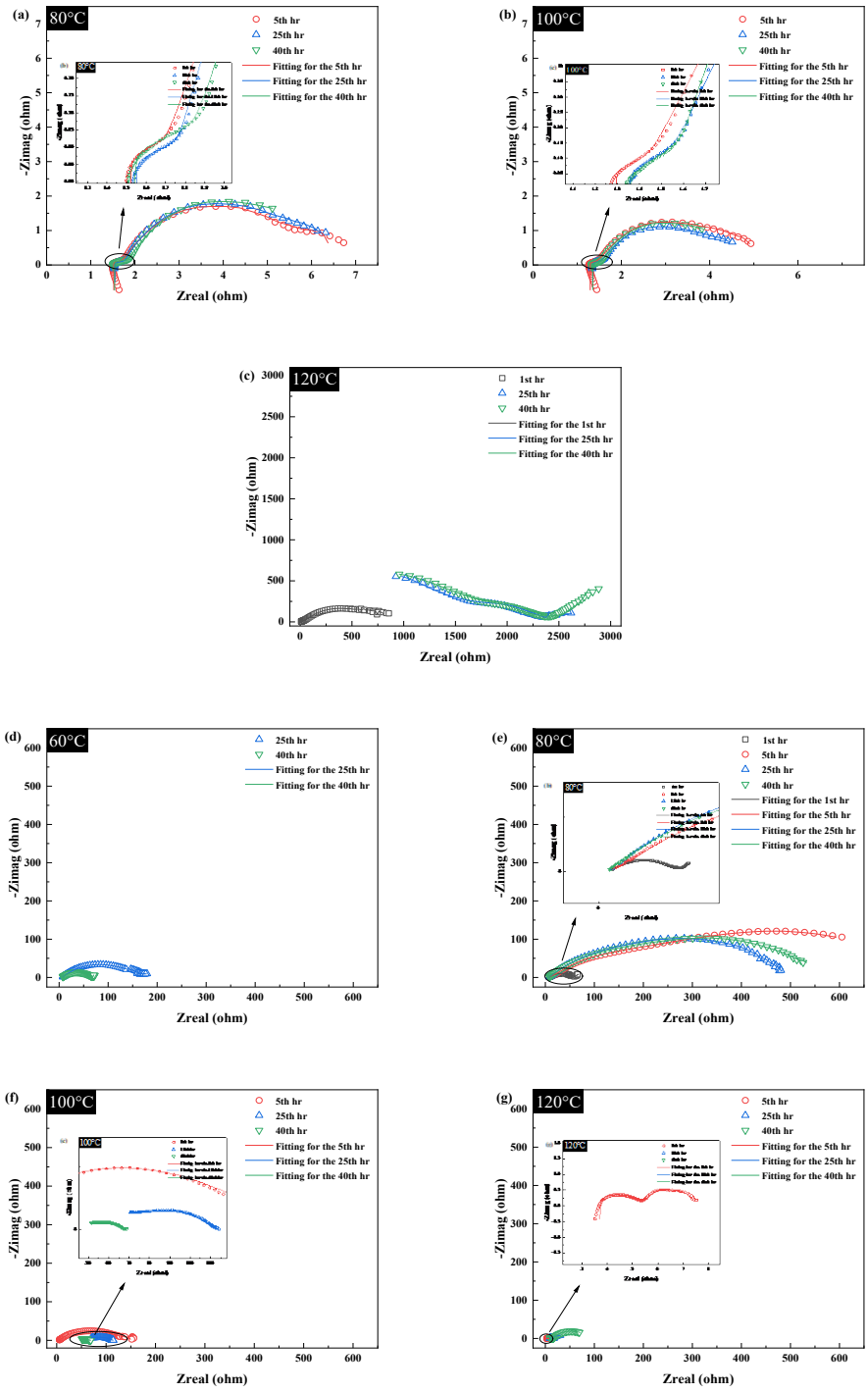

Figure 49: Corrosion behavior of the corrosion products with 200 ppm H_2S (a)-(c) in the sub-critical CO_2 environment at 80°C, 100°C, and 120°C and (d)-(g) in the supercritical CO_2 environment at 60°C, 80°C, 100°C, and 120°C.

Table 25 shows the electric parameters of each medium output by using the same equivalent circuit for the EIS testing exposed to a sub-critical and a supercritical CO_2 environment with the addition of 200 ppm H_2S at 60ºC, 80ºC, 100ºC, and 120ºC. Apart from the effects of time and temperature, which were discussed above, the effect of pressure was more clearly shown by the comparison of the supercritical CO_2 condition at 120ºC with the sub-critical CO_2 condition than the comparison at lower temperatures (60ºC and 80ºC). Both the resistance of the corrosion product film and the charge transfer resistance at 120ºC in the supercritical environment were lower than the ones in the sub-critical CO_2 environment at the same temperature. Considering that the temperature and H_2S concentration were the same in both environments, it was assumed that their effects on the resistances were insignificant or neglectable. By ruling out the effects of temperature and H_2S concentration, it suggests that the reason for the large reduction on the charge transfer resistance was caused by the high CO_2 partial pressure causing abundant CO_2 to dissolve into the solution, which further lowered the pH value. With the thermodynamic calculation from the OLI software, the pH value in the supercritical CO_2 environment with H_2S was predicted to be 3.8 to 3.9. Under this circumstance and potential of the system, iron carbonate was favored to be the corrosion product combined by carbonate ions with iron ions. Also, due to the high pressure, the corrosion product film was grown more compactly than it was in the sub-critical environment. The sample was covered by a thin layer combination of iron carbonate and iron sulfide, which resulted from the CO_2 supercritical state.

Table 26: EIS fitting results of C1018 exposed to the sub-critical and supercritical CO_2 conditions at 60°C, 80°C, 100°C, and 120°C with 200 ppm H_2S.

CO_2 Partial Pressure (psi)	Temperature (°C)	Time (h)	R_s ($\Omega\ cm^2$)	Q_f ($\Omega^{-1}s^n cm^{-2}$)	n	R_f ($\Omega\ cm^2$)	Q_{dl} ($\Omega^{-1}s^n cm^{-2}$)	n	R_{ct} ($\Omega\ cm^2$)
400 (Sub-critical)	80	5th	1.52	5.03 x 10^{-3}	1	0.197	0.146	0.78	4.82
		25th	1.548	1.57 x 10^{-2}	0.91	0.234	0.289	0.83	4.68
		40th	1.539	2.58 x 10^{-2}	0.87	0.339	0.398	0.82	5.04
400 (Sub-critical)	100	5th	1.294	1.31 x 10^{-2}	1	0.174	0.312	0.75	3.68
		25th	1.355	3.53 x 10^{-2}	0.91	0.216	0.471	0.79	3.13
		40th	1.352	19.1 x 10^{-2}	0.66	0.392	0.378	0.93	3.1
400 (Sub-critical)	120	1st	4.592	2.14 x 10^{-5}	0.65	23.02	5.69 x 10^{-4}	0.47	854.4
		25th	9.82 x 10^{-6}	4.41 x 10^{-6}	0.37	241	8.14 x 10^{-2}	0.99	1.61 x 10^5
		40th	7.781	9.55 x 10^{-8}	0.64	756	3.04 x 10^{-4}	0.07	4.13 x 10^3
1600 (Supercritical)	60	25th	6.246	3.42 x 10^{-4}	0.53	116.7	1.86 x 10^{-2}	0.6	534.4
		40th	6.525	5.9 x 10^{-5}	0.66	1.04 x 10^{-4}	5.63 x 10^{-4}	0.4	64.56
1600 (Supercritical)	80	1st	6.955	5.86 x 10^{-4}	0.47	52.23	0.316	0.47	1.41 x 10^6
		5th	7.7	6.77 x 10^{-4}	0.44	8.08 x 10^{-2}	1.87 x 10^{-3}	0.1	1.3 x 10^4
		25th	6.441	4.51 x 10^{-4}	0.5	415.1	1.67 x 10^{-3}	0.86	81.23
		40th	6.438	2.21 x 10^{-4}	0.56	2.132	7.41 x 10^{-4}	0.32	627.3
1600 (Supercritical)	100	5th	3.975	7.48 x 10^{-4}	0.48	0.14	7.24 x 10^{-3}	0.28	3.28 x 10^4
		25th	56.46	6.16 x 10^{-4}	0.33	58.03	1.25 x 10^3	0.32	0.11
		40th	42.01	3.51 x 10^{-7}	0.77	4.387	1.73 x 10^{-3}	0.33	22.21
1600 (Supercritical)	120	5th	3.637	1.68 x 10^{-3}	0.65	1.607	0.397	0.58	2.427
		25th	9.125	1.28 x 10^{-3}	0.5	7.05	0.249	0.72	24.6
		40th	8.932	1.28 x 10^{-3}	0.48	7.78	3.04 x 10^{-2}	0.61	73.37

Corrosion mechanism of supercritical CO_2 environment with the addition of H_2S:

Initially, the $H_2S_{(g)}$ dissolved into an aqueous solution as an aqueous form of hydrogen sulfide, $H_2S_{(aq)}$, (5 ppm and 50 ppm) rapidly owing to the low solubility limit of iron sulfide and adsorbed onto the surface as a thin film. At low temperatures like 60°C and 80°C, hydrogen sulfide, $H_2S_{(aq)}$, was quickly converted to iron sulfide, which provided a protective function to protect the steel surface from being corroded. At 100°C and 120°C, the system seemed to be dominated by another corrosion product, iron carbonate, as the formation of the iron carbonate was favored to take place at 95°C in an

environment full of CO_2. That was why the corrosion rate increased tremendously at 100°C. When the temperature reached 120°C, it was shown that the iron carbonate scaled all over the steel surface, leading to a decrease in corrosion rate. As time elapsed, the corrosion process reached a dynamic balance between iron dissolution and the formation of iron carbonate at high temperature. However, as the H_2S concentration was increased to 100 ppm and 200 ppm, the iron sulfide corrosion products became so thick that it is easily led to a mechanical fracture on the surface due to inner stress, which resulted in a high roughness for the surface. The formation of iron carbonate underneath also partially contributed to this phenomenon. When the iron sulfide thin film was broken and the steel surface was exposed to the acidic solution (carbonate ion solution), the steel surface continued to be corroded. At this point, the corrosion rate increased until the iron carbonate was fully scaled on the surface to form another protective film for the steel surface. Eventually, with the protection of iron carbonate, the corrosion rate decreased, and the surface became noble again due to the nature of iron carbonate compared to carbon steels.

4.5. Conclusion

1. The presence of H_2S in a supercritical CO_2 state has a major impact on mild carbon steel C1018, influencing the corrosion rate through the surface morphology and microstructure; as the H_2S concentration increased from 5 ppm to 200 ppm, an increase in the thickness of iron sulfide corrosion product adsorbed on the steel surface was observed.
2. The microstructure of iron sulfide corrosion product was converted to troilite at 120°C from amorphous iron sulfide - mackinawite from 60°C to 100°C; while the low H_2S concentration (5 ppm) was beneficial to the corrosion rate at 60°C and 80°C as the amorphous iron sulfide covered the steel surface as a protective thin film, higher H_2S concentrations like 50 ppm, 100 ppm, and 200 ppm, caused cracking issues on the surface due to inner stress and exposed it to the corrosive solution, further increasing the corrosion rate of the system.
3. The effect of temperature promoted the formation of iron carbonate at 100°C and 120°C, which speeded up the corrosion process, so it outweighed the effect of the H_2S presence in the supercritical CO_2 environment regarding the corrosion rate.
4. Yet under the effect of time, the corrosion rates decreased with the exposure time gradually held true at 60°C, 80°C, 100°C, and 120°C with all the H_2S concentrations – 5 ppm, 50 ppm, 100 ppm, and 200 ppm.
5. These are the prioritized environmental factors from the highest to lowest impact on the supercritical CO_2 environment with the existence of H_2S: pressure, temperature, H_2S concentration, and time.

4.6. References

1. Zhang, G.A., et al., *Electrochemical corrosion behavior of carbon steel under dynamic high pressure H2S/CO2 environment.* Corrosion Science, 2012. **65**: p. 37-47.
2. Gao, S., et al., *Corrosion Behavior of Mild Steel in Sour Environments at Elevated Temperatures*. 2017.
3. Karimi Abadeh, H. and M. Javidi, *Assessment and influence of temperature, NaCl and H2S on CO2 corrosion behavior of different microstructures of API 5L X52 carbon steel in aqueous environments.* Journal of Natural Gas Science and Engineering, 2019. **67**: p. 93-107.
4. Choi, Y.-S., S. Nesic, and S. Ling, *Effect of H2S on the CO2 corrosion of carbon steel in acidic solutions.* Electrochimica Acta, 2011. **56**(4): p. 1752-1760.
5. Ma, H., et al., *The influence of hydrogen sulfide on corrosion of iron under different conditions.* Corrosion Science, 2000. **42**(10): p. 1669-1683.
6. Abelev, E., T.A. Ramanarayanan, and S.L. Bernasek, *Iron Corrosion in CO[sub 2]/Brine at Low H[sub 2]S Concentrations: An Electrochemical and Surface Science Study.* Journal of The Electrochemical Society, 2009. **156**(9): p. C331.
7. Greco, E.C. and W.B. Wright, *Corrosion of Iron in an H2S-CO2-H2O System.* Corrosion, 2013. **18**(3): p. 119t-124t.
8. Sardisco, J.B., W.B. Wright, and E.C. Greco, *Corrosion of Iron in on H2S-CO2-H2O System: Corrosion Film Properties on Pure Iron.* Corrosion, 2013. **19**(10): p. 354t-359t.
9. Sardisco, J.B. and R.E. Pitts, *Corrosion of Iron in an H2S-CO2-H2O System Mechanism of Sulfide Film Formation and Kinetics of Corrosion Reaction.* Corrosion, 2013. **21**(8): p. 245-253.
10. Bolmer, P.W., *Polarization of Iron in H2S-NaHS Buffers.* Corrosion, 2013. **21**(3): p. 69-75.
11. Morris, D.R., L.P. Sampaleanu, and D.N. Veysey, *The Corrosion of Steel by Aqueous Solutions of Hydrogen Sulfide.* Journal of The Electrochemical Society, 1980. **127**(6): p. 1228-1235.
12. Galvan-Martinez, R., et al., *Effects of turbulent flow on the corrosion kinetics of X52 pipeline steel in aqueous solutions containing H2S.* Materials and Corrosion, 2004. **55**(8): p. 586-593.
13. Kittel, J., et al., *Corrosion mechanisms in aqueous solutions containing dissolved H2S. Part 1: Characterisation of H2S reduction on a 316L rotating disc electrode.* Corrosion Science, 2013. **66**: p. 324-329.
14. Tribollet, B., et al., *Corrosion mechanisms in aqueous solutions containing dissolved H2S. Part 2: Model of the cathodic reactions on a 316L stainless steel rotating disc electrode.* Electrochimica Acta, 2014. **124**: p. 46-51.
15. Kahyarian, A. and S. Nesic, *H2S corrosion of mild steel: A quantitative analysis of the mechanism of the cathodic reaction.* Electrochimica Acta, 2019. **297**: p. 676-684.

16. Asadian, M., M. Sabzi, and S.H.M. Anijdan, *The effect of temperature, CO2, H2S gases and the resultant iron carbonate and iron sulfide compounds on the sour corrosion behaviour of ASTM A-106 steel for pipeline transportation.* International Journal of Pressure Vessels and Piping, 2019. **171**: p. 184-193.
17. Santos, B.A.F., et al., *The effect of different brines and temperatures on the competitive degradation mechanisms of CO2 and H2S in API X65 carbon steel.* Journal of Natural Gas Science and Engineering, 2020. **80**: p. 103405.
18. Suleimenov, O.M. and R.E. Krupp, *Solubility of hydrogen sulfide in pure water and in NaCl solutions, from 20 to 320°C and at saturation pressures.* Geochimica et Cosmochimica Acta, 1994. **58**(11): p. 2433-2444.
19. Nordsveen, M., S.N.R. Nyborg, and A. Stangeland, *A Mechanistic Model for Carbon Dioxide Corrosion of Mild Steel in the Presence of Protective Iron Carbonate FilmsPart 1: Theory and Verification.* Corrosion, 2003. **59**(05).
20. Diebler, H., *E. Högfeldt (Ed.): Stability Constants of Metal-Ion Complexes, Part A: Inorganic Ligands, Vol. 21 aus: IUPAC Chemical Data Series. Pergamon Press, Oxford, New York, Toronto, Sydney, Paris, Frankfurt 1982. 310 Seiten, Preis: $ 85.00.* Berichte der Bunsengesellschaft für physikalische Chemie, 1983. **87**(12): p. 1227-1227.
21. Weiss, R.F., *The solubility of nitrogen, oxygen and argon in water and seawater.* Deep Sea Research and Oceanographic Abstracts, 1970. **17**(4): p. 721-735.
22. Roberts, B.E. and P.R. Tremaine, *Vapour liquid equilibrium calculations for dilute aqueous solutions of CO2, H2S, NH3 and NaOH to 300°C.* The Canadian Journal of Chemical Engineering, 1985. **63**(2): p. 294-300.
23. Suleimenov, O.M. and T.M. Seward, *A spectrophotometric study of hydrogen sulphide ionisation in aqueous solutions to 350°C.* Geochimica et Cosmochimica Acta, 1997. **61**(24): p. 5187-5198.
24. Kharaka, Y.K. and S. Geological, *SOLMINEQ. 88, a computer program for geochemical modeling of water-rock interactions*. Computer program for geochemical modeling of water-rock interactions. 1989, Menlo Park, Calif. : Denver, CO: Dept. of the Interior, U.S. Geological Survey ; U.S. Geological Survey, Books and Open-File Reports [distributor]. 420 pages.
25. Millero, F.J., *The thermodynamics and kinetics of the hydrogen sulfide system in natural waters.* Marine Chemistry, 1986. **18**(2): p. 121-147.
26. Myers, R.J., *The new low value for the second dissociation constant for H2S: Its history, its best value, and its impact on the teaching of sulfide equilibria.* Journal of Chemical Education, 1986. **63**(8): p. 687.
27. Ellis, A.J. and W. Giggenbach, *Hydrogen sulphide ionization and sulphur hydrolysis in high temperature solution.* Geochimica et Cosmochimica Acta, 1971. **35**(3): p. 247-260.
28. Licht, S., et al., *Conductometric analysis of the second acid dissociation constant of H2S in highly concentrated aqueous media.* Journal of Electroanalytical Chemistry and Interfacial Electrochemistry, 1991. **318**(1): p. 111-129.
29. Skoog, D.A., *Fundamentals of analytical chemistry*. 1982, New York: Holt, Rinehart, and Winston.

30. Su, Y.S., K.L. Cheng, and Y.C. Jean, *Amplified potentiometric determination of pK00, pK0, pKl, and pK2 of hydrogen sulfides with Ag2S ISE.* Talanta, 1997. **44**(10): p. 1757-1763.
31. Ning, J., et al., *Thermodynamic Study of Hydrogen Sulfide Corrosion of Mild Steel.* Corrosion, 2013. **70**(4): p. 375-389.
32. Smith, S.N. and M.W. Joosten, *Corrosion of Carbon Steel by H2S in CO2 Containing Oilfield Environments*. 2006.
33. Singer, M., et al., *Sour Top Of The Line Corrosion In The Presence Of Acetic Acid*. 2010.
34. Wolthers, M.t., S.J. Van der Gaast, and D. Rickard, *The structure of disordered mackinawite.* American Mineralogist, 2003. **88**(11-12): p. 2007-2015.
35. Rickard, D., et al., *The composition of nanoparticulate mackinawite, tetragonal iron(II) monosulfide.* Chemical Geology, 2006. **235**(3): p. 286-298.
36. *Peer Reviewed: Chemical Dynamics of Sedimentary Acid Volatile Sulfide.* Environmental Science & Technology, 2004. **38**(7): p. 131A-136A.
37. Berner, R.A., *thermodynamic stability of sedimentary iron sulfides.* American Journal of Science, 1967. **265**(9): p. 773.
38. Sweeney, R.E. and I.R. Kaplan, *Pyrite Framboid Formation; Laboratory Synthesis and Marine Sediments.* Economic Geology, 1973. **68**(5): p. 618-634.
39. Rickard, D. and G.W. Luther, *Chemistry of Iron Sulfides.* Chemical Reviews, 2007. **107**(2): p. 514-562.
40. Lennie, A.R. and D.J. Vaughan, *Spectroscopic studies of iron sulfide formation and phase relations at low temperatures*. Vol. 5. 1996: The Geochemical Society Houston, TX.
41. Arnold, R.G., *Pyrrhotite phase relation below 304.* Economic Geology, 1969. **64**(4): p. 405-419.
42. Sun, J., et al., *Effect of O2 and H2S impurities on the corrosion behavior of X65 steel in water-saturated supercritical CO2 system.* Corrosion Science, 2016. **107**: p. 31-40.
43. Alpermann, T., M. Dietrich, and C. Ostertag-Henning, *Mineral trapping of a CO2/H2S mixture by hematite under initially dry hydrothermal conditions.* International Journal of Greenhouse Gas Control, 2016. **51**: p. 346-356.
44. López, D.A., S.N. Simison, and S.R. de Sánchez, *The influence of steel microstructure on CO2 corrosion. EIS studies on the inhibition efficiency of benzimidazole.* Electrochimica Acta, 2003. **48**(7): p. 845-854.
45. Wei, L., X. Pang, and K. Gao, *Effect of small amount of H2S on the corrosion behavior of carbon steel in the dynamic supercritical CO2 environments.* Corrosion Science, 2016. **103**: p. 132-144.